

UC Berkeley

UC Berkeley Electronic Theses and Dissertations

Title

Fundamental Spectroscopic Studies of Lithium Sulfur Battery Reaction Mechanisms

Permalink

<https://escholarship.org/uc/item/3v9402x0>

Author

Wujcik, Kevin Hamilton

Publication Date

2016

Peer reviewed|Thesis/dissertation

Fundamental Spectroscopic Studies of Lithium Sulfur Battery Reaction Mechanisms

By

Kevin Hamilton Wujcik

A dissertation submitted in partial satisfaction of the

requirements for the degree of

Doctor of Philosophy

in

Chemical Engineering

in the

Graduate Division

of the

University of California, Berkeley

Committee in charge:

Professor Nitash Balsara, Chair

Professor Roya Maboudian

Professor Kristin Persson

Fall 2016

Fundamental Spectroscopic Studies of Lithium Sulfur Battery Reaction Mechanisms

© 2016

by Kevin Hamilton Wujcik

Abstract

Fundamental studies of lithium sulfur battery reaction mechanisms

by

Kevin Hamilton Wujcik

Doctor of Philosophy in Chemical Engineering

University of California, Berkeley

Professor Nitash Balsara, Chair

Lithium sulfur batteries have garnered a significant amount of attention as a next-generation energy storage technology. They have a theoretical specific capacity of 1672 mAh/g and a theoretical specific energy density of 2600 Wh/kg, which is five times greater than current lithium ion battery standards. Unfortunately, Li-S cells are plagued with numerous scientific problems that make practical implementation of the technology impossible. The overall reaction mechanism for the battery is given by $S_8 + 16 e^- + 16 Li^+ \rightarrow 8 Li_2S$. However, it is well-known that the actual reaction mechanism is much more complex, involving a multistep series of reactions through which lithium polysulfide reaction intermediates are formed. Lithium polysulfides are highly soluble in common battery electrolytes, and as a result, their formation during charge/discharge leads to their dissolution out of the cathode and into the cell electrolyte separator. This results in a direct loss of cell capacity, detrimental reactions at the cell anode, and ultimately, cell failure.

Despite over four decades of research, the redox reaction mechanisms that govern the Li-S charge/discharge processes are still unclear. This is primarily due to challenges associated with obtaining spectral ‘fingerprints’ for the lithium polysulfide intermediates (Li_2S_x , $2 \leq x \leq 8$, referred to as polysulfide dianions; or LiS_x , $3 \leq x \leq 5$, referred to as polysulfide radical anions). Numerous spectroscopy and characterization techniques have been used to study the Li-S redox reactions, but all have had issues obtaining unambiguous spectral standards for the different polysulfide dianion species. In this work, X-ray absorption spectroscopy at the sulfur K-edge is used to study Li-S battery reaction mechanisms and lithium polysulfide mixtures. First principles calculations of theoretical spectra of lithium polysulfide species are used to interpret results obtained for experimentally measured Li-S battery cells. These theoretical calculations circumvent the issues associated with obtaining spectral standards for polysulfide species experimentally. Fundamental studies of Li-S chemistry are a necessity to our ability to rationally address and overcome the obstacles that Li-S batteries face.

To begin, X-ray absorption spectroscopy at the sulfur K-edge was used to probe

chemically synthesized mixtures of lithium polysulfide species dissolved in a block copolymer of poly(styrene)-poly(ethylene oxide) (SEO), and a homopolymer of poly(ethylene oxide) (PEO). For both solvents, a series of spectra were gathered for polysulfide mixtures that had stoichiometric Li_2S_x 'x' values of 2, 4, 6 and 8. The system of experimental spectra obtained from XAS was analyzed using a statistical technique called principal component analysis. This analysis revealed that the polysulfide mixtures contained only three species: Li_2S , Li_2S_4 , and Li_2S_8 . The parsimonious interpretation of these results suggests that in PEO-based solid electrolytes containing chemically synthesized polysulfide species, Li_2S_6 and Li_2S_2 disproportionate to form binary mixtures of $\text{Li}_2\text{S}_4/\text{Li}_2\text{S}_8$, and $\text{Li}_2\text{S}/\text{Li}_2\text{S}_4$, respectively.

Next, XAS at the sulfur K-edge was used to examine Li-S cells that were discharged to different depths of discharge and allowed to reach equilibrium. The experimental geometry and novel cell construction was such that incoming X-rays primarily probed the lithium polysulfide species dissolved in the cell electrolyte. Analysis of the experimental spectra using theoretically calculated spectra from first principles revealed that polysulfide radical anions were present in the Li-S cell electrolyte after discharge. However, evidence of radical polysulfide species was only obtained for a cell that was stopped at the midpoint of the first discharge plateau. No evidence of polysulfide radical species was found at increased depths of discharge. This suggests that polysulfide radical species are formed during early stages of discharge, or that polysulfide radical species are formed through chemical disproportionation reactions involving polysulfide dianion species electrochemically created during the initial stages of discharge. The detection of radical species was especially notable given that the electrolyte used in the Li-S cell was an ether-based polymer electrolyte (SEO). While it had already been established that radicals were stable in electrolytes with high electron pair donor numbers, it was unclear whether or not radical species could be stabilized in ether-based solvent (which have low electron pair donor numbers).

The appearance of polysulfide radical species in the electrolyte of partially discharged Li-S cells motivated a further examination of the stability of radical species in ether-based electrolytes. Lithium polysulfide species dissolved in PEO and a PEO oligomer of tetraethylene glycol dimethyl ether (TEGDME) were probed using a combination of ultraviolet-visible (UV-vis) spectroscopy and electron paramagnetic resonance (EPR) spectroscopy. EPR results unambiguously confirmed the presence of radical species in ether-based electrolytes. Comparison of the EPR spectra to corresponding UV-vis spectra established that the UV-vis absorbance signature for radical species in ether-based solvents occurs at a wavelength of 617 nm. Additionally, analysis of the UV-vis spectra using the Beer Lambert law allowed for the determination of polysulfide radical concentration and the fraction of sulfur that was present in the form of radical species. As sulfur concentration increased, the fraction of sulfur (on an atomic basis) present in the form of radical species decreased. That is, polysulfide radical species are less stable at higher concentrations of sulfur (and lithium) and likely recombine to form dianion species (e.g. through reactions of the kind: $2 \text{LiS}_3 \rightarrow \text{Li}_2\text{S}_6$).

Multiple authors have shown that in order for Li-S batteries to succeed, Li-S cathodes

need to be thicker than what is typically used in Li-S battery research. Little is known about the fundamental reaction mechanisms and chemical processes that take place in thick cathodes, as most research has focused on studying thinner cathodes that enable high performance. In this part of the dissertation work, in situ XAS at the sulfur K-edge was used to probe the back of a thick Li-S cathode during discharge. Interpretation of the experimental spectra using theoretically derived spectra, and analysis of the fluorescence intensity revealed that lithium polysulfide dianion species formed in the front of the cathode during discharge diffused to the back of the cathode during discharge. Additionally, high conversion of elemental sulfur in the back of the cathode is achieved through chemical disproportionation reactions between elemental sulfur and polysulfide dianion species.

Table of Contents

Table of Contents	i
List of Figures	iv
List of Tables	vi
Acknowledgements	viii
Chapter 1 – Introduction	1
1.1 Lithium sulfur batteries	1
1.2 Lithium sulfur battery problems.....	3
1.3 Characterization of lithium sulfur battery reaction mechanisms	3
1.4 X-ray absorption spectroscopy	4
1.5 Outline of dissertation	8
Chapter 2 – Fingerprinting lithium-sulfur battery reaction products by X-ray absorption spectroscopy.....	9
2.1 Introduction	9
2.2 Experimental Section	11
2.2.1 Materials	11
2.2.2 Lithium polysulfide solutions.....	11
2.2.3 Polymer/polysulfide thin films	12
2.2.4 Lithium sulfide	12
2.2.5 X-ray absorption spectroscopy	13
2.2.6 X-ray overabsorption.....	13
2.2.7 Principal Component Analysis	14
2.3 Results/Discussion	14
2.4 Conclusions	20
2.5 Acknowledgements	21
2.6 Supporting information	22
2.6.1 Effect of air exposure on X-ray absorption spectra.....	22
2.6.2 Equations for the calculation of x_{mix} error.....	22
2.6.3 Sample calculations for x_{mix} error	23
2.6.4 Equations for the calculation of sulfur concentration error	24

2.6.5 Sample calculations for sulfur concentration error.....	24
Chapter 3 – Characterization of Polysulfide Radicals Present in an Ether-based Electrolyte of a Lithium-Sulfur Battery during Initial Discharge using <i>in situ</i> X-ray Absorption Spectroscopy Experiments and First-Principles Calculations.....	26
3.1 Introduction.....	26
3.2. Materials and Methods.....	28
3.2.1. Experimental Section.....	28
3.2.2. Theoretical Calculations.....	30
3.3 Results and Discussion.....	31
3.3.1. Experimental XAS of the Li-S cell at various depths of discharge.....	31
3.3.2. Theoretical XAS of dissolved lithium polysulfides.....	33
3.3.3. Fingerprinting of measured XAS using theory.....	36
3.3.4. Discharge mechanism.....	39
3.3.5. Comparison to previous work.....	40
3.4. Conclusions and Outlook.....	41
3.5 Acknowledgements.....	42
Chapter 4 – Lithium Polysulfide Radical Anions in Ether-Based Solvents.....	43
4.1. Introduction.....	43
4.2. Experimental.....	44
4.2.1 Materials.....	44
4.2.2 Lithium polysulfide solutions.....	44
4.2.3 UV-vis spectroscopy.....	45
4.2.4 Electron paramagnetic resonance spectroscopy.....	45
4.3. Results/Discussion.....	46
4.3.1 UV-vis spectroscopy of lithium polysulfide solutions.....	46
4.3.2 Photographs of lithium polysulfide solutions.....	48
4.3.3 Electron paramagnetic resonance spectroscopy of lithium polysulfide solutions.....	49
4.3.4 Comparison of UV-vis and EPR results.....	52
4.3.5 Determination of polysulfide radical anion concentration in TEGDME.....	53
4.4 Conclusions.....	55
4.5 Acknowledgements.....	56

4.6 Supporting Information	56
4.6.1 UV-vis Spectra Peak Fitting and Parameters	56
4.6.2 EPR Spectra Fitting and Parameters.....	60
Chapter 5 – In situ X-ray absorption spectroscopy studies of discharge reactions in a thick cathode of a lithium sulfur battery	63
5.1 Introduction	63
5.2 Experimental	64
5.2.1 Electrolyte Preparation	64
5.2.2 Cathode Preparation	65
5.2.3 In situ XAS cell	65
5.2.4 Battery Cycling.....	66
5.2.5 Experimental X-ray Absorption Spectroscopy Measurements	67
5.2.6 Data Analysis.....	67
5.3 Results	67
5.4 Conclusions	83
5.5 Acknowledgements	84
5.6 Supporting information	84
5.6.1 Calculation of X-ray penetration depth/fraction of photons reaching each depth.....	84
5.6.2 Fitting of experimental in situ XAS spectra	87
Chapter 6 – Summary	90
Chapter 7 – References	92
Chapter 8 – Appendix	97
Table 8.1 List of symbols.....	97
8.2 Spin coating of SEO thin films	99
8.3 Corrections for X-ray overabsorption	100

List of Figures

Figure 1.1 Schematic of a lithium sulfur battery	1
Figure 1.2 Typical discharge voltage profile for a lithium sulfur battery.....	2
Figure 1.3 Animation of X-ray absorption spectroscopy fluorescence and Auger electron processes	5
Figure 1.4 Example of an X-ray absorption spectrum for FeO	7
Figure 2.1 Sulfur K-edge XAS spectra for $x_{\text{mix}} = 8$ in PEO as a function of film thickness	14
Figure 2.2 Experimentally measured sulfur K-edge XAS spectra of lithium polysulfide species in PEO and SEO at a variety of x_{mix} values	15
Figure 2.3 Scree plot of principal component analysis eigenvalues.....	16
Figure 2.4 XAS spectra of principal components that represent Li_2S_4 , Li_2S , and Li_2S_8	17
Figure 2.5 Ternary diagrams representing the compositions of the measured x_{mix} spectra determined from PCA.....	18
Figure 2.6 Comparison of experimental $x_{\text{mix}} = 6$ and $x_{\text{mix}} = 4$ spectra to calculated spectra based on assumed disproportionation reactions.....	19
Figure 2.S1 XAS spectra of $x_{\text{mix}} = 8$ in SEO after exposure to air	22
Figure 3.1 Experimental Li-S cell schematic and photograph along with the discharge voltage profile of the measured cells and the corresponding sulfur K-edge XAS spectra.....	32
Figure 3.2 First principles calculation of LiS_3 XAS spectrum	34
Figure 3.3 Calculated sulfur XAS spectra for lithium polysulfide radical species.....	36
Figure 3.4 Best fit of the XAS spectrum obtained for the Li-S cell partially discharge to 2.25V	37
Figure 3.5 Comparison of the best fit spectra obtained for each Li-S cell in situ spectrum.....	39
Figure 4.1 UV-vis spectra obtained for TEGDME polysulfide solutions	47
Figure 4.2 UV-vis spectra obtained for PEO lithium polysulfide ($C_s = 10$ mM) solutions	48
Figure 4.3 EPR spectra obtained for TEGDME polysulfide solutions.....	50
Figure 4.4 EPR spectra obtained for PEO polysulfide solutions.....	51
Figure 4.5 Calculated peak areas obtained from UV-vis and EPR double integrals	53
Figure 4.6 UV-vis peak area versus EPR double integral for TEGDME and PEO solutions	53
Figure 4.7 Polysulfide radical anion concentration as a function of sulfur concentration (C_s) and x_{mix} value.....	54
Figure 4.8 Fraction of sulfur present in the form of radical polysulfide species as a function of sulfur concentration (C_s) and x_{mix} value	55
Figure 4.S1 Example fitting of experimental UV-vis spectrum	56
Figure 4.S2 Example fitting of experimental EPR spectrum.....	61
Figure 5.1 Schematic Li-S cell for in situ XAS experiments	66
Figure 5.2 Simplified XAS experiment geometry/schematic	68
Figure 5.3 Voltage discharge profile for in situ Li-S cell	69
Figure 5.4 Sulfur K-edge X-ray absorption spectra obtained for the Li-S cell cathode during first discharge	70
Figure 5.5 Spectral standards used to analyze in situ XAS data.....	71

Figure 5.6 Main edge to pre-edge peak area ratio used to determine x_{av} value for cathode.....	72
Figure 5.7 Composition of cathode determined from analysis of in situ XAS spectra using spectral standards	73
Figure 5.8 Ratio of lithium to sulfur determined through speciation using spectral standards, represented as x_{avall} and x_{avps}	75
Figure 5.9 Analysis of the fluorescence intensity as a function of capacity.....	76
Figure 5.10 Corrected mole fractions of elemental sulfur and polysulfide dianion species in the back of the cathode	78
Figure 5.11 Mole fraction of elemental sulfur determined through spectroscopic analysis versus the fraction remaining based on hypothetical electrochemical reactions	79
Figure 5.12 Illustrative summary of the spectral fraction calculations.....	81
Figure 5.13 Mole fractions of elemental sulfur and all polysulfide dianions in the back of the cathode as a function of capacity	82
Figure 5.S1 Example of the X-ray spectra fitting procedure	87
Figure 8.1 SEO thin film thickness as a function of spin coater spin rate for two solution concentrations of polymer.....	99
Figure 8.2 SEO thin film thickness as a function of spin coat duration for three sets of experimental parameters	100
Figure 8.3 Overabsorbed sulfur K-edge XAS spectra for $x_{mix} = 8$ films of different thickness	103
Figure 8.4 Corrected sulfur K-edge XAS spectra $x_{mix} = 8$ films of different thickness	104

List of Tables

Table 2.1 Experimentally obtained sulfur concentration and x_{mix} values.....	12
Table 2.2 Principal component eigenvalues and IND values	16
Table 2.S1 Data for sample: $x_{\text{mix}} = 2$, PEO, used for sample calculations of x_{mix} error.....	23
Table 2.S2 Data for sample: $x_{\text{mix}} = 2$, PEO, used for sample calculations.....	24
Table 3.1 Exact weights of component spectra used in linear component fits in Figures 3.4 and 3.5.....	38
Table 3.2 Molecular composition of samples I, II, and III in terms of six broad families of species: solid S_8 and Li_2S , radicals, short dianions [Li_2S_x ; $x = 2$ to 5] and long dianions [$x = 6, 7, 8$]	38
Table 4.1 Gaussian peak amplitude and area for 617 nm UV-vis peak at sulfur concentrations (C_S) of 10 mM, 50 mM, and 100 mM.....	47
Table 4.2 Photographs of UV-vis cuvettes filled with TEGDME and PEO lithium polysulfide solutions	49
Table 4.3 Peak areas obtained by double integration of TEGDME and PEO polysulfide solution EPR spectra.....	52
Table 4.S1 UV-vis peak fitting parameters for TEGDME $x_{\text{mix}} = 4$, $C_S = 10$ mM.....	57
Table 4.S2 UV-vis peak fitting parameters for TEGDME $x_{\text{mix}} = 4$, $C_S = 50$ mM.....	57
Table 4.S3 UV-vis peak fitting parameters for TEGDME $x_{\text{mix}} = 4$, $C_S = 100$ mM.....	57
Table 4.S4 UV-vis peak fitting parameters for TEGDME $x_{\text{mix}} = 6$, $C_S = 10$ mM.....	57
Table 4.S5 UV-vis peak fitting parameters for TEGDME $x_{\text{mix}} = 6$, $C_S = 50$ mM.....	58
Table 4.S6 UV-vis peak fitting parameters for TEGDME $x_{\text{mix}} = 6$, $C_S = 100$ mM.....	58
Table 4.S7 UV-vis peak fitting parameters for TEGDME $x_{\text{mix}} = 8$, $C_S = 10$ mM.....	58
Table 4.S8 UV-vis peak fitting parameters for TEGDME $x_{\text{mix}} = 8$, $C_S = 50$ mM.....	58
Table 4.S9 UV-vis peak fitting parameters for TEGDME $x_{\text{mix}} = 8$, $C_S = 100$ mM.....	58
Table 4.S10 UV-vis peak fitting parameters for TEGDME $x_{\text{mix}} = 10$, $C_S = 10$ mM.....	59
Table 4.S11 UV-vis peak fitting parameters for TEGDME $x_{\text{mix}} = 10$, $C_S = 50$ mM.....	59
Table 4.S12 UV-vis peak fitting parameters for TEGDME $x_{\text{mix}} = 10$, $C_S = 100$ mM.....	59
Table 4.S13 UV-vis peak fitting parameters for PEO $x_{\text{mix}} = 4$, $C_S = 10$ mM.....	59
Table 4.S14 UV-vis peak fitting parameters for PEO $x_{\text{mix}} = 6$, $C_S = 10$ mM.....	60
Table 4.S15 UV-vis peak fitting parameters for PEO $x_{\text{mix}} = 8$, $C_S = 10$ mM.....	60
Table 4.S16 EPR peak fitting parameters for TEGDME polysulfide solutions	61
Table 4.S17 EPR peak fitting parameters for PEO polysulfide solutions	62
Table 5.1 Depth of penetration analysis for the Li-S cathode based on the known cathode composition and X-ray absorption coefficients	68
Table 5.S1 Absorption coefficients for each element and mass fractions of each element in cathode and Kapton.....	86
Table 5.S2 Overall absorption coefficients for cathode and Kapton	86
Table 5.S3 Arctangent parameters used for the fitting of each in situ XAS spectrum	87
Table 5.S4 Gaussian peak parameters determined for each in situ XAS spectrum	88

Table 8.1 List of symbols..... 97

Acknowledgements

I would like to start by acknowledging my parents. I would not be who I am or where I am today without their love and support. They taught me the value of education and the importance of hard work. My mom has overcome more challenges in her life than one can ever imagine. The loss of my dad during my first year of graduate school was hard on all of my family, but hardest on her. And yet she was still there to support me through the past five years. I am very proud and grateful to call her my mom. I owe her and my dad the world. My dad is still and always will be an inspiration to me. I would also like to thank my older sisters Stacey and Stephanie, who I have always looked up to and am truly lucky to have as role models. I've learned a great deal just by watching them navigate school, their careers, and life in general. They have also been extremely supportive during my graduate school career. I dedicate this work to my family.

I would also like to thank my advisor Nitash Balsara for his mentorship and support throughout my time at UC Berkeley. I am extremely fortunate to have gotten to work with Nitash, and I am a much better scientist and person because of it. The field of lithium sulfur batteries grew extraordinarily large while I pursued my Ph.D. degree. Nitash's guidance and vision for our project, along with his love for science and his intellect were crucial in navigating this very popular field. Nitash was also incredibly supportive, patient, and understanding during the time after my dad passed away. This speaks volumes about who he is, and I thank him for that.

I also would like to thank those who I collaborated with on this project. David Prendergast and Tod Pascal were critical members of our team and drove the theoretical portion of this work. Their love and curiosity for science led to many interesting discussions that opened up new questions for us to explore. I would also like to thank Alex Teran, who made our lab's first steps into the world of lithium sulfur batteries and has been an invaluable resource to learn about batteries and polymers. He was always very patient in answering questions I had and when I made research mistakes early on. I thank him for being a great colleague and friend. Next, I must thank Rita Wang, who was truly helpful in performing some of the work shown here. Rita is bravely exploring new ways to study Li-S chemistry and I have been impressed with the progress she has already made. I also would like to thank Aditya Raghunathan, an undergraduate student that worked with me on the work shown in Chapter 4. Aditya quickly mastered two types of spectroscopy that our lab had little to no expertise in. I would also like to acknowledge Wayne Stolte, who was very gracious with his time and taught me a lot about designing and building parts/stages for in situ experiments and XAS. At SSRL, Erink Nelson, Matthew Latimer, and Cynthia Patty were always helpful, and generally made life during beamtime easier. I also would like to thank Juan Velasco Velez, Cheng Hao Wu, Jordi Cabana, Jinghua Guo, Yi-De Chuang, Miquel Salmeron, Mukesh Kapalishrami, Melanie Drake and Matthew Marcus for their support, input, and feedback.

I'd also like to thank Professor Yossef Elabd, whose excitement and passion for science is truly contagious and inspired me to do research in his lab at Drexel University and then go to graduate

school. I am very thankful for his guidance and mentorship both during my undergraduate and graduate careers.

In the College of Chemistry, I want to thank Carlet Altamirano, Joseph Nolan, Jessica Chapman, and Fred Deakin for always being helpful. Eric Granlund of the College of Chemistry machine shop was always a great resource to go to and I thank him for his patience and helpfulness.

I am really thankful to have gotten to work alongside so many talented and all around great people in the Balsara lab. Everyone's support, feedback, and friendship has made the lab a great place to do research and grow as a scientist and person. I would like to start by thanking the more senior students in lab when I joined in 2011. Scott Mullin, Greg Stone, Evren Oscam, Keith Beers and David Wong made our lab more of a community rather than a group of independent researchers. They were always willing to give advice and support and were all fun to be around. I also want to thank Dan Hallinan, who brought an energy to science and our group that was always inspiring. Dan was a figurehead in the Balsara lab and the Elabd lab at Drexel. I also would like to thank Anna Javier, whose leadership kept our LBNL labs under control my first couple years. Sebnem Inceoglu Yilmaz was always a great person to go to for advice, and is one of the most kind-hearted and supportive people I have worked with. I did not get to work too much with Inna Gurevitch or Guillaume Sudre, but they were both a pleasure to be around.

I also want to thank Shrayesh Patel. Shrayesh is an extremely patient and thoughtful person who was always willing to answer questions I had and offer valuable advice. I was always impressed by how gracefully and intelligently Shrayesh overcame research challenges. I would also like to thank Nick Young. Nick was a leader in our lab and I was always impressed with his research, particularly because it was outside of the normal scope of our lab's work. I could relate to that having worked on XAS. Nick was the captain of our softball team and brought a lot of us together for some fun times outside of lab. I have a lot of great memories from those times.

I am also particularly grateful for the group of graduate students who I joined the lab with. I have to start by thanking Jacob Thelen, who was an invaluable labmate, roommate, friend, and scientist during my time at Berkeley. Jacob and I spent a lot of time talking about pretty much everything. We may have been less productive when we were around each other, but I think in the end we are both better off because of that. Katherine Harry's boldness and passion as a musician transcends into her talents as a scientist. It was great getting to work with her and see her awesome research come to fruition. It was also a pleasure working alongside of Chae-Young Shin, who was always fun to grab coffee and/or lunch with. Her systematic and well thought out approach to research is impressive, and it's no surprise that she could teach herself how to play guitar during a lab ski trip. Mahati Chintapalli joined our crew during our second year and pretty much instantly was producing some really cool research. She is one of the most interesting people I know and it was always fun to grab lunch and hang out outside of lab with her.

The group of students a year younger has also been a pleasure to work with. Adriana Rojas has been an awesome lab safety coordinator and has done some really interesting work studying single ion conducting block copolymers. Alex Wang and Doug Greer were always great guys to talk and hang out with outside of lab. Despite how different our projects were, they both always had valuable advice and questions. A year younger than those three, Danielle Pesko and Ksenia Timachova joined our lab at the same time and have both done some really impressive research studying polymer electrolytes. Both of them make work a fun place to be and are successfully carrying on the Isothermal PBR torch.

I have also benefited from the support and teachings of some more recent post docs. Didier Devaux has taught me a great deal about batteries, and there seemingly are no boundaries to the novel materials Irune Villaluenga can develop. Chelsea Chen was always a pleasure to work with and was an amazing microscopist and scientist. Mahesh Bhatt has been great to work with and he has been a leader in our LBNL lab space. Pepa Cotanda and Nikos Petzetakis were also a pleasure to work with and I truly enjoyed when they squared off for scientific debates in group meeting.

More recently, our lab has grown with the addition of Whitney Loo, Jackie Maslyn, Deep Shah, and Hee Jeung Oh. This group has brought an awesome new energy to lab and has made the Tan Hall lab a lot of fun to be in. On top of that, I've really been impressed with how quickly they've all jumped into their research and how much they've already accomplished.

I also would like to thank Laura Van Tassel, who has been immensely supportive over the last few years. She has been there for me through all of the highs and lows of graduate school. I am truly grateful for that and hope I can be as supportive as she was for me once she is in law school. I thank her for being a best friend and companion over the past few years.

Lastly, I spent a great deal of my time outside of lab with my past roommates of the Channing Institute: Chris Jakobson, David Liu, Pete Lobaccaro, and Stanley Herrmann. My time in graduate school has been one of the most memorable periods of my life, in large part thanks to these guys. I will always miss sharing a house with them and will forever be grateful for their friendship. I also would like to thank my first year roommates John Alper and Wes Chaney for showing me the grad. school ropes, and my fellow graduate students (particularly the incoming class of 2011) in the CBE department. Thank you all for creating a supportive environment to do work in and for making grad. school such an amazing experience.

Chapter 1 – Introduction

Our society's transition from a petroleum-based energy infrastructure to one that is sustainable and founded on renewable energy resources necessitates improved, highly efficient energy storage technology. Lithium ion batteries are a highly sought after form of energy storage due to their high gravimetric and volumetric energy density, and have transformed the portable electronics industry.⁽¹⁻⁴⁾ The demand for lithium ion batteries continues to grow, as they find use in grid-scale energy storage and transportation applications. Unfortunately, it has become apparent that the maximum energy density that current lithium ion batteries can theoretically achieve is lower than what will be required by future energy intensive technologies (e.g. electric vehicles).⁽²⁾ As a result, it is imperative that new battery chemistries be developed that surpass the theoretical limitations of current lithium ion batteries, and that are both affordable and environmentally responsible.

1.1 Lithium sulfur batteries

One of the most sought after battery chemistries that can fulfill these requirements is the lithium sulfur (Li-S) battery. Lithium sulfur batteries have a theoretical specific energy of 2600 Wh/kg.^(5,6) This is roughly a factor of five times higher than the current standards for lithium ion batteries such as $\text{LiC}_6\text{-LiCoO}_2$ (430-570 Wh/kg).⁽¹⁾ Additionally, sulfur is earth-abundant, affordable, and nontoxic. These characteristics make Li-S batteries an attractive solution to our need for high power, high capacity energy storage technology.

A schematic for a typical Li-S battery in its charged state is shown in Figure 1.1. Here, a lithium metal foil serves as the anode and current collector. The electrolyte separator is generally a porous polymeric material that is not electrically conductive and that is filled with a liquid electrolyte that conducts lithium ions. The cathode is typically prepared by slurry casting a paste that contains elemental sulfur, carbon (for electrical conduction), a binder, and solvent. The solvent is then dried, leaving a highly porous electrode that is then filled with liquid electrolyte (for lithium ion conduction). The electrolyte-filled pores provide channels for lithium ion conduction throughout the cathode. The carbon network allows for electrical conduction.

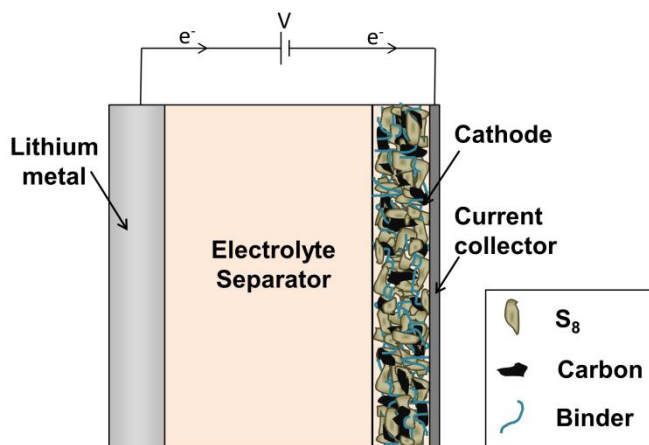


Figure 1.1 Schematic for a charged Li-S cell containing a lithium metal anode, an electrolyte separator, and a cathode consisting of elemental sulfur, carbon, electrolyte, and binder.

During discharge, the reaction that takes place at the cell anode is given by:



while the reaction that occurs at the cathode is given by:



The Li^+ ion generated at the anode travels through the electrolyte separator to reach the S cathode while the e^- travels through the external circuit. The overall reaction mechanism for the cell (per single S_8 molecule) is then given by:



During charging, the reverse of reactions 1.1, 1.2, and 1.3 occur: lithium is redeposited at the anode side of the battery, and Li_2S is oxidized to S_8 . The actual discharge and charge reaction mechanism, however, are much more complicated, and involve a series of electrochemical reactions through which lithium polysulfide reaction intermediates are formed. Lithium polysulfide molecules are chains of sulfur atoms covalently linked together that are anionic and that are coordinated by positively charged lithium ions. These polysulfides come in two forms: lithium polysulfide dianion species (Li_2S_x , $2 \leq x \leq 8$), and lithium polysulfide radical anions (of the form LiS_x , $3 \leq x \leq 5$).⁽⁷⁻¹¹⁾ An example voltage profile for an Li-S battery discharge process is shown in Figure 1.2. Here, the cell voltage starts at roughly 2.45 V, and the cathode only contains S_8 . As discharge begins, S_8 reacts with lithium to form soluble polysulfide species. Lithium polysulfide species are then further reduced to form lithium sulfide. The two voltage plateaus shown in Figure 1.2 are generally attributed to the reduction of solid elemental sulfur to form soluble lithium polysulfide species (first plateau) and the reduction of soluble polysulfide species to form solid lithium sulfide (second plateau).⁽¹²⁾

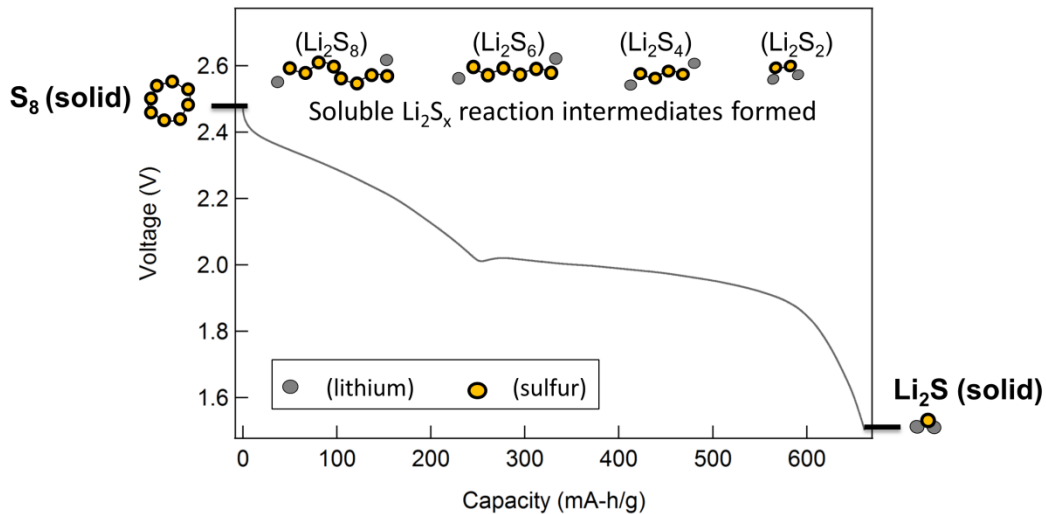


Figure 1.2. Typical discharge voltage profile for an Li-S cell containing two voltage plateaus. Solid elemental sulfur is converted to soluble lithium polysulfide species (first plateau), followed by the reduction of polysulfide species to solid lithium sulfide (second plateau). The polysulfide intermediates

formed during discharge are not limited to the polysulfide species presented above the discharge profile, these are simply shown for example.

1.2 Lithium sulfur battery problems

Many of the issues that lithium sulfur batteries have can be attributed to the high solubility of polysulfide intermediates in typical battery electrolytes. Their formation during charge/discharge leads to their dissolution into the cathode electrolyte and subsequently their diffusion into the electrolyte separator. The diffusion of polysulfide species out of the cathode results in a drop in cell capacity. Additionally, polysulfide species can diffuse to the anode side of the battery where they can react with lithium metal to form an insulating surface-coating of insoluble $\text{Li}_2\text{S}/\text{Li}_2\text{S}_2$. Reactions between polysulfide species and the lithium anode during charging can lead to a shuttle mechanism of polysulfide species between the anode and cathode that results in an infinite charging (i.e. charging of the cell is never completed).⁽¹³⁾ Because of these issues, Li-S batteries fail to achieve their full capacity, and instead are characterized by short lifetimes and low cyclability.

While most Li-S battery research is focused on solving the issue of polysulfide dissolution, many questions still remain regarding the fundamental chemical processes that take place within an Li-S cell. Despite over four decades of research, the reaction mechanisms that govern the charge and discharge processes of Li-S batteries are still unclear. The goal of this work was to fundamentally study the reaction mechanisms through which lithium polysulfide species are formed.

1.3 Characterization of lithium sulfur battery reaction mechanisms

A starting point for studying Li-S battery reaction mechanisms would be to examine how much elemental sulfur and lithium sulfide are present in the cell cathode throughout the course of charge and discharge. Both Li_2S and S_8 are solid state under typical battery conditions, and their crystal structures have been studied extensively.⁽¹⁴⁻¹⁶⁾ Thus, one would expect X-ray diffraction (XRD) to be a clear-cut way to examine the presence or absence of S_8 and Li_2S . This has surprisingly not been the case. In three separate studies, Canas, Lowe, and Nelson et al. used XRD to probe Li-S cathodes during discharge. Canas observed that lithium sulfide (the expected end product of discharge shown in Figure 1.2) formation started at a depth of discharge of 60% (i.e. the discharge process was only 60% complete).⁽¹⁷⁾ Lowe et al. observed that lithium sulfide formation began only at the very end of the discharge process.⁽¹⁸⁾ And Nelson et al. didn't observe any formation of lithium sulfide during/after discharge.⁽¹⁹⁾ The detection of crystalline sulfur after charging has also been controversial. Nelson and Canas both observed the formation of crystalline sulfur at the end of charging^(17, 19), but other authors who performed ex situ XRD on charged cells found no evidence of crystalline sulfur.⁽²⁰⁻²²⁾ The disparity in the results produced by these studies can be attributed to difficulties in performing in situ experiments properly, dissimilarities between in situ and ex situ results, differences in cell composition, and differences in cell performance (i.e. the obtained capacity).

Perhaps the most challenging aspect of studying Li-S reaction chemistry is the unambiguous detection and identification of lithium polysulfide reaction intermediates.⁽²³⁻³⁰⁾ This is largely due to the fact that polysulfide intermediates cannot be isolated from solutions. Thus, spectral standards can only be obtained for polysulfides that are dissolved in solvents.

When in solution, polysulfide species may undergo reversible disproportionation reactions to form a distribution of various polysulfide species of different chain lengths, an example of which is given by reaction equation 1.4:



As a result, attempts to obtain spectral standards for a single polysulfide chain length result in spectra that likely represent a distribution of polysulfide species. Additionally, the distribution of species present in a solution is solvent and temperature-dependent. These issues have prevented researchers from obtaining unambiguous spectral fingerprints with which to analyze in situ spectroelectrochemical data.

Despite the issues mentioned above, X-ray diffraction along with electron microscopy have proven to be insightful techniques to probe the end products of charge/discharge (Li_2S and S_8). However, since these two techniques are incapable of detecting lithium polysulfide species (which, with the exception of Li_2S_2 , are not solid and have no crystal structure), a variety of other spectroscopy techniques have been implemented to study Li-S chemistry. The most popular technique used to study Li-S chemistry has been UV-vis spectroscopy.^(26, 27, 31-40) Unfortunately, while UV-vis has had some success clearly identifying polysulfide radical species, attempts to clearly discern the UV-vis signatures of different polysulfide dianion species have been controversial.^(29, 32) Electron paramagnetic resonance spectroscopy (EPR) has been used to detect the presence of polysulfide radical anions in ex situ mixtures of polysulfide species, and recently an Li-S cell that was studied in situ.^(11, 23, 38, 41-43) This is advantageous to one that is strictly looking to study the presence of radical polysulfide species, but inadequate to one looking to examine elemental sulfur, lithium sulfide, and polysulfide dianions as well. In addition to UV-vis and EPR, Raman spectroscopy, nuclear magnetic resonance (NMR) spectroscopy, and liquid chromatography/mass spectroscopy have also been employed to study Li-S chemistry and distinguish polysulfide dianions.^(6, 31, 44-47) But like UV-vis, attempts to unambiguously identify the signature for different polysulfide dianion species have been inconclusive.

In this work, Li-S battery reaction mechanisms are studied using X-ray absorption spectroscopy (XAS). X-ray absorption spectroscopy is a characterization technique that, prior to 2011, had not been applied to the study of Li-S chemistry. There are several advantages to using XAS compared to other spectroscopy techniques. First is that it is an element specific technique. This allows one to examine only the chemicals that contain a specific element, without interference from other elements that may be present.⁽⁴⁸⁾ XAS is also beneficial because it can measure chemicals in any form. Whereas XRD, for instance, is limited to probing chemicals that are crystalline, XAS can probe chemicals that are crystalline or amorphous, concentrated or dilute. XAS is also guaranteed to always provide information about a sample; whereas other techniques may be ‘silent’ (e.g. EPR will only provide information about a sample if it contains radical species).

1.4 X-ray absorption spectroscopy

The goal of X-ray absorption spectroscopy is to examine the X-ray absorption coefficient of a sample as a function of energy. We are interested in doing this because the absorption coefficient of a measured sample is a reflection of the chemicals that a bulk sample is comprised

of, and can inform one about a chemical's electronic structure. Every molecule has its own XAS signature (or fingerprint), which is essentially the molecule's absorption coefficient as a function of incident X-ray energy. Thus, XAS can be used to determine the composition of a sample that consists of multiple species by deconvolution of the spectrum using spectral standards for individual components. This is particularly useful in the realm of studying chemical reactions. One can obtain the spectral standards for reactants and potential products, and determine what species have formed by probing the reaction in situ.

An explanation of the theoretical basis of XAS begins with a description of what takes place when X-ray photons interact with atoms. When an X-ray photon encounters an atom and has an energy that is equal to or greater than the binding energy of one of the atom's core shell electrons, the photon will be absorbed (i.e. destroyed), and the core shell electron will become excited. If the incident photon has an energy that is less than the binding energy, the core shell electron will remain unprovoked. The point at which an X-ray photon has an energy that is equal to the binding energy of a core shell electron is referred to as the element's absorption edge.^(48, 49) The excitation of a core shell electron creates a 'core hole'. The filling of this hole occurs within femtoseconds, and proceeds through one of two processes. First, an electron from a higher shell drops to the core hole and in doing so releases an X-ray fluorescent photon. The emitted fluorescent photon has a well-defined energy that is characteristic of the atom's emission lines (e.g. $K\alpha$). The second process also begins with an electron from a higher shell dropping to fill the core hole. However, instead of releasing energy in the form of fluorescence, the decaying electron ejects another electron. This process is referred to as the Auger Effect.^(48, 49) The fluorescence and Auger modes of decay are shown in Figure 1.3.

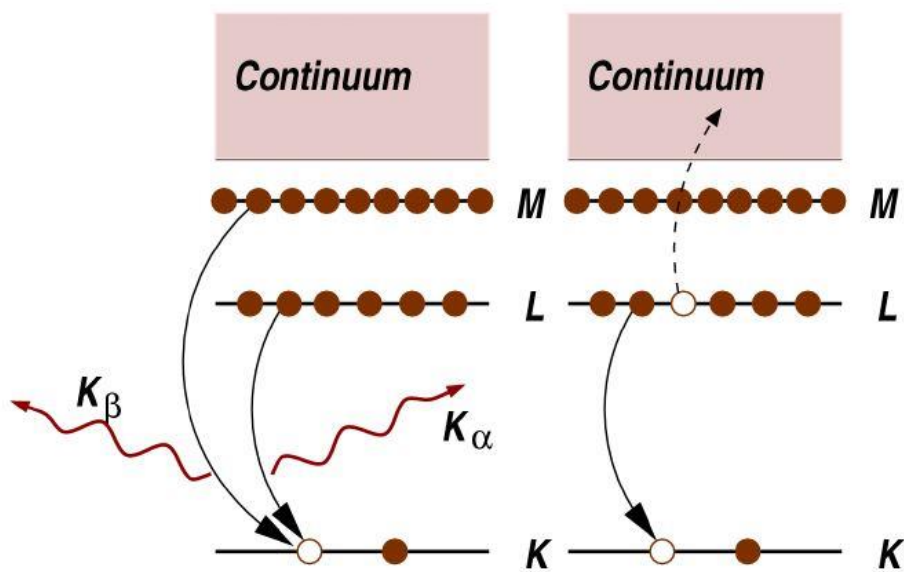


Figure 1.3 Animation showing the two decay processes that take place after a core shell electron has been excited and a core hole is produced after an atom's absorption of an X-ray photon. The decay of an outer shell electron can create fluorescent photons (left) and Auger electrons (right). This image is taken from reference⁽⁴⁹⁾.

In all XAS experiments, the incoming X-ray photon energy is scanned upward while the absorption coefficient of the sample is measured. The experiment begins at X-ray energies that

are well below the absorption edge in order to obtain an accurate baseline measurement of ‘background’ absorption (i.e. the absorption of all other elements and non-resonant absorption of the atom being examined). The X-ray energy is then scanned through the absorption edge and to a final energy, which is chosen based on the goal for the experiment. The simplest method to measure the absorption coefficient relies on Beer’s law:

$$I = I_0 e^{-\mu(E)\rho t} \quad (1.5)$$

Here, the incoming X-ray intensity (I_0) is related to the outgoing X-ray intensity (I) via an exponential function that contains the sample thickness (t), the sample density (ρ), and the sample’s absorption coefficient ($\mu(E)$), which is a function of the incoming X-ray energy (E). In practice, one measures I and I_0 (for instance using a photodetector), and relates changes in these intensities to the absorption coefficient:

$$\mu(E) = -\frac{1}{\rho t} \log\left(\frac{I}{I_0}\right) \quad (1.6)$$

While X-ray transmission mode is the simplest approach to measuring a sample’s absorption coefficient, it is often not the most convenient. For instance, in the case when X-ray’s cannot fully penetrate through a sample (e.g. when the element being probed is present in high concentrations, or the element’s absorption edge is in the soft X-ray regime).^(48, 49) When transmission mode of measurement is not viable, the absorption coefficient can be measured in fluorescence mode or electron yield mode.

In fluorescence mode, the fluorescent photons emitted during the excitation/decay process are measured by a fluorescent detector, and are directly related to the absorption coefficient. In electron yield mode, one measures the electrons that were emitted from the atom as a result of the Auger Effect. Since the escape depth for emitted electrons is generally low, electron yield mode is generally considered to be surface sensitive, while fluorescence mode is considered to be bulk sensitive.⁽⁴⁹⁾ In either case, the magnitude of measured fluorescence or emitted electrons is directly proportional to the absorption coefficient:

$$\mu(E) \propto \frac{I_f}{I_0} \quad (1.7)$$

Equation 1.7 holds only under special circumstances, and is considered to be a highly simplified and ideal representation of the relationship between the absorption coefficient and measured X-ray intensities. For more information on this, see Appendix 8.3 and references⁽⁵⁰⁻⁵²⁾.

XAS experiments are split into two types based on the range of incoming X-ray energies examined, which is inherently related to the purpose of the experiment. In an X-ray absorption near edge spectroscopy (XANES) experiment, absorbed X-ray photons have enough energy to excite to the core shell electron to the lowest unoccupied molecular orbital (LUMO) of the atom.⁽⁴⁸⁾ When incoming X-ray photons have energy equal to the amount required to excite the core shell electron to the LUMO, there will be an increase in the amount of absorption measured. And thus, the measured absorption coefficient is a direct reflection of an atoms electronic structure. XANES experiments provide insight regarding the atom’s oxidation state, local environment, and what the atom is bound to. XANES is a particularly effective probe of an

atom's oxidation state. When an atom has a net negative charge (e.g. in the case of polysulfide anions) the amount of energy required to excite a core shell electron is reduced as a result of electronic shielding of the nucleus. This results in a measured absorption peak at X-ray energies below the absorption edge of neutrally charged atoms. When an atom is oxidized (i.e. the atom has a net positive charge) the opposite effect takes place, and more energy is required to excite the core shell electron. This results in a measured absorption peak above the expected absorption edge.⁽⁵³⁾

When incident X-rays have energies greater than the LUMO level, the excited core shell electron will be released from the atom, thereby ionizing the atom. The ejected photoelectron is wave-like, having a wavelength that reflects the energy originally imparted on the electron by the incident X-ray photon. The photoelectron wave will then interact with backscattered waves from nearby atoms.^(48, 49) The constructive or deconstructive interference with backscattered waves leads to oscillations in the measured absorption coefficient, and a departure from the expected free-atom absorption coefficient (i.e. the absorption coefficient of the atom in an environment with no local structure or periodicity). This type of experiment is referred to as EXAFS, and generally deals with X-ray energies beginning above the LUMO energy and going as far out as 1 keV above the absorption edge.

Figure 1.4 shows an example of a normalized iron K-edge X-ray absorption spectrum for FeO. If a measured atom were completely isolated, the measured absorption coefficient would essentially be a step function followed by a smooth background. In Figure 1.4, this is represented by $\mu_0(E)$. Instead, due to changes in bonding, oxidation state, local environment, and overall electronic structure, the measured absorption coefficient is given by $\mu(E)$. The value of $\mu(E)$ that is plotted in Figure 1.4 has been normalized to $\mu_0(E)$. Figure 1.4 also shows the general areas of an absorption spectrum that correspond to XANES and EXAFS measurements. XANES measurements typically refer to the first 30 or so eV above the absorption edge, while EXAFS experiments extend out to as high as 1000 eV above the absorption edge. In this work, we will focus on the XANES region of XAS.

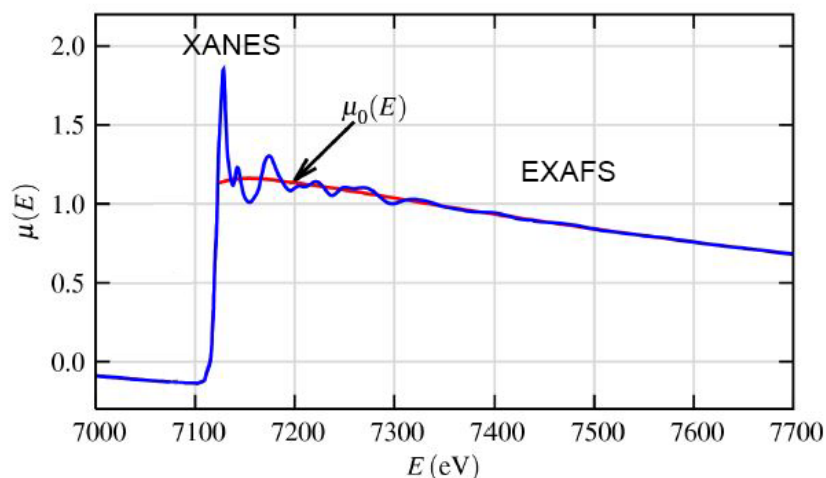


Figure 1.4 Example XAS spectrum: iron K-edge spectrum of FeO. Adapted from ref⁽⁴⁹⁾

Like other spectroscopy techniques, XAS can be applied to the study of Li-S redox chemistry through in situ spectroelectrochemical approaches. Again, however, we encounter the

issue of obtaining spectral standards for individual polysulfide molecules. The novelty of the work presented herein is that the obtained in situ spectra were analyzed using theoretically calculated spectra. Spectral standards for polysulfide intermediates were obtained by performing first principles molecular dynamics calculations and spectral simulations using the excited electron and core hole (XCH) density functional theory (DFT) approach. This allowed us to obtain spectral standards for single polysulfide species, rather than mixtures of polysulfide dianion. These simulations were performed by Tod Pascal and David Prendergast of Lawrence Berkeley National Laboratory. Details regarding the computational approaches used to develop the spectra can be found in references.⁽⁵⁴⁻⁵⁶⁾

1.5 Outline of dissertation

In this work, X-ray absorption spectroscopy is used to study lithium sulfur battery reaction mechanisms and lithium polysulfide reaction intermediates in a variety of different ways. In Chapter 2, we begin by developing the sulfur K-edge XAS spectral standards for lithium polysulfide dianion species. Spectra obtained for ex situ mixtures of lithium polysulfide species in an ether-based block copolymer solvent are examined using principal component analysis. In Chapter 3, XAS is used to probe Li-S cells that have been discharged to different depths of discharge. The notable result of this chapter is that polysulfide radical anions were detected in the cell electrolyte. This result was unexpected, and inspired the work presented in Chapter 4. In Chapter 4, the stability of and presence of polysulfide radical anions in ether-based solvents is investigated using UV-vis spectroscopy coupled to EPR spectroscopy. The concentration of radical species as a function of sulfur concentration and average polysulfide chain length are reported. In Chapter 5, sulfur K-edge XAS is used to examine the cathode of a thick Li-S cathode during discharge. Here, electrochemical reactions between sulfur and lithium are likely to preferentially occur at the front of the cathode. Interestingly, XAS reveals that polysulfide species formed in the front of the cathode diffuse to the back of the cathode during discharge. Additionally, high conversion of elemental sulfur is observed as a result of chemical reactions between short chain polysulfide dianions and elemental sulfur.

Chapter 2 – Fingerprinting lithium-sulfur battery reaction products by X-ray absorption spectroscopy[†]

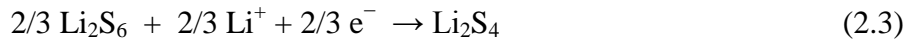
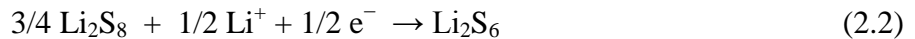
ABSTRACT

Lithium-sulfur batteries have a theoretical specific energy that is a factor of five greater than that of current lithium-ion batteries, but suffer from consequences of the solubility of lithium polysulfide reaction intermediates that form as the batteries are charged and discharged. These species can react with each other and diffuse out of the cathode, causing battery capacity and ultimately, cell failure. In spite of work that has spanned four decades, "fingerprints" of polysulfides have not yet been established, precluding a systematic study of lithium-sulfur chemistry. Herein we demonstrate the use of principal component analysis of X-ray absorption spectroscopy (XAS) to obtain fingerprints of lithium polysulfides. This approach enables interpretation of spectral data without any assumptions regarding the origin of the observed spectral features or knowledge of the stability of the polysulfide species of interest. We show that in poly(ethylene oxide)-based solid electrolytes containing polysulfides made by chemically reacting Li₂S and elemental sulfur, Li₂S₂ and Li₂S₆ spontaneously disproportionate to give binary Li₂S/Li₂S₄ and Li₂S₄/Li₂S₈ mixtures, respectively, while Li₂S₄ and Li₂S₈ exist as single molecular species. XAS fingerprints of Li₂S₄ and Li₂S₈ are thus presented.

2.1 Introduction

Lithium-sulfur batteries have become a popular focus of energy storage research due to their high theoretical specific energy (2600Wh/kg), which is over five times greater than current lithium-ion battery technology. Compared to active materials like cobalt oxide and iron phosphate, elemental sulfur is abundant, nontoxic and inexpensive.⁽⁵⁷⁻⁵⁹⁾ The reaction mechanism through which the battery provides energy is a complex, multi-step process. The reaction scheme that is often proposed is shown below:

Scheme 1: Proposed lithium-sulfur reduction reaction pathway



In its simplified form, the overall reduction mechanism can be written as: $\text{S}_8 + 16 \text{Li}^+ + 16 \text{e}^- \rightarrow 8 \text{Li}_2\text{S}$. The intrinsic advantages of Li-S chemistry are unfortunately overshadowed by issues stemming from the fundamental properties of the Li₂S_x ($2 \leq x \leq 8$) intermediates. Due to their high solubility in common battery electrolytes, Li₂S_x species can diffuse out of the cathode

[†]This work was reported in *J. Electrochem. Soc.* **161**, A1100 (2014)

during cycling and participate in a parasitic shuttle between electrodes, resulting in capacity fade and self-discharge.⁽¹³⁾ Additionally, Li_2S_x species that diffuse to the battery anode can be irreversibly reduced to form an insulating layer of Li_2S and Li_2S_2 between the electrolyte and the negative electrode surface. These issues limit cycle life and ultimately lead to cell failure.

While a vast amount of Li-S battery research has been and is increasingly focused on solving issues related to polysulfide dissolution,⁽⁶⁰⁻⁶²⁾ the complex reaction mechanisms through which Li_2S_x intermediates form remain unclear.⁽³¹⁾ Sulfur reduction by lithium has been studied for over four decades, but has historically been a point of contention among researchers.^(8, 26, 40, 63) Typical approaches to examine the reaction have involved spectroelectrochemistry.^(26, 40, 44, 46) Here, electrochemical techniques (e.g. cyclic voltammetry and galvanostatic processes) are coupled with spectroscopy in an attempt to obtain spectral evidence of reaction intermediates. Spectral data obtained from these in situ experiments is interpreted by comparison to ex situ standards collected for various Li_2S_x intermediates.

Spectroelectrochemical approaches can provide powerful insight into Li-S redox pathways, as they probe chemistry in its native, unaltered environment. However, obtaining spectral fingerprints of Li_2S_x species has been problematic. Polysulfide intermediates cannot be isolated,⁽⁶⁴⁾ and thus the fingerprints must be gathered of polysulfides dissolved in specific solvents. In solution, Li_2S_x molecules may undergo reversible disproportionation reactions to form a distribution of different Li_2S_x species via reactions equations (2.6), (2.7) and (2.8) shown in Scheme 2^(25, 31):

Scheme 2: Proposed lithium polysulfide disproportionation reactions



where $m \leq x - 1$ for reactions 2.6 and 2.7, and $m \geq x$ for reaction (2.8). Attempts to obtain standards for single Li_2S_x intermediates may instead yield spectra that represent a distribution of polysulfide molecules. It is evident from Scheme 2 that a given polysulfide solution could contain many more than one molecular species. For example, S_6^{2-} could disproportionate to give S_4^{2-} and S_8^{2-} [reaction (2.7) of Scheme 2 with $x = 6$ and $m = 2$] but S_4^{2-} thus obtained may then disproportionate into other products [e.g. S_3^{2-} and S_5^{2-} ; reaction (2.7) of Scheme 2 with $x = 4$ and $m = 1$]. Additionally, the distribution of polysulfide species present is highly dependent on the medium.^(33, 65) In one of the earliest UV-vis absorption spectroscopic studies of lithium polysulfides, Rauh et al. showed that spectra of lithium polysulfide solutions with identical ratios of Li:S were drastically different when THF and DMSO were solvents.⁽⁸⁾ This was taken as a signature of different extents of disproportionation of the same lithium polysulfides in the two solvents. Obtaining unambiguous spectral fingerprints of polysulfide species has been difficult due to these issues and this has prevented researchers from reaching conclusive agreement regarding Li-S redox pathways.

X-ray absorption spectroscopy (XAS) is a well-established probe of local environment and the electronic structure of the atom of interest.^(48, 66, 67) XAS in the vicinity of the sulfur K-edge is a potentially powerful technique for differentiating lithium polysulfide species. To our

knowledge, XAS at the sulfur K-edge has been used to study Li-S chemistry in two previous publications. Gao et al. were the first to report XAS spectra of lithium polysulfides in battery electrolytes. However, they did not attempt to determine the relationship between measured spectra and specific polysulfide molecules that were present in the cathode.⁽⁶⁸⁾ More recently, Cuisinier et al. performed XAS studies of Li-S cathodes containing sulfur-imbibed spherical carbon shells.⁽⁶⁹⁾ They acknowledged the difficulty of interpreting measured X-ray absorption spectra due to the lack of Li_2S_x spectral standards. The determination of what polysulfide(s) spectra represent has always required auxiliary insight regarding polysulfide disproportionation.^(25, 31) It has not been possible to prove that the measured spectra correspond to a unique polysulfide distribution due to the complexity of reactions in Scheme 2 above.

The distinguishing feature of the present work is the use of a rigorous approach to XAS data analysis without auxiliary insight, i.e. we do not assume the presence or absence of any given polysulfide species. To do this, we employ the principal component analysis (PCA) technique as a way to determine the number of polysulfides obtained spectra represent. In previous applications to interpret XAS spectra of multicomponent systems, PCA has been used to identify different oxidation states and local environments of vanadium centers during catalytic oxidation,⁽⁷⁰⁾ speciate humic acid constituents in soil,⁽⁷¹⁾ and elucidate the number and types of Mn-containing species in particulates emitted by gasoline engines.⁽⁷²⁾

While previous work⁽⁶⁹⁾ has probed Li_2S_x species as they exist in cathodes containing liquid electrolytes, we probe Li_2S_x molecules as dilute species dissolved in solid polymer films with thicknesses below 200 nm. This combination of sulfur concentration and sample geometry is essential for obtaining spectra that are not affected by X-ray overabsorption.⁽⁷³⁾

2.2 Experimental Section

2.2.1 Materials

A PEO homopolymer ($M_n = 50$ kg/mol) sample was obtained from Polymer Source, Inc. An SEO diblock copolymer was synthesized on a high vacuum line via sequential anionic polymerization,⁽⁷⁴⁾ having polystyrene and poly(ethylene oxide) block molecular weights of 60 kg/mol and 63 kg/mol, respectively. Sulfur (S_8) and lithium sulfide (Li_2S) were received under argon from Alfa Aesar, opened in an argon-filled glovebox, and used as received.

2.2.2 Lithium polysulfide solutions

Samples for XAS experiments were prepared by spin-coating thin films of SEO and PEO containing lithium polysulfide molecules onto silicon wafers (thicknesses ranging from 120-950 nm). Polysulfide/polymer/solvent solutions for spin-coating were prepared by mixing Li_2S and S_8 with either PEO or SEO in either *n*-methylpyrrolidone (NMP) for the Li_2S_x spectra comparison study, and dimethylformamide (DMF) for the overabsorption study. DMF is more volatile than NMP, which allowed us to obtain films as thick as 950 nm by spin-coating followed by drying. Solutions were mixed in sealed vials for three days at 90°C.⁽⁸⁾ The lithium to sulfur ratio in our samples is quantified by the parameter x_{mix} . The moles of S_8 per mole of Li_2S in our systems is $(x_{\text{mix}} - 1)/8$. If a single polysulfide species were formed by our reaction, then we would obtain:



Amounts of PEO and SEO were added to each solution to obtain solution concentrations of either 50 mg polymer/mL or 100 mg polymer/mL of solvent; higher concentrations were used to obtain thicker samples. Overall sulfur concentration in polymer thin films was kept constant at 0.447 g S/g polymer for each solution. Detailed information regarding obtained x_{mix} values and sulfur concentration for each sample can be found in Table 2.1. Calculations for the errors expressed in Table 2.1 can be found in the Supporting Information.

Table 2.1 Experimentally obtained sulfur concentration and x_{mix} values

Sample Name	Concentration (g S/g polymer)	x_{mix}
$x_{\text{mix}} = 2$, PEO	0.452 ± 0.002	1.99 ± 0.003
$x_{\text{mix}} = 4$, PEO	0.443 ± 0.002	4.03 ± 0.021
$x_{\text{mix}} = 6$, PEO	0.455 ± 0.002	6.38 ± 0.076
$x_{\text{mix}} = 8$, PEO	0.433 ± 0.002	8.37 ± 0.165
$x_{\text{mix}} = 2$, SEO	0.441 ± 0.002	2.01 ± 0.003
$x_{\text{mix}} = 4$, SEO	0.453 ± 0.002	4.20 ± 0.022
$x_{\text{mix}} = 6$, SEO	0.440 ± 0.002	5.97 ± 0.063
$x_{\text{mix}} = 8$, SEO	0.434 ± 0.002	8.47 ± 0.159

Solutions for $x_{\text{mix}} = 2$ were found to contain small amounts of precipitated solids. The reason for this will be addressed shortly. These mixtures were vigorously homogenized before solution was drawn for spin coating. There were no visible signs of precipitation in any of the other solutions ($x_{\text{mix}} = 4, 6,$ and 8).

2.2.3 Polymer/polysulfide thin films

Thin films of polysulfide-containing polymer electrolyte were obtained by spin coating onto silicon wafers. Spin coating was performed in an argon-filled glovebox at room temperature. Parameters used to obtain films of different thickness ranged from 1000 – 4000 RPM, and 30 – 60 seconds of spin time. Films were allowed to dry at room temperature to prevent the sublimation of sulfur. Films were spin coated using a Chemat KW-4A spin coater. Film thickness was measured using ellipsometry (α -SE Ellipsometer, J.A. Woolman Co., Inc.).

2.2.4 Lithium sulfide

In addition to the polymer film samples above, XAS measurements were also taken for Li_2S (lithium sulfide). Attempts to dissolve Li_2S in polymer/solvent were unsuccessful, and thus, samples of Li_2S for XAS consisted of pure Li_2S powder. This powder was lightly dusted onto sulfur-free tape and measured in fluorescence mode.

2.2.5 X-ray absorption spectroscopy

X-ray absorption spectra were obtained at beamline 4-3 of the Stanford Synchrotron Radiation Lightsource (SSRL) and were taken in fluorescence mode using a 4-element silicon Vortex detector. Energy calibration was carried out using thiosulfate, setting the first peak centroid to 2472.02 eV. Spectra were taken for a range of 2440 to 2575 eV with an energy resolution as low as 0.08 eV near the absorption edge. Three consecutive scans were taken for each sample without any movement of the sample stage between scans and then averaged for further data analysis. No differences were observed between consecutive scans. X-ray spectra were normalized and background subtracted using SIXPACK.⁽⁷⁵⁾

To prevent the exposure of samples to air, samples were transferred from the glovebox at Lawrence Berkeley National Laboratory (LBNL) in an argon-filled desiccator to the Stanford Synchrotron Radiation Lightsource (SSRL) where they were placed in an argon-filled glovebox. Samples were transferred from the glovebox to the beamline endstation via an air-tight container and loaded into the helium-filled measurement chamber through a helium-filled glovebag equipped with an oxygen sensor. The effect that air-exposure has on obtained spectra was examined as shown in the Supporting Information.

2.2.6 X-ray overabsorption

Interpretation of XAS spectra is simplified in the absence of overabsorption (sometimes referred to as self-absorption in literature), a phenomena that occurs for samples that are too thick or too concentrated.^(51, 76, 77) Spectra affected by overabsorption tend to display dampened spectral features with strong relative absorption and, hence, enhanced spectral features with weak relative absorption. This would likely lead to spurious relative intensities between observed pre- and main-edge features in our S K-edge, and, as we will show, these two spectral features are critical for determining the distribution of polysulfide species in samples. To elucidate the effect of overabsorption on Li_2S_x spectra, thin films of PEO containing $x_{\text{mix}} = 8$ were spun cast to obtain a range of thicknesses; sulfur K-edge spectra were obtained for each thickness. In Figure 2.1a we show XAS spectra at selected film thicknesses. The intensity of the main-edge peak occurring at 2472.7 eV is plotted as a function of film thickness in Figure 2.1b. The main-edge peak intensity is 2.98 ± 0.02 when film thickness is less than 200 nm. In contrast, the main-edge peak intensity of films with thickness greater than 200 nm is significantly lower, reaching a value of about 2.71 as film thickness exceeded 900 nm. The XAS spectra of samples with thicknesses between 135 and 175 nm were almost indistinguishable from each other (see Figure 2.1a). Thus, to mitigate the effects of overabsorption, the samples used to obtain spectra shown throughout the remainder of this work were all cast to be between 120 and 180 nm.

The effect of overabsorption is also dependent on the overall concentration of sulfur atoms in a sample. For this reason, all samples contained an equivalent overall sulfur concentration of 0.447g S/ g polymer. No mathematical corrections for overabsorption were performed on the data presented here.

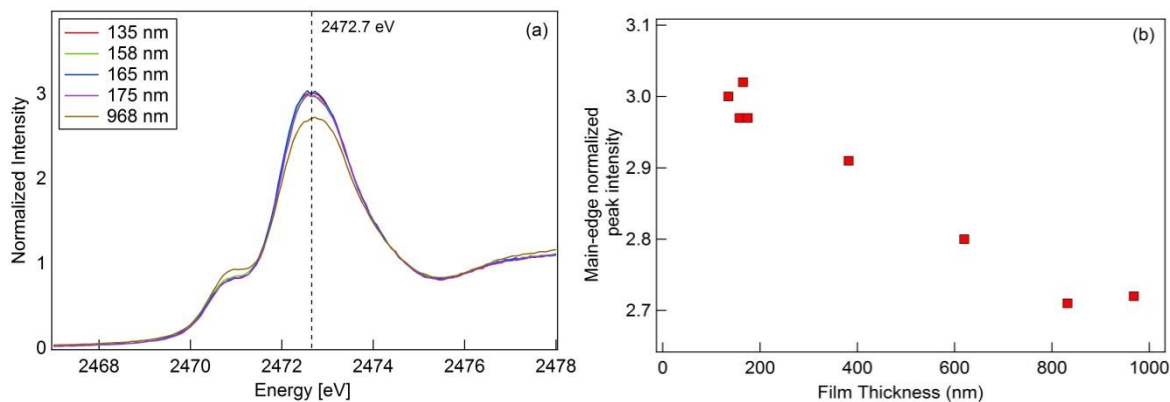


Figure 2.1 (a) XAS spectra in the vicinity of the sulfur K-edge of thin films of $x_{\text{mix}} = 8$ samples in PEO with different film thicknesses. (b) Main-edge peak intensity as a function of film thickness; the decrease in intensity is due to X-ray overabsorption.

2.2.7 Principal Component Analysis

The PCA was performed using algorithms described by Ressler.⁽⁷²⁾ In brief, PCA works by reducing the dimensionality of the X-ray spectra dataset by finding independent components that, through linear combination, can be used to simulate experimental data within statistical significance.⁽⁷⁸⁻⁸¹⁾

2.3 Results/Discussion

We begin our analysis by examining sulfur K-edge XAS data collected for polysulfide-containing polymer electrolyte thin films. Figure 2.2a,b show the normalized sulfur K-edge spectra collected for samples having x_{mix} values of 2, 4, 6, and 8 dissolved in solid thin films of PEO and SEO at a constant sulfur concentration of 0.447 g S / g polymer. Spectra obtained from SEO and PEO mixtures for a given value of x_{mix} are nearly indistinguishable (Figures 2.2a and 2.2b). Also shown is the XAS spectrum for pure Li_2S powder (Figure 2.2c).

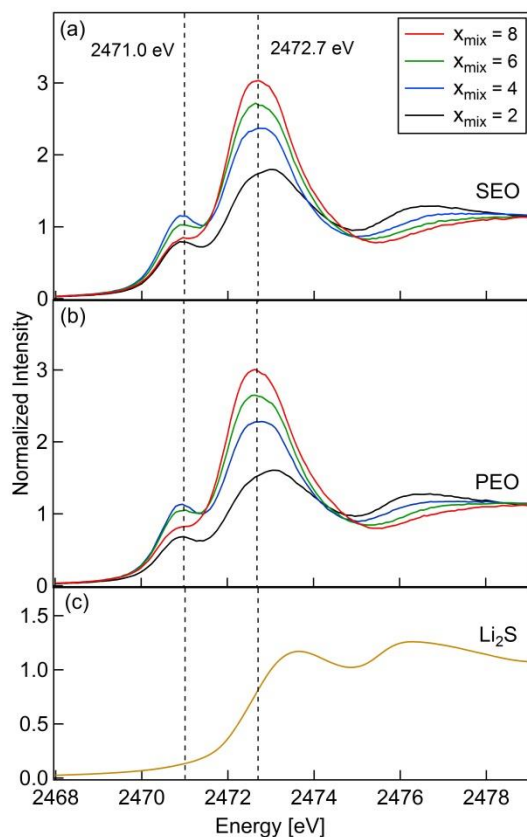


Figure 2.2 Experimentally measured sulfur K-edge XAS spectra of $\text{Li}_2\text{S}_{x_{\text{mix}}}$ in polymer thin film samples (thicknesses less than 180 nm) in (a) SEO and (b) PEO at a sulfur concentration of 0.447 g S/g polymer, and (c) pure Li_2S powder lightly dusted onto sulfur-free tape.

The energy range over which XAS data are obtained in this study (Figure 2.2) are in close proximity to the sulfur K-edge. It is well known that data obtained in this regime, often referred to as X-ray absorption near-edge structure (XANES) spectra, are similar to other forms of absorption spectra known in chemistry, wherein the measured signal reflects the molecular species present in solution. Given that XAS is a bulk spectroscopic technique, the resulting XANES region is due to the weighted average of the XANES of all molecular species present in the sample. If reference spectra for known species are available, then linear least-squares fitting may be used to measure the fractions of each species represented by each spectrum. While we have obtained a reference spectrum for Li_2S , no such spectra exist for Li_2S_x species ($2 \leq x \leq 8$). We must use statistical methods to interpret the data shown in Figure 2.2. PCA seeks to describe the set of spectra as weighted sums of a smaller number of "component" spectra, the relative importance of which is measured by the "eigenvalue" of each component. Semi-empirical methods exist to determine the minimum number of components required to describe a given dataset.⁽⁷⁹⁾ Results of the application of PCA to the dataset of nine experimental spectra ($\text{Li}_2\text{S}_{x_{\text{mix}}}$ in PEO & SEO, and Li_2S) are shown in Figure 2.3, where components are rank-ordered according to the magnitude of their corresponding eigenvalue (also known as a scree plot).⁽⁷⁸⁾ Note that our analysis is restricted to four different x_{mix} compositions: $x_{\text{mix}} = 2, 4, 6, 8$ in PEO & SEO. On a semi-log plot, there is a kink which separates the first three components from the rest, suggesting that the systems of interest contain three underlying components. These are our

principal components. Reconstruction of the data using these three components shows satisfactory agreement with the original spectra.

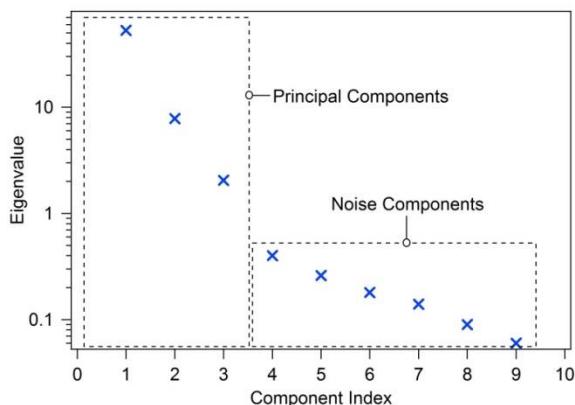


Figure 2.3 Scree plot of principal component analysis eigenvalues

Another approach for distinguishing between noise and principal components was proposed by Malinowski, who suggests calculating the value indicator function (IND).⁽⁷⁹⁾ The values of IND obtained for each component are shown in Table 2.2 along with their eigenvalue. The distinction between principal and noise components is predicted to occur at the component index where IND is a minimum. As seen in Table 2.2, this occurs for the component index of three. It is thus evident both from the scree plot and the IND analysis that the XAS spectra from our collection of samples contain three principal components.

Table 2.2 Principal component eigenvalues and IND values

Principal Component	Eigenvalue	IND values
1	53.0	4.47e-2
2	7.81	1.63e-2
3	2.05	6.11e-3
4	0.40	6.47e-3
5	0.26	7.76e-3
6	0.18	1.13e-2
7	0.14	1.88e-2
8	0.09	6.08e-2
9	0.06	-

The abstract component spectra generated by the PCA procedure contain unphysical features (e.g. negative absorption values in the energy range of interest). The standard procedure

to obtain X-ray spectra that do not contain such unphysical features is the iterative transformation factor analysis (ITFA) as described in reference.⁽⁸²⁾ In this step of the analysis, one constructs new “components” from weighted sums of the abstract components in such a way that the amounts of each ITFA component required to fit all spectra are between 0 and 1 and as different from each other as possible. This method has been shown to result in ITFA spectra which often represent molecular species or combinations of a small number of molecular species. ITFA was applied to the results of the PCA and the computed spectrum of principal components one, two and three are shown in Figure 2.4. The weightings of each computed spectrum needed to recreate the experimentally measured spectra for all our samples were calculated and the results are plotted on a ternary composition diagram in Figure 2.5a.

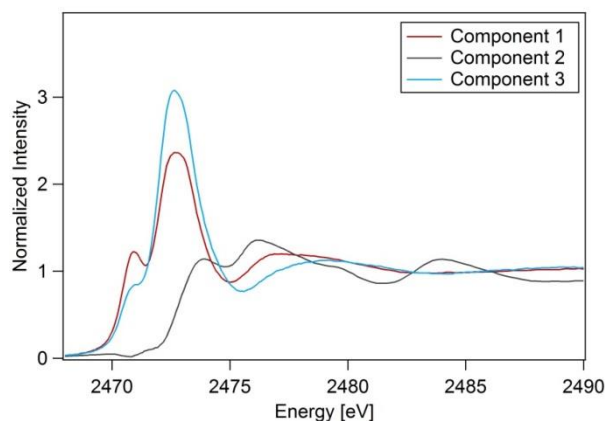


Figure 2.4 X-ray absorption spectra of principal components obtained from analysis of the full XAS data set. Components 1, 2, and 3 are identified as Li_2S_4 , Li_2S and Li_2S_8 , respectively, based on the parsimonious interpretation of the full XAS data set.

Each corner of the ternary diagram represents the spectrum of one of the principal components shown in Figure 2.4, and binary mixtures of components are located along the sides of the triangle. The bracketed numbers near the corners of the ternary composition diagram in Figure 2.5 represent the specific components identified in Figure 2.4. It is remarkable that all of our samples are located either near the corners or the sides of the ternary diagram. This indicates that our samples are, to a good approximation, either single component or two component mixtures. It is evident in Figure 2.5a that Li_2S is located very close to the corner corresponding to component 2. We know for a fact that our Li_2S sample is a pure component. We thus expect the PCA to interpret the Li_2S data as such. The fact that the Li_2S data point in Figure 2.5a is not exactly at the apex of the triangle may be due to noise in the data and limitations of the PCA approach. Recognizing this, we still assert that component 2 is Li_2S . Note the similarity between the XAS spectrum of component 2 obtained by the PCA (Figure 2.4) and the measured spectrum of Li_2S (Figure 2.2c).

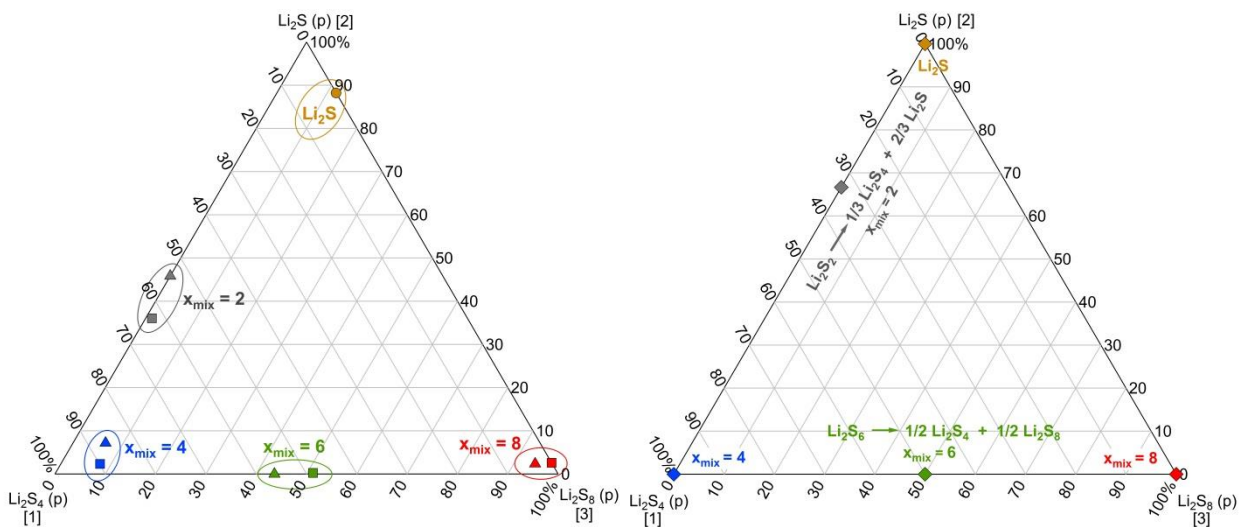


Figure 2.5 (left) Compositions of $\text{Li}_2\text{S}_{x_{\text{mix}}}$ and Li_2S samples plotted on a ternary diagram, determined by principal component analysis of the full XAS data set. Samples that lie near the corners are, to a good approximation, one-component systems. Samples that lie near the sides of the triangle but away from the corners are, to a good approximation, two-component systems. Squares and triangles represent polysulfides dissolved in SEO and PEO, respectively. (right) Theoretical ternary composition diagram of $\text{Li}_2\text{S}_{x_{\text{mix}}}$ and Li_2S samples if only the $x_{\text{mix}} = 2$ and $x_{\text{mix}} = 6$ samples participated in disproportionation reactions as shown. Qualitative agreement between the experimental and theoretical ternary composition diagrams supports the proposed disproportionation scheme (see text for details).

The bottom left corner of the triangle in Figure 2.5a represents principal component 1 and the bottom right, principal component 3. Samples of $x_{\text{mix}} = 4$ are located near the bottom left corner of the diagram, while $x_{\text{mix}} = 8$ are located near the bottom right corner. The parsimonious interpretation of these observations is that principal component 1 is Li_2S_4 and principal component 3, Li_2S_8 . The component corners in Figure 2.5a are thus labeled $\text{Li}_2\text{S}(\text{p})$, $\text{Li}_2\text{S}_4(\text{p})$ and $\text{Li}_2\text{S}_8(\text{p})$, where ‘(p)’ denotes the fact that these assignments originate from the PCA. We have thus established a correspondence between the abstract *components* determined by PCA and molecular *species*.

Figure 2.5a shows that the $x_{\text{mix}} = 2$ samples are, to a good approximation, binary mixtures of Li_2S_4 and Li_2S . It is thus evident that Li_2S_2 species do not exist in the $x_{\text{mix}} = 2$ mixtures. Specifically, Li_2S_2 disproportionates into Li_2S and Li_2S_4 . The fact that the $x_{\text{mix}} = 2$ data lie on the Li_2S — Li_2S_4 side of the triangle in Figure 2.5a indicates the absence of Li_2S_8 . The expected disproportionation reaction is then:



This corresponds to disproportionation reaction 2.8 in Scheme 2 given in the introduction with $x = 2$ and $m = 4$. Note that the proposed equilibrium is dominated by the forward reaction. Since Li_2S is an insoluble solid, our observation of precipitates in $x_{\text{mix}} = 2$ solutions (see Experimental section) is likely to be due to its presence.

Similarly, Figure 2.5a shows that $x_{\text{mix}} = 6$ samples are binary mixtures of Li_2S_4 and Li_2S_8 . The expected disproportionation reaction is:



This corresponds to disproportionation reaction 2.7 in Scheme 2 given in the introduction with $x = 6$ and $m = 2$. Note that the proposed equilibrium is dominated by the forward reaction.

Figure 2.5b shows the expected locations of $x_{\text{mix}} = 2, 4, 6, 8$ and Li_2S samples in the case that: (a) $x_{\text{mix}} = 4, x_{\text{mix}} = 8$, and Li_2S experimental spectra were identical to the generated principal components, and (b) the experimental spectra for $x_{\text{mix}} = 2$ and 6 represented the complete disproportionation reactions proposed above without any error. One might consider Figure 2.5b to be the ideal ternary diagram representing the parsimonious interpretation of the PCA results. The observed differences between the location of data points in Figures 2.5a and 2.5b are probably due to noise in the data or inherent uncertainties in component spectra determined by PCA. The qualitative similarity between the measured and ideal ternary diagrams is noteworthy, particularly when one considers the fact that the PCA analysis is not constrained to any particular stoichiometry.

To further explore the robustness of the conclusion regarding Li_2S_6 disproportionation to form Li_2S_4 and Li_2S_8 , we calculated a 50/50 weighted sum of the experimental spectra of $x_{\text{mix}} = 4$ and $x_{\text{mix}} = 8$ PEO samples. This calculated spectrum is compared to the experimental spectrum obtained from the $x_{\text{mix}} = 6$ PEO in Figure 2.6a. The absolute value of the difference between the experimental and calculated spectra intensity shown in Figure 2.6b is relatively small. This comparison mainly serves to show the internal consistency of our PCA-based conclusion regarding the disproportionation of Li_2S_6 (Scheme 2, reaction 2.7) to form Li_2S_4 and Li_2S_8 .

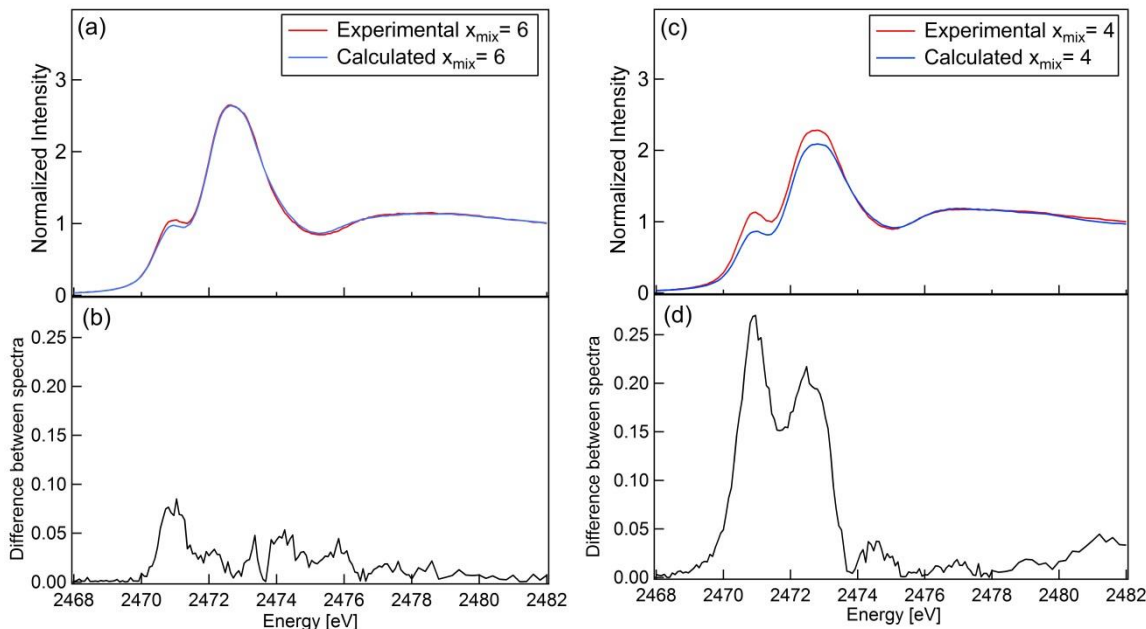


Figure 2.6 (a) XAS spectra of an $\text{Li}_2\text{S}_{x_{\text{mix}}}$ sample in PEO with $x_{\text{mix}} = 6$: Calculated using a weighted sum of spectra obtained from $x_{\text{mix}} = 4$ and $x_{\text{mix}} = 8$ samples, and one obtained directly by experiment. (b) Absolute value of the difference between experimental and calculated spectra in (a). (c) XAS spectra of an $\text{Li}_2\text{S}_{x_{\text{mix}}}$ sample with $x_{\text{mix}} = 4$: Calculated using a weighted sum of spectra obtained from $x_{\text{mix}} = 2$ and $x_{\text{mix}} = 6$ samples, and one obtained directly by experiment. (d)

Absolute value of the difference between experimental and calculated spectra in (c). The small difference in (b) supports disproportionation in $\text{Li}_2\text{S}_{x_{\text{mix}}}$ sample with $x_{\text{mix}} = 6$, while the large difference in (d) indicates that the data do not support disproportionation in $\text{Li}_2\text{S}_{x_{\text{mix}}}$ sample with $x_{\text{mix}} = 4$.

We then aimed to test whether the calculation described in the previous paragraph would hold for other spectra where we concluded that disproportionation did not take place. In other words, is it possible to represent any x_{mix} spectrum as a combinations of $(x_{\text{mix}} - 2)$ and $(x_{\text{mix}} + 2)$ spectra? Such a calculation was performed for the $x_{\text{mix}} = 4$ sample to determine if the $x_{\text{mix}} = 4$ spectrum could be represented by equal parts $x_{\text{mix}} = 2$ and $x_{\text{mix}} = 6$, corresponding to a hypothetical disproportionation reaction: $2 \text{Li}_2\text{S}_4 \rightarrow \text{Li}_2\text{S}_6 + \text{Li}_2\text{S}_2$ (according to Scheme 2, reaction 2.7). The results of this calculation are shown in Figures 2.6c and 2.6d. The difference between the experimental and calculated spectra obtained for this hypothetical reaction shown in Figure 2.6d is significantly larger than that for Li_2S_6 disproportionation by Scheme 2, reaction 2.7 as shown in Figure 2.6b. This indicates that the hypothetical reaction ($2 \text{Li}_2\text{S}_4 \rightarrow \text{Li}_2\text{S}_6 + \text{Li}_2\text{S}_2$) proposed in this paragraph is inconsistent with our data. The results in Figure 2.6 support the conclusion that that Li_2S_6 disproportionates to form Li_2S_4 and Li_2S_8 .

The disproportionation reaction we propose here is different from those reported by Cuisiner et al. who studied sulfur cathodes with a mixture of 1,3-dioxolane, 1,2-dimethoxyethane, LiClO_4 , and LiNO_3 as the electrolyte.⁽⁶⁹⁾ They concluded that Li_2S_6 does not disproportionate, while Li_2S_8 does. The difference between our conclusions and those reported by Cuisiner et al. may be due to the differences in the systems examined. In particular, our work studies polysulfides in polymer electrolytes with no added salt while Cuisiner et al. studied polysulfides generated via redox reaction in the cathode in the presence of LiClO_4 and LiNO_3 . Additionally, the polysulfide species of this work were obtained by chemical reactions, rather than electrochemical reactions.

While the above analysis has focused on the parsimonious interpretation of the XAS data based on PCA, it is not unique. For example, if a constant fraction of a fourth species were present in all samples, PCA would still indicate three principal components, but the component spectra thus generated would not represent single molecular species. Note that this is highly unlikely as reactions involving polysulfides must be consistent with strict stoichiometric constraints (e.g. Scheme 2). Nevertheless, further work is needed to critically evaluate the validity of the proposed disproportionation schemes.

2.4 Conclusions

Solid-state polymer films of PEO and SEO containing Li_2S_x molecules as well as Li_2S powder were examined using XAS at the sulfur K-edge. Principal component analysis was performed on the system of collected X-ray spectra to obtain spectral fingerprints of individual polysulfide species. The present approach to spectral data interpretation makes no assumption regarding polysulfide disproportionation. We believe the coupling of XAS with PCA will stand as an effective tool for spectroelectrochemical studies of Li-S battery reaction mechanisms.

Our analysis revealed that spectra obtained at all x_{mix} values (2, 4, 6, 8) could be represented as mixtures of one or two principal components. The PCA results were quantified on a ternary diagram (Figure 2.5a). The data for Li_2S and $x_{\text{mix}} = 4$ and 8 samples were located close to the corners of the ternary diagram. Our parsimonious interpretation is that the $x_{\text{mix}} = 4$ and 8 samples were composed of nearly pure molecular species, Li_2S_4 and Li_2S_8 , respectively. In contrast samples of $x_{\text{mix}} = 2$ and 6 were located on the binary mixture lines. The fact that the

most complex polysulfide containing mixtures in PEO-based electrolytes have only two components is a remarkable simplification. The location of $x_{\text{mix}} = 2$ samples suggests that Li_2S_2 disproportionates to form the Li_2S_4 and Li_2S , while the location of $x_{\text{mix}} = 6$ data suggests that Li_2S_6 disproportionates to form Li_2S_4 , and Li_2S_8 . The implication of these results is that complex reaction pathways similar to the proposed example shown in Scheme 1 would be highly simplified. Essentially, steps (2.2) and (2.4) would be skipped over, as Li_2S_6 and Li_2S_2 disproportionate spontaneously to give Li_2S_8 and Li_2S_4 , and Li_2S and Li_2S_4 , respectively. Further work is needed to determine the kinetics of disproportionation. If this simplification is also valid in polysulfides created by electrochemical driving forces in the lithium-sulfur battery, then resolving issues related to capacity fading may be addressed by focusing on the containment of only two species: Li_2S_4 and Li_2S_8 .

Note that no knowledge of the relationship between observed peaks in the XAS spectra and specific electronic transitions of particular species was used to determine polysulfide disproportionation. In future work we will use molecular simulations and other complimentary experimental tools to critically examine the conclusions made in this study. In particular, we plan to study the products of electrochemical reduction of sulfur in appropriately designed in situ XAS cells. The species that are created in electrochemical cells may be different from those detected in the present work that is limited to chemically synthesized polysulfides.

2.5 Acknowledgements

We acknowledge the help of Erik Nelson and Matthew Latimer of SSRL beamline 4-3, and Wayne Stolte of the Advanced Light Source (ALS) beamline 9.3.1, where preliminary work was performed. Preliminary work was also performed at ALS beamline 10.3.2. J. Velasco-Velez gratefully acknowledges financial support from the Alexander von Humboldt foundation. The authors acknowledge Rachel Segalman for use of ellipsometry equipment, and Mukes Kapilishrami for valuable advice regarding the XAS experiments.

This work was supported by the Assistant Secretary for Energy Efficiency and Renewable Energy, Office of Vehicle Technologies of the U.S. Department of Energy under Contract DE-AC02-05CH11231 under the Batteries for Advanced Transportation Technologies (BATT) Program.

Portions of this research were carried out at the Stanford Synchrotron Radiation Lightsource, a Directorate of SLAC National Accelerator Laboratory and an Office of Science User Facility operated for the U.S. Department of Energy Office of Science by Stanford University. The SSRL Structural Molecular Biology Program is supported by the DOE Office of Biological and Environmental Research, and by the National Institutes of Health, National Institute of General Medical Sciences (including P41GM103393). The contents of this publication are solely the responsibility of the authors and do not necessarily represent the official views of NIGMS or NIH. Complimentary XAS experiments were performed at the Advanced Light Source. The Advanced Light Source is supported by the Director, Office of Science, Office of Basic Energy Sciences, of the U.S. Department of Energy under Contract No. DE-AC02-05CH11231.

2.6 Supporting information

2.6.1 Effect of air exposure on X-ray absorption spectra

To elucidate the effect that air-exposure had on obtained X-ray spectra, XAS was performed on an unexposed sample of $x_{\text{mix}} = 8$ dissolved in SEO. After this initial measurement, the sample was removed from the measurement chamber and allowed to sit in air at room temperature for one hour before another XAS measurement was performed. The resulting spectra can be seen in Figure 2.S1 below. The peaks that occur at 2479.4 and 2480.8 eV are common in oxidized sulfur species,⁽⁵³⁾ and are direct evidence of the effect that air exposure may have on obtained X-ray spectra. The increase in intensity of these two peaks is also accompanied by a decrease in pre-edge peak intensity, possibly due to the reaction of anionic sulfur species with oxygen or water.

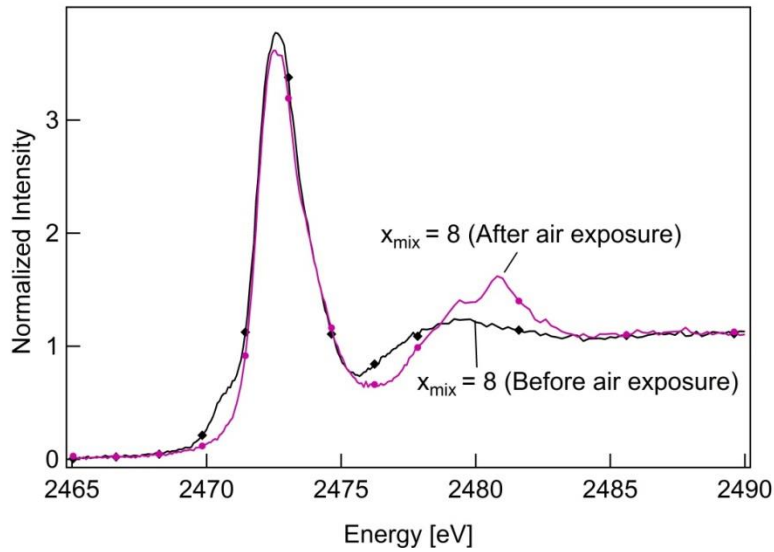


Figure 2.S1 X-ray spectra of $x_{\text{mix}} = 8$ in SEO samples before and after air exposure

2.6.2 Equations for the calculation of x_{mix} error

1. Calculation of x_{mix} (Equation 2.S1)

$$x_{\text{mix}} = \frac{\left(\frac{\text{moles } S / \text{mole } S_8 \cdot \text{mass of } S_8}{\text{molar mass } S_8} \right) + \left(\frac{\text{moles } S / \text{mole } Li_2S \cdot \text{mass of } Li_2S}{\text{molar mass } Li_2S} \right)}{\left(\frac{\text{moles } Li_2 / \text{mole } Li_2S \cdot \text{mass of } Li_2S}{\text{molar mass } Li_2S} \right)}$$

2. Overall calculation of x_{mix} error (Equation 2.S2)

$$\Delta x_{\text{mix}} = \frac{\partial x_{\text{mix}}}{\partial \text{mass } S_8} \cdot \Delta \text{mass of } S_8 + \frac{\partial x_{\text{mix}}}{\partial \text{mass } Li_2S} \cdot \Delta \text{mass of } Li_2S$$

3. Calculation of error with respect to mass of S_8 (Equation 2.S3)

$$\frac{\partial x_{mix}}{\partial \text{mass } S_8} = \frac{\left(\frac{\text{moles } S / \text{mole } S_8}{\text{molar mass } S_8} \right)}{\left(\frac{\text{moles } Li_2 / \text{mole } Li_2S \cdot \text{mass } Li_2S}{\text{molar mass } Li_2S} \right)}$$

4. Calculation of error with respect to mass of Li_2S (Equation 2.S4)

$$\frac{\partial x_{mix}}{\partial \text{mass } Li_2S} = \frac{\left(- \frac{\text{moles } S / \text{mole } S_8 \cdot \text{mass } S_8}{\text{molar mass } S_8} \right)}{\left(\frac{\text{moles } Li_2 / \text{mole } Li_2S \cdot (\text{mass } Li_2S)^2}{\text{molar mass } Li_2S} \right)}$$

2.6.3 Sample calculations for x_{mix} error

Table 2.S1 Data for sample: $x_{mix} = 2$, PEO, used for sample calculations of x_{mix} error

Mass of Li_2S added	0.0177	g
Mass of S_8 added	0.0122	g
Moles S per mole S_8	8	
Moles Li_2 per mole Li_2S	1	
Molar mass S_8	256.0	g/mol
Molar mass Li_2S	45.8	g/mol
Δ mass of S_8	± 0.0001	g
Δ mass of Li_2S	± 0.0001	g

1. Calculation of x_{mix}

$$x_{mix} = \frac{\left(\frac{8 \cdot 0.0122g}{256g/mol} \right) + \left(\frac{1 \cdot 0.0177g}{45.8g/mol} \right)}{\left(\frac{1 \cdot 0.0177g}{45.8g/mol} \right)} = 1.987$$

2. Calculation of error with respect to mass of S_8

$$\frac{\partial x_{mix}}{\partial \text{mass } S_8} = \frac{\left(\frac{8}{256g/mol} \right)}{\left(\frac{1 \cdot 0.0177g}{45.8g/mol} \right)} = 80.8g^{-1}$$

3. Calculation of error with respect to mass of Li_2S

$$\frac{\partial x_{mix}}{\partial \text{mass } \text{Li}_2\text{S}} = \frac{\left(-\frac{8 \cdot 0.0122\text{g}}{256\text{g/mol}}\right)}{\left(\frac{1 \cdot (0.0177\text{g})^2}{45.8\text{g/mol}}\right)} = -55.7\text{g}^{-1}$$

4. Overall calculation of x_{mix} error

$$\Delta x_{mix} = 80.8\text{g}^{-1} \cdot 0.0001\text{g} + -55.7\text{g}^{-1} \cdot 0.0001\text{g} = \pm 0.0025$$

2.6.4 Equations for the calculation of sulfur concentration error

1. Calculation of sulfur concentration (Equation 2.S5)

$$\text{Sulfur concentration} \left(\frac{\text{g S}}{\text{g polymer}}\right) = \frac{(\text{mass } \text{Li}_2\text{S})(\text{wt}\% \text{ S in } \text{Li}_2\text{S}) + \text{mass } \text{S}_8}{\text{mass polymer}}$$

2. Overall calculation of sulfur concentration error (Equation 2.S6)

$$\Delta \text{ sulfur conc.} = \frac{\partial \text{ sulfur conc.}}{\partial \text{ mass } \text{S}_8} \cdot \Delta \text{ mass of } \text{S}_8 + \frac{\partial \text{ sulfur conc.}}{\partial \text{ mass } \text{Li}_2\text{S}} \cdot \Delta \text{ mass of } \text{Li}_2\text{S} + \frac{\partial \text{ sulfur conc.}}{\partial \text{ mass polymer}} \cdot \Delta \text{ mass polymer}$$

3. Calculation of error with respect to mass of S_8 (Equation 2.S7)

$$\frac{\partial \text{ sulfur conc.}}{\partial \text{ mass } \text{S}_8} = \frac{1}{\text{mass polymer}}$$

4. Calculation of error with respect to mass of Li_2S (Equation 2.S8)

$$\frac{\partial \text{ sulfur conc.}}{\partial \text{ mass } \text{Li}_2\text{S}} = \frac{(\text{wt}\% \text{ S in } \text{Li}_2\text{S})}{\text{mass polymer}}$$

5. Calculation of error with respect to mass of polymer (Equation 2.S9)

$$\frac{\partial \text{ sulfur conc.}}{\partial \text{ mass polymer}} = -\frac{(\text{mass } \text{Li}_2\text{S})(\text{wt}\% \text{ S in } \text{Li}_2\text{S}) + \text{mass } \text{S}_8}{(\text{mass polymer})^2}$$

2.6.5 Sample calculations for sulfur concentration error

Table 2.S2 Data for sample: $x_{mix} = 2$, PEO, used for sample calculations

Mass of Li ₂ S added	0.0177	g
Mass of S ₈ added	0.0122	g
Mass of polymer added	0.0543	g
wt% S in Li ₂ S	0.699	-
Δ mass of S ₈	±0.0001	g
Δ mass of Li ₂ S	±0.0001	g
Δ mass of polymer	±0.0001	g

1. Calculation of sulfur concentration

$$\text{Sulfur concentration} \left(\frac{g S}{g \text{ polymer}} \right) = \frac{(0.0177g)(0.699) + 0.0122g}{0.0543g} = 0.452 \frac{g S}{g \text{ polymer}}$$

2. Calculation of error with respect to mass of S₈

$$\frac{\partial \text{sulfur conc.}}{\partial \text{mass } S_8} = \frac{1}{0.0543g} = 18.4g^{-1}$$

3. Calculation of error with respect to mass of Li₂S

$$\frac{\partial \text{sulfur conc.}}{\partial \text{mass } Li_2S} = \frac{0.699}{0.0543g} = 12.8g^{-1}$$

4. Calculation of error with respect to mass of polymer

$$\frac{\partial \text{sulfur conc.}}{\partial \text{mass polymer}} = - \frac{(0.0177g)(.699) + 0.0122g}{(0.0543g)^2} = -8.3g^{-1}$$

5. Calculation of sulfur concentration error

$$\begin{aligned} \Delta \text{ sulfur conc.} &= 18.4g^{-1} \cdot 0.0001g + 12.8g^{-1} \cdot 0.0001g - 8.3g^{-1} \cdot 0.0001g \\ &= \pm 0.0022 \frac{g S}{g \text{ polymer}} \end{aligned}$$

Chapter 3 – Characterization of Polysulfide Radicals Present in an Ether-based Electrolyte of a Lithium-Sulfur Battery during Initial Discharge using *in situ* X-ray Absorption Spectroscopy Experiments and First-Principles Calculations[†]

ABSTRACT

The presence and role of polysulfide radicals in the electrochemical processes of lithium sulfur (Li-S) batteries is currently being debated. Here, we leverage first principles interpretations of measured X-ray absorption spectra (XAS) of Li-S cells with an ether-based electrolyte. We find unambiguous evidence for significant quantities of polysulfide radical species (LiS_3 , LiS_4 , and LiS_5), including the trisulfur radical anion $\text{S}_3^{\cdot-}$, present after initial discharge to the first discharge plateau, as evidenced by a low energy shoulder in the S K-edge XAS below 2469 eV. This feature is not present in the XAS of cells at increased depth of discharge, which, by our analysis, exhibit increasing concentrations of progressively shorter polysulfide dianions. Through a combination of first principles molecular dynamics and associated interpretation of in-situ XAS of Li-S cells, we provide atomic level insights into the chemistries that underlie the operation and stability of these batteries.

3.1 Introduction

Despite many years of research, the electrochemical reactions underlying the operation of lithium-sulfur (Li-S) batteries are still the subject of some debate. In particular, the radical trisulfur anion, $\text{S}_3^{\cdot-}$, has concurrently been purported as a key species in the electrochemical process^(18, 68, 83) or has been discounted as existing in any appreciable concentration during battery operation^(30, 84, 85). While one may expect the trisulfur radical to be extremely reactive, there is some reason to believe that it might be stable in solvents commonly used in Li-S batteries. Colorimetric analysis, UV-visible (UV-vis) and electron paramagnetic spin resonance (ESR/EPR) spectroscopies have shown that radical anions are stabilized in chemical solutions of polar solvents such as dimethylformamide (DMF)^(33, 40, 86) and dimethyl sulfoxide (DMSO)^(26, 39, 65, 87), but not tetrahydrofuran (THF)^(38, 86). Based on these and similar studies,^(88, 89) it is generally accepted that highly polar, electron pair donor solvents such as DMSO and DMF are capable of stabilizing radicals in solutions, while low dielectric constant solvents like THF cannot⁽⁹⁰⁻⁹²⁾. Within the context of Li-S batteries, Barchasz *et al.* obtained UV-vis and ESR evidence of radical species in a Li-S cell that consisted of poly(ethylene oxide) oligomers with four repeat units (also known as tetraethylene glycol dimethyl ether or TEGDME) mixed with 1M LiTFSI.⁽⁸³⁾ Hagen and coworkers used *in-situ* Raman measurements and theoretical vibrational calculations to show that radical polysulfides are present during cell discharge.⁽⁴⁴⁾ More recently Wang *et al.* performed *in-situ* ESR on a Li-S cell consisting of a 1,3-dioxolane (DOL), dimethyl ether (DME) (1M LiTFSI) electrolyte and also detected radicals.⁽⁴²⁾ In the same study, they also detected the presence of radicals in chemical mixtures of lithium

[†]This work was reported in *Adv. Ener. Mat.* **5** 1500285 (2015)

polysulfides in DOL:DME by ESR.

Several questions concerning the presence of radicals during battery operation remain unresolved. This discussion has predominantly focused on the trisulfur radical. While S_3^- could be formed via a direct electrochemical pathway, the prevailing assumption is that it is formed via the dissociation of Li_2S_6 ($Li_2S_6 \rightarrow 2 LiS_3$).^(39, 40, 42, 65, 87) If true, then the redox pathway and voltage profile must significantly depend on the equilibrium constant of the disproportionation reaction, as well as its kinetics. It is also still unclear how critical the formation of polysulfide radical anions is to the remaining redox pathways⁽⁹³⁾. It is not known if the radicals are an essential intermediate for complete reduction of sulfur (or complete oxidation of Li_2S). In addition, the concentration of radical anions relative to dilithium sulfide species formed during redox reactions has not been quantified. Questions also emerge regarding the parasitic reactions that take place at the lithium metal anode, and damaging reactions that may take place between radical species and cell electrolytes. The extent to which these effects depend on the choice of solvent/salt electrolyte mixture is also unclear.

As a means of gaining insights into the complex chemistries that underlie Li-S battery systems, X-ray absorption spectroscopy (XAS) has been utilized in several studies.^(18, 30, 55, 68, 69, 85, 93-95) The attractiveness of XAS is that it is element-specific while also being sensitive to the local bonding chemistry and solvent environment. When properly interpreted, XAS can provide powerful insights into molecular structure and electronic charge state, and, for *in situ* studies, changes in chemistry due to an external bias. Characterization of the lithium polysulfide species in Li-S batteries usually involves XAS at the sulfur K-edge, i.e. excitations of S 1s core electrons into unoccupied molecular orbitals with local *p*-character. Recently, Gao *et al.* investigated the effect of liquid electrolytes on battery performance using S K-edge XAS, and found qualitative differences between polar and ethereal solvents during cycling.⁽⁶⁸⁾ Cuisinier *et al.* probed the chemistry of an operational cell by fingerprinting their measured XAS with solid standards.⁽⁶⁹⁾ This study clearly demonstrated the production of polysulfide species and lithium sulfide during discharge (due to the consumption of sulfur), although no radicals were invoked in the proposed cathode reaction mechanism. Consistent with these findings, Patel *et al.* used S K-edge XAS in conjunction with NMR to probe the chemical species formed at the cathode and in the electrolyte during different stages of discharge of the battery, finding that shorter polysulfides were continually being formed at later stages of the discharge.⁽⁸⁵⁾ On the other hand, Lowe *et al.* attempted to uncover the chemistries induced during the discharge process of a Li-S cell with an ether-based solvent (TEGDME) using S K-edge XAS, and interpreted their data as providing evidence of the trisulfur radical.⁽¹⁸⁾

The differences in interpretation of the experimental S K-edge XAS data can be directly traced to reliance on experimentally derived spectral standards coupled with the lack of such standards for polysulfide solutions: due to possible spontaneous polysulfide disproportionation and the establishment of equilibrium mixtures in solution, isolating standards for specific molecular species is necessarily complicated, if not impossible.^(25, 30) As a result, fingerprinting is frequently performed using solid analogs, which may induce errors in the analysis since the correspondence between the solid and solution phase XAS is by no means guaranteed.⁽⁹⁶⁾ This could be an even larger issue for radical anions in solution, since the stabilization and subsequent isolation of the radical is purported to be solvent-dependent, then so might the solution-phase XAS spectral standard. Nevertheless, the solid-state spectral standard of the trisulfur radical anion, measured using crystalline ultramarine samples,⁽⁹⁷⁾ has recently been used by Cuisinier *et al.* to dynamically fingerprint a working Li-S cell.⁽⁹³⁾ The authors showed that cells containing

dimethylacetamide (DMA) (1M LiClO₄) show evidence of LiS₃, while, cells containing DOL:DME (1M LiClO₄) do not,⁽⁹³⁾ which stands in contrast to the ESR findings of Wang and coworkers.⁽⁴²⁾ It is worth noting that the presence of ESR signals is, perhaps, the most direct signature of the presence of radicals.

A recent advance towards establishing standards, and thus atomistic interpretations of experimental measurements, has been the use of electronic structure methods based on density functional theory (DFT).^(55, 95, 98) Vijayakumar *et al.* calculated the XAS of the various polysulfides, including the trisulfur radical, in vacuum and in a solvation shell of six DMSO molecules using time-dependent DFT calculations, and used these spectra to fingerprint experimental measurements.⁽⁹⁵⁾ In a previous work we demonstrated that the XAS of dissolved lithium polysulfide dianion species can be obtained via condensed-phase first-principles molecular dynamics and DFT spectral simulations.⁽⁵⁵⁾ More recently, we extended our approach to the various polysulfide radicals in vacuum⁽⁹⁸⁾, and have predicted that XAS can detect the trisulfur radical against a background of longer chain polysulfide dianions at a ~20% molar concentration (or ~ 4% by spectral composition), at 0.1 – 0.2 eV spectral resolution. Our condensed phase DFT approach has been proven accurate when compared to measured spectra of known sulfur containing compounds and is extremely insightful for interpreting spectra based on the atomic and electronic properties of the molecule of interest.

In this work, we present, for the first time within the Li-S context, measured X-ray spectra of chemically equilibrated cells at various depths of discharge. Most importantly, we leverage first-principles spectral simulations to deduce the particular sulfur speciation consistent with the measured spectra. We do this using superpositions of our calculated spectra for: the crystalline solid endpoints (S₈ and Li₂S); the intermediate polysulfide dianions (Li₂S_x, where the polysulfide dianion is S_x²⁻) dissolved in oligomeric PEO; and dissolved radical polysulfide anions (LiS₃, LiS₄, LiS₅), which are the only predicted contributors to low energy absorption features in our S K-edge XAS. Whereas previous studies probed the sulfur cathode in an attempt to directly examine the charge and discharge reaction processes, this present study explores a different question, also pertinent to Li-S cells: if cell discharge were stopped at specific points in the discharge process, what intermediate species would be present in the battery electrolyte after ample time has been given for polysulfide dissolution to occur? This question is of some importance, as real-world consumer batteries will be stopped and started as the user chooses; it would be useful to know what species can be expected in the battery electrolyte if dissolution were to occur. Our results provide further insight into the discharge and disproportionation reactions that take place in the electrolyte during cycling.

3.2. Materials and Methods

3.2.1. Experimental Section

3.2.1.1. Electrolyte Preparation

All electrolyte, cathode, and cell preparation was performed in an argon-filled glovebox (MBraun). Electrolyte films were prepared using a diblock copolymer of polystyrene-poly(ethylene oxide) (SEO) synthesized on a high vacuum line via sequential anionic polymerization, having polystyrene and poly(ethylene oxide) molecular weights of 240 kg/mol and 269 kg/mol, respectively, and a polydispersity index (PDI) of 1.26.^(74, 99) SEO and dry, battery grade lithium perchlorate (LiClO₄) (Sigma-Aldrich) were added to n-methylpyrrolidone

(NMP) (EMD Millipore) in an amount equivalent to 10 wt% solids, and allowed to mix overnight at 90°C. The solution was then cast onto nickel foil using a doctor blade and allowed to dry at 60°C overnight. The resulting film was peeled from the nickel foil and dried under vacuum at 90°C overnight. The dry film composition had a LiClO₄ amount equivalent to an 'r' value of $r = 0.085$, where 'r' is the ratio of lithium ions per ethylene oxide monomer.

3.2.1.2. Cathode Preparation

Cathode slurries contained S₈ (Alfa Aesar), carbon black (Denka), LiClO₄, and SEO (identical to that which was used in the electrolyte separator) mixed in NMP, such that the slurry was 15 wt% solids. The slurry was mixed overnight at 90°C and subsequently mixed using a homogenizer (Polytron) set to 15,000 RPM. Homogenization was performed three times, five minutes each time with five minute breaks in between each homogenization to prevent the solution from heating up past undesirable temperatures. The resulting slurry was immediately cast onto electronic grade aluminum foil using a doctor blade and allowed to dry overnight at 50°C in an argon filled glovebox. The cathode electrode was then dried under vacuum overnight at 50°C. The dry composition of all cathodes used in the study was 13.0 wt% S₈, 51.4% SEO, 5.5% LiClO₄ and 30.1% carbon.

3.2.1.3. Cell Assembly

Modified pouch cells were prepared by punching a single 3/16'' hole in the center of one side of aluminum laminate pouch material (Showa Denko). A ring of epoxy was carefully coated around this hole, on the outer side of the pouch, and a 5/8'' hole of ultra-thin 3μm thick Mylar film (2spi) was then placed on top of the epoxy. This was then allowed to dry overnight at room temperature and subsequently dried overnight under vacuum at 90°C. Pouches were then brought directly into the glovebox without exposure to air.

Circular pieces of cathode and electrolyte were punched from the dried films. Cathode discs were punched to be 7/16'' in diameter, and electrolyte films, 9/16''. After punching, thickness of cathode and electrolyte discs were measured using a micrometer; mass of cathode discs was measured using a balance (Mettler Toledo). Lithium metal chips (MTI), were used as the anode material and were further punched to be 7/16'' in diameter. Cathode electrodes were gently pressed to punched electrolyte, placed inside a fluorinated ethylene propylene (FEP) bag and pressed for 30 seconds using a hand press at room temperature. Lithium metal discs were then pressed to the opposing side of the electrolyte to form a sandwich. The sandwich was then placed in the pouch cell, a nickel tab taped to the lithium metal and an electronic grade aluminum tab taped to the back of the cathode electrode, using Kapton tape in both cases. Assembled cell pouches were sealed with a vacuum heat sealer (Audionvac). Cells were then annealed overnight at 90°C to enhance interfacial contact between electrodes and the electrolyte film.

3.2.1.4. Battery Cycling

Batteries were placed in a temperature controlled box set to 90°C and allowed to sit for 12 hours before cycling. Cycling was performed using a VMP3 Potentiostat (Bio-Logic). All cells were cycled at a discharge rate corresponding to C/40, calculated using the measured mass of the cathode electrode, the predetermined cathode composition, and assuming a theoretical

capacity of 1672 mA-h/g for sulfur. Discharge was stopped at three different voltages: 2.25V, 2.02V, and the minimum cutoff of 1.50V. After discharge was stopped, cells were disconnected from potentiostat leads and left to sit at 90°C for three days to allow diffusion of polysulfide species out of the electrolyte.

3.2.1.5. Experimental X-ray Absorption Spectroscopy Measurements

XAS measurements were performed at beamline 9.3.1 of the Advanced Light Source (Lawrence Berkeley National Laboratory). Pouch cells were transferred from the glovebox to the beamline endstation chamber, which was kept at ultra-high vacuum ($< 6e-7$ torr) and at room temperature. Measurements were taken in fluorescence mode using a Hamamatsu silicon photodiode, with 0.1 eV energy resolution around the absorption K-edge. The beam spot size was roughly 5 mm². Calibration was performed using sodium thiosulfate (Sigma-Aldrich), setting the first peak maximum to 2472.02 eV. As shown in Figure 3.1b, incident X-ray photons passed through the anode side of the battery and into the electrolyte. Data was normalized and background subtracted by hand.

3.2.2. Theoretical Calculations

3.2.2.1. Ab-Initio Molecular Dynamics (AIMD) Simulations

Optimization of the lithium polysulfide species in the gas phase was performed using density functional theory (DFT) calculations employing the Perdew-Burke-Ernzerhof⁽¹⁰⁰⁾ (PBE) generalized-gradient approximation to the exchange-correlation potential. We performed conjugate-gradient minimization of the total energy with respect to the atomic positions using the PWSCF code within the Quantum-ESPRESSO package.⁽¹⁰¹⁾ The plane-wave pseudopotential calculations used ultrasoft pseudopotentials and a kinetic energy cut-off for electronic wave functions (density) of 25 (200) Ry.

The gas-phase optimized structures were then inserted into the center of a pre-equilibrated box of 24 solvent molecules. By analogy to the poly(ethylene oxide) component of the electrolyte in our samples, we make use of an oligomeric approximation to PEO called tetraethylene glycol dimethyl ether (TEGDME) or tetraglyme. Our AIMD simulations were performed using a modified version of the mixed Gaussian and plane wave code CP2K/Quickstep.^(102, 103) We employed a triple- ζ basis set with two additional sets of polarization functions (TZV2P)⁽¹⁰⁴⁾ and a 320 Ry plane-wave cutoff. The same PBE functional is employed⁽¹⁰⁰⁾, and the Brillouin zone is sampled at the Γ -point only. Interactions between the valence electrons and the ionic cores are described by norm-conserving pseudopotentials^(105, 106). Solutions to the Poisson equation are provided by an efficient Wavelet-based solver⁽¹⁰⁷⁾. We overcome the poor description of the long-range dispersive forces within the PBE-GGA exchange-correlation functional by employing the DFTD3 empirical corrections of Grimme *et al.*⁽¹⁰⁸⁾ For each system, we performed at least 50 ps of constant volume constant temperature (NVT) dynamics, saving a snapshot of the system (atomic coordinates and velocities) at every step. The temperature of the system was kept near 300K using a Nose-Hoover thermostat (temperature damping constant of 100 fs). We allowed for 20 ps of equilibration and 100 snapshots for the system from 20 – 50ps (evenly spaced every 30fs) as input to our first principles X-ray absorption calculations.

3.2.2.2. First Principles X-ray Absorption Spectroscopy Calculations

X-ray absorption spectra were calculated within a spin-polarized generalization of the excited electron and Core Hole Density Functional Theory (XCH-DFT) approach.⁽⁹⁶⁾ All our XCH calculations employed the same periodic boundary conditions as our AIMD simulations, and used the PBE-GGA functional⁽¹⁰⁰⁾ and plane-wave ultrasoft pseudopotentials with a kinetic energy cut-off for the electronic wave functions (density) of 25 (200) Ry. Core-excited ultrasoft pseudopotentials and corresponding atomic orbitals were generated with the Vanderbilt code⁽¹⁰⁹⁾. Matrix elements representing transition amplitude of core-excitations were evaluated within the projector-augmented-wave (PAW) frozen-core approximation.⁽¹¹⁰⁾ The PWSCF code within the Quantum-ESPRESSO package⁽¹⁰¹⁾ was used to generate the core-excited Kohn-Sham eigenspectrum, while the Shirley interpolation scheme⁽¹¹¹⁾ was used to accelerate numerical convergence of the computed spectra. We include a 0.2 eV Gaussian convolution to guarantee a continuous spectral contribution from each atom. The calculated XAS is taken as the statistical average of the computed spectrum of every sulfur atom in the structure, which further includes intrinsic line shape broadening resulting from finite temperature effects at 298K.

3.2.2.3. Least Squares Fitting (LSF)

Fitting of the experimental spectra employed the method of least squares using an in-house code. The calculated first principles XAS of seven dianions [Li_2S_x ; $x = 2$ to 8], five radical anions [LiS_x ; $x = 2$ to 6], S_8 and Li_2S were used to construct a hypothetical spectrum that minimized the error in peak positions and intensities when compared to the measured spectrum. Due to concerns of overabsorption and beam damage, the LSF was performed for the energy range spanning from 2465 eV to 2474.5 eV.

3.3 Results and Discussion

3.3.1. Experimental XAS of the Li-S cell at various depths of discharge

We begin our analysis by presenting the schematic for the XAS experiments performed (Figure 3.1a) and an example image of the modified pouch cell (Figure 3.1b). Li-S cells used in this study comprised cathodes containing elemental sulfur, carbon black, lithium perchlorate (LiClO_4) and a diblock copolymer electrolyte polystyrene-poly(ethylene oxide) (SEO). The electrolyte separator consisted of SEO and LiClO_4 ($r = 0.085$). The anodes were lithium metal foils. Further details are given in the experimental section.

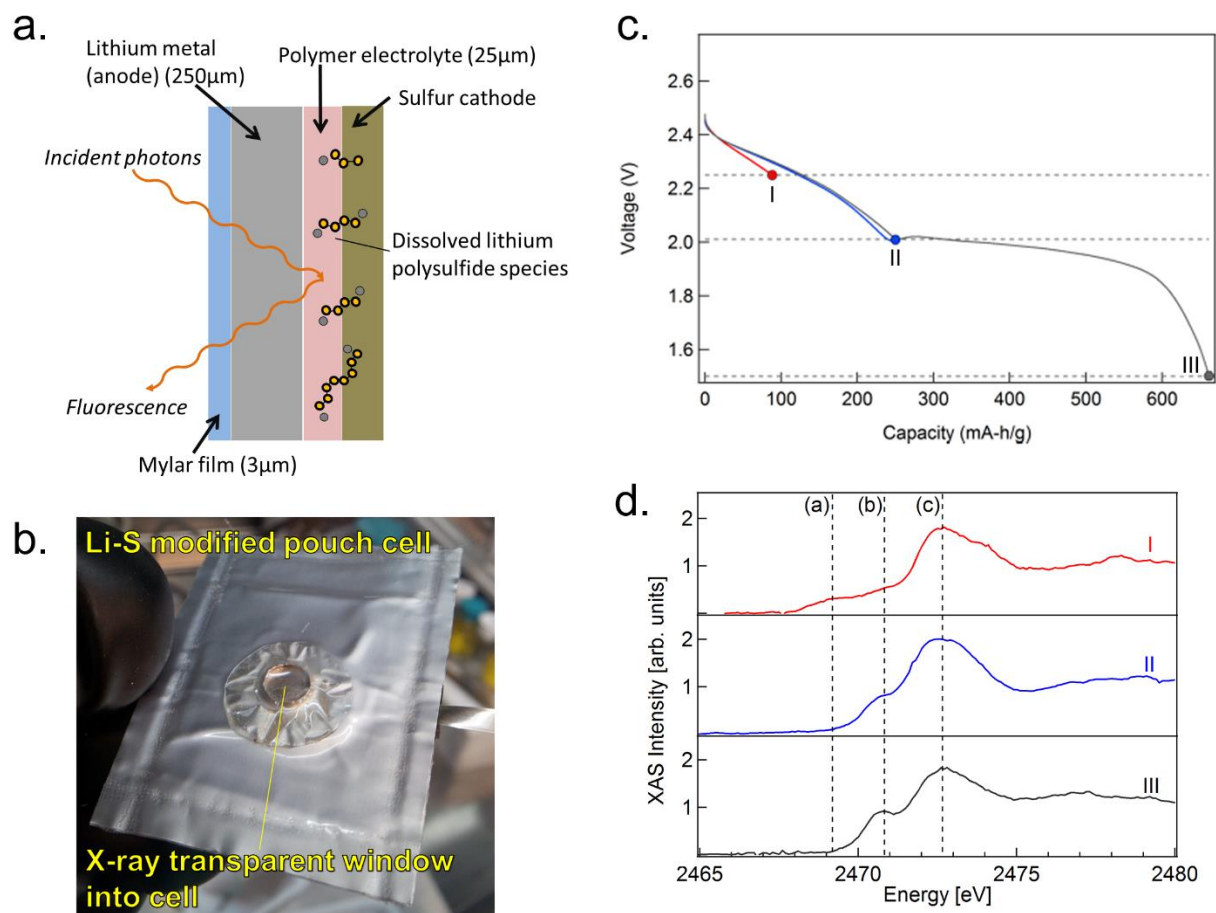


Figure 3.1 Description of experimental setup and results. **a)** Schematic of X-ray experiment **b)** Diagram of modified Li-S pouch cell **c)** I-V curves for the three pouch cells tested. The cells were stopped at three different points: I, II and III, corresponding to 2.25V, 2.02V, and 1.5V, respectively. X-ray absorption near-edge structure (XANES) measurements are obtained after holding the cell voltage at the indicated value (dashed horizontal lines) for three days. **d)** Sulfur K-edge XANES as a function of discharge, for each of the three points indicated in (c). Dashed vertical lines are included as a guide to highlight several low energy features below the white line near 2472.6 eV.

We elect to probe through the lithium metal anode side of the battery and into the electrolyte (Figure 3.1a), in order to maximize the XAS signal of the electrolyte over the cathode. Fresh cells were discharged at constant current of 41.8 mA/g (a C/40 discharge rate) at 90°C using a VMP-3 potentiostat to three specific voltages: 2.25, 2.02 and 1.5 V, labeled I, II, and III, respectively. The cell potential versus discharge capacity for the three cells is shown in Figure 3.1c. After discharging was stopped, cells were then allowed to rest for three days at the operating temperature (90°C), before being probed via XAS at the sulfur K-edge. This procedure means that our measurements are most likely of the equilibrium distributions of polysulfides in the electrolyte. The discharge curves in Figure 3.1c are qualitatively similar to those reported in the literature.^(12, 112) The first-discharge capacity of the fully-discharged cell (661 mA-h/g) is less than half of the theoretical capacity of sulfur (1672 mA-h/g). Our objective was not to design a cell to exploit the full capacity of the sulfur cathode, but rather to enable the XAS experiments.

Our measured XAS spectra (Figure 3.1d) show unique profiles that may point to fundamentally different chemistries. All three spectra have a main feature centered near 2472.6 eV, labeled ‘c’, reminiscent of the sulfur “white-line.” Below the main feature is a lower intensity “pre-edge” between 2470.5 - 2471 eV, labeled ‘b’. While this pre-edge feature has been purported as being evidence of the trisulfur radical anion,⁽¹⁸⁾ our previous study revealed the origin to be excitations specific to the terminal S atoms, i.e., those at the end of the polysulfide dianion chains.⁽⁵⁵⁾ The intensity and distinctiveness of this feature is found to increase as the cell is discharged. This indicates an increase in the populations of shorter chain polysulfide dianions (i.e. Li_2S_2 , Li_2S_3 , and Li_2S_4), as suggested by our previous work⁽⁵⁵⁾ and the conclusions of voltage dependent studies⁽⁸³⁾.

Of particular interest, we find that spectrum I, corresponding to a 2.25 V cutoff voltage, exhibits a low energy shoulder in the range 2468-2470 eV, labeled ‘a’, that is below the pre-edge peak ‘b’ at 2470.5 - 2471 eV. This low energy shoulder is absent in spectra II and III. We note that this feature appears below the pre-edge, suggesting excitations to molecular orbitals of lower energy than the 3p σ^* levels. Some clues to its origin can be found from S K-edge XAS measurements of ultramarine samples. Indeed Fleet and coworkers proposed that the low energy feature near 2468.0 eV from ultramarine powder was due to transitions from the 1s $\rightarrow \pi^*$ (3p) molecular orbital of a radical anion, purported to be trisulfur, trapped in an aluminosilicate cage.⁽⁹⁷⁾ Motivated by this study, we calculated the sulfur K-edge XAS spectrum of a lithium trisulfur radical complex (LiS_3) dissolved in TEGDME, an oligomer of PEO comprising four glyme units. The correspondence between the calculated XAS of isolated polysulfide radicals in oligomeric PEO and SEO is inferred from the similar chemical nature and dielectric screening environment of these solvents. These XAS spectra are then used as a basis to fingerprint the XAS of the experimental samples, which undoubtedly contain mixtures of the various species.

3.3.2. Theoretical XAS of dissolved lithium polysulfides

3.3.2.1. Trisulfur radical

As noted previously, XAS is an atom specific probe and our computational approach similarly involves combining separate calculations where a S 1s core electron is excited from a single atom. The power of our computational approach is that it facilitates the deconvolution of a spectrum in terms of transitions to specific molecular orbitals, and from particular atoms in a molecule. In the particular case of trisulfur, the first available XAS orbital is the singly occupied π^* molecular orbital.⁽⁹⁸⁾ In the ground state, this orbital extends over the entire molecule. However, upon absorption of an X-ray photon, the particular core-excited S atom perturbs this orbital, and in different ways depending on its location within the trisulfur chain. We see this by separately considering excitations originating from either the internal (central) sulfur atom or the two terminal atoms.

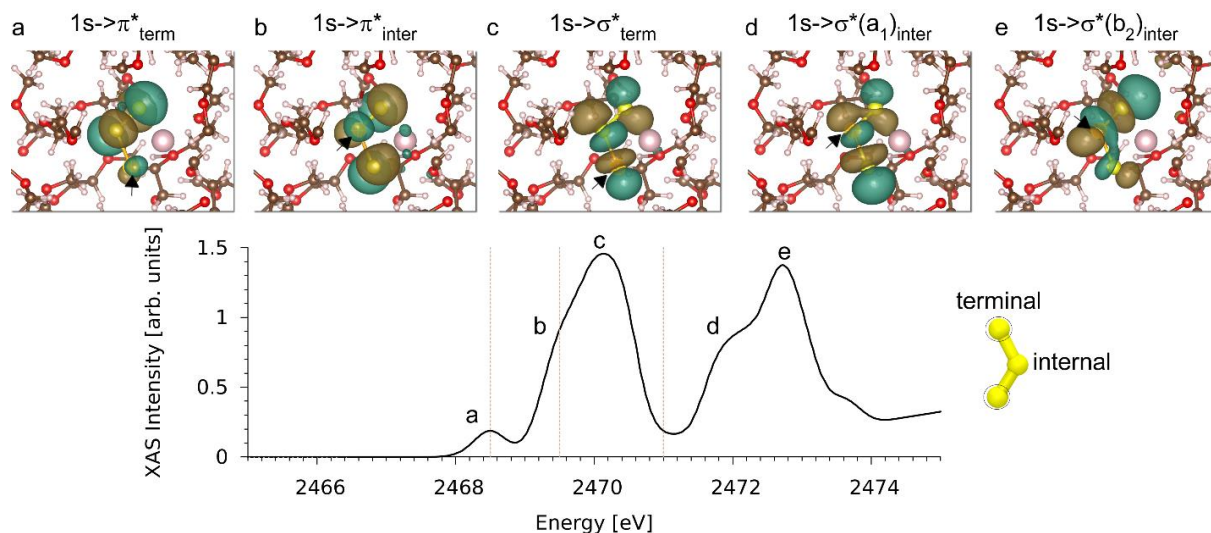


Figure 3.2 First principles XANES spectra of the trisulfur LiS_3 molecule dissolved in polyethylene oxide (PEO) oligomers obtained from sampling an *ab-initio* molecular dynamics (AIMD) simulation at 298K. Each of the five major transitions that inform the spectra are indicated. These can be grouped as excitation from terminal (a. and c.) or internal (b., d. and e.) sulfur atoms (see schematic in bottom right). *Top inset:* Representative electron density of the resulting excited states. We adopt the convention that the positive phase of the density is colored gold while the negative phase is colored green. The carbon (gray), oxygen (red), and hydrogen (silver) PEO atoms near the LiS_3 molecule are shown. The lithium atom (pink spheres) are also shown. The excited sulfur atom is indicated by the crossed sphere and the arrow.

The first-principles simulated XAS spectrum of a single LiS_3 molecule dissolved in TEGDME is presented in Figure 3.2, and can generally be described as having three main features:

- 1) a low energy peak centered near 2468.5 eV that does indeed arise from $1s \rightarrow \pi^*$ transitions; our analysis indicates that this feature only arises from transitions originating from sulfur 1s core orbitals on either of the two terminal atoms;
- 2) a broad, main feature centered near 2470.1 eV with σ^* character, that also arises primarily from transitions originating from terminal atoms; we find a low energy shoulder on this main peak, near 2469.5 eV, originating from π^* excitations of the internal sulfur atom;
- 3) another broad peak near 2472.7 eV that arises from σ^* transitions originating from the internal sulfur atom.

In the following analysis, we will focus on spectral contributions to the S K-edge XAS at energies below the white line. Spectral features above this energy for our sulfur-rich samples are undoubtedly affected by overabsorption and perhaps other effects outside the scope of the present study. We note that while the lower energy of the LiS_3 π^* compared to the σ^* transition is easily understood from standard molecular orbital theory,⁽⁹⁸⁾ the 1 eV splitting between the π^* transitions originating from the terminal and internal sulfur atoms may appear surprising. In fact, this splitting reflects the increased partial atomic charge around the terminal atoms in the ground state; an effect that reduces the binding energy of their 1s core electrons and thus red-shifts their spectral contribution, reminiscent of the core-level shift effect that informs X-ray photoemission spectroscopy.

We find that the calculated low energy π^* peak of the trisulfur radical anion near 2468.5 eV has 1/10th the intensity of the pre-edge feature, due to the delocalized nature of the core-excited π^* molecular orbital compared to the σ^* . We also note that the π^* peak is also not nearly as broad as the pre-edge, due to the lower sensitivity of the π^* molecular orbital to bond length variation at finite temperature (with its electron density above and below the molecular plane) than the σ^* orbital (which has electron density along the S - S bond). Based on these estimates, we conclude that the relatively weak and narrow π^* peak (labeled a in Figure 3.3) cannot be the only reason for the observed low energy shoulder (labeled a in Figure 3.2) in sample I.

3.3.2.2. Longer-chain polysulfide radicals

In order to explain the origin of the low energy shoulder in the XAS of sample I, we considered longer-chain polysulfide radicals. This was inspired by our previous work, which showed that dissolved polysulfide dianions have slightly longer S - S bond lengths which leads to a red-shift in their XAS peaks.⁽⁵⁵⁾ To test this hypothesis, we calculated the spectra of LiS_4 and LiS_5 species dissolved in TEGDME. As shown in the inset of Figure 3.3, the thermodynamically favored geometry of the lithium - radical anion complex in solution is a “claw” structure, with the lithium ion bound to three sulfur atoms, while simultaneously interacting with an oxygen atom on a nearby glyme molecule. In contrast to the three distinct peaks in trisulfur, the XAS of the longer-chain polysulfide radicals are found to be characterized by broader features. In fact, we find that the spectrum of LiS_5 contains only two main features, reminiscent of the spectra of the Li_2S_5 dianion.⁽⁵⁵⁾ Therefore, we predict that XAS can distinguish between the LiS_3 , LiS_4 and LiS_5 polysulfide radicals. Our simulated XAS of the longer chain radicals [LiS_x ; $x = 6,7,8$] in vacuum indicate that their spectra are virtually indistinguishable from those of the dianions.⁽⁹⁸⁾ Thus we chose the calculated XAS of the dissolved dianions from our previous work⁽⁵⁵⁾ to be representative. This catalog of reference radical anion and dianion spectra from our first principles calculations then allowed for a semi-quantitative fit to experiment.

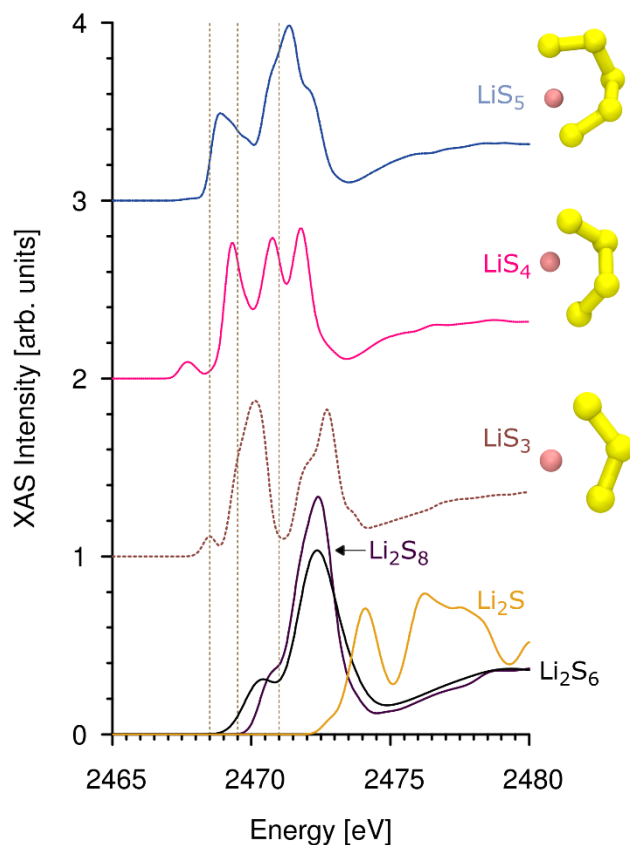


Figure 3.3 Calculated sulfur K-edge XANES spectra of the solvated radical LiS_5 (blue), LiS_4 (pink) and LiS_3 (brown) molecules. The XANES spectra of the Li_2S_6 (black) and Li_2S_8 (purple) dianions, as well as crystalline Li_2S (gold) from our previous study⁽⁵⁵⁾ are also included. *Right insets:* Thermodynamically favored state of lithium polysulfide dissolved in PEO from AIMD simulations.

3.3.3. Fingerprinting of measured XAS using theory

As already stated, we interpret our XAS measurements using our first-principles spectral standards. Before discussing the results of the fitting procedure, it is important to note the limitations of this approach. First, while the experimental spectra primarily represent the polysulfide species dissolved in the electrolyte separator, it is likely that a minor portion of the incident X-rays were able to pass through the electrolyte (25 μm) and reach the cathode. We have calculated that incident photons have a roughly 18% probability of transmitting through our particular cell, to the cathode, and out to the fluorescence detector. Thus, it is possible that unreacted sulfur in the cathode may manifest itself in the spectra. Second, the obtained spectra are affected by X-ray overabsorption. This causes features at and above the absorption K-edge to be dampened, and features below the edge to effectively appear more intense.^(51, 76, 77) While this complication could have been avoided by using a much thinner electrolyte separator (< 200nm), doing so would have resulted in spectra dominated by the cathode. Third, our calculations generally underestimate the oscillator strength of transitions beyond the main edge⁽⁵⁵⁾. Finally, while we present a “best fit” to the experimental spectra; the fit is by no means unique. In fact, other linear combinations provide calculated spectra similar in shape to those shown presently, although they are only slightly different in quantitative composition.

3.3.3.1. Initial discharge at 2.25V

The measured XAS spectrum for cell I and the fitted spectrum are shown in Figure 3.4. The energy scale is divided into four regions labeled A, B, C, and D. Also shown in Figure 3.4 are the weighted contributions from individual species to the overall spectrum. A visual comparison of the computed LiS_3 spectrum (Figure 3.3) and the measured spectrum of cell I (Figure 3.4) indicates that the low energy shoulder cannot be exclusively attributed to LiS_3 as suggested in the literature. In fact, we need to introduce LiS_4 and LiS_5 in order to obtain quantitative agreement between theory and experiment. The apparent presence of these longer chain radical polysulfides is consistent with the ex-situ mass spectrometer results of Kawase and coworkers.⁽¹¹³⁾ These three species dominate the low energy shoulder that occupies regions A and B (Figure 3.4). At energies above 2469 eV contributions from the Li_2S_6 dianion become evident (regions B and C). Introduction of S_8 is essential for obtaining agreement between experiment and theory in region D. The final spectral decomposition of sample I obtained from our least squares fit (LSF) was 30% contribution from S_8 , 25% LiS_5 , 22% Li_2S_6 or Li_2S_8 , 8% LiS_3 , and 16% LiS_4 (Table 3.1) In other words, a linear addition of the theoretical spectra of the pure species listed above with the given weighting results in the dotted curve shown in Figure 3.4.

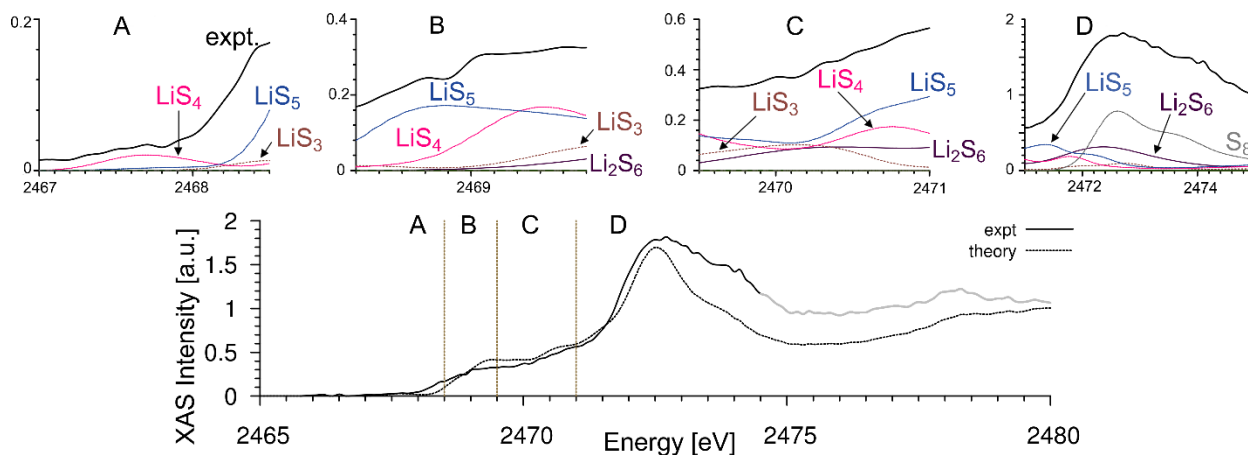


Figure 3.4 S K-edge XAS during initial stage of discharge (point I. in Figure 3.1). We present a best fit of the experimental data (solid line) using independent spectra obtained from first principles calculations (dashed line). Due to the likeliness that features above 2474.5 eV stem from radiation damage, fitting is performed below this energy. Four separate regions are identified: **region A**: Features < 2469 eV resulting from $1s \rightarrow \pi^*$ transitions of the terminal sulfur atoms on the radical species. **region B**: Features between 2469 and 2470 eV arising primarily from $1s \rightarrow \sigma^*$ transitions in the terminal atoms of the radical species. **region C**: The so-called “pre-edge” between 2470 and 2471.5 eV, arising primarily from $1s \rightarrow \sigma^*$ on the terminal sulfur atoms of the Li_2S_6 dianion and the $1s \rightarrow \pi^*$ transitions on the internal atoms of radicals. **region D**: The main edge (including the sulfur white line), resulting primarily from $1s \rightarrow \sigma^*$ excitations of the internal sulfur atoms. *Top outliers*: Zoom of each region, showing the experimental spectra (solid black line) and relative amounts of each of the theoretical spectra in that energy range. The chemical character of the XANES features are also indicated.

Our analysis indicates that sample I contains a complex mixture of radical anion and dianion sulfur species. Instead of the spectral compositions obtained from our LSF procedure, we

could instead consider the corresponding molecular composition, obtained by normalizing with respect to the number of sulfur atoms in each molecule. The results (Table 3.2) show that the electrolyte contains 17% long chain polysulfide dianions (Li_2S_8 or Li_2S_6), about 62% polysulfide radical anions (LiS_3 , LiS_4 , and LiS_5), and 20% S_8 . The 20% of the insoluble S_8 present in the spectra is attributed to unreacted sulfur in the cathode. The absence of short chain polysulfide dianions (Li_2S_x , $x = 2$ to 5) is noteworthy and indicates the long-term stability of the long chain polysulfide dianions.

Table 3.1 Exact weights of component spectra used in linear component fits in Figures 3.4 and 3.5.

	Voltage (V)	S_8 (%)	Li_2S (%)	LiS_3 (%)	LiS_4 (%)	LiS_5 (%)	Li_2S_2 (%)	Li_2S_3 (%)	Li_2S_5 or Li_2S_4 (%)	Li_2S_6 (%)	Li_2S_8 (%)
I	2.25	30	0	8	16	25	0	0	0	12	10
II	2.02	4	11	0	0	9	0	16	41	20	0
III	1.5	0	17	0	0	0	20	33	30	0	0

Table 3.2 Molecular composition of samples I, II, and III in terms of six broad families of species: solid S_8 and Li_2S , radicals, short dianions [Li_2S_x ; $x = 2$ to 5] and long dianions [$x = 6,7,8$]

	S_8 (%)	Li_2S (%)	radicals (%)	dianions(short) (%)	dianions(long) (%)
I	20	0	62	0	17
II	2	36	6	45	11
III	0	39	0	61	0

3.3.3.2. Subsequent depths of discharge

The same approach was used to interpret the measured XAS of samples II and III. Comparisons between theory and experiment are shown in Figure 3.5. Overall, we find that the spectrum of sample II is dominated by short chain polysulfide dianions, as well as a small molecular fraction (~6%) of the LiS_5 radical anion in order to reproduce the low energy intensity. The main difference between samples I and II is the dramatic decrease in XAS signatures of the LiS_3 and LiS_4 polysulfide radicals, the decreased concentration of unreacted sulfur (to 2%), and for the first time, evidence of significant amounts of solid Li_2S (36%). The decrease in sulfur content may be due to its expected reduction and consumption through electrochemical reactions, or it may also reflect a decrease in X-ray transmittance of the electrolyte, due to the increased concentration of dissolved polysulfide species. In summary, short chain dianions dominate the spectra of sample II, with estimated molecular concentrations of 45%, compared to 11% for the long chain dianions.

Finally, we find that the molecular composition of sample III is relatively simple, comprising 61% short chain dianions (23 % Li_2S_2 , 25 % Li_2S_3 , 13 % Li_2S_5) and 39% Li_2S . It is not clear if the Li_2S detected in our experiments is located within the cathode or the product of side reactions between the lithium metal anode and polysulfides.

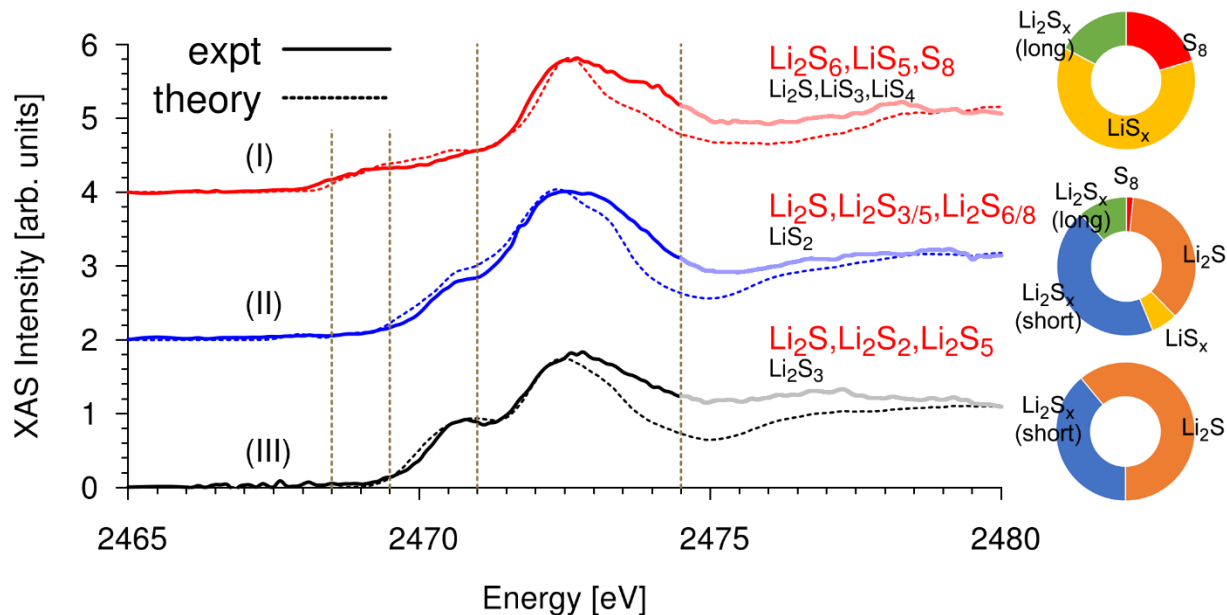


Figure 3.5 Comparison of the best fit spectra from theory (dashed lines) compared to experiments (solid lines) for each of the three voltages. The isolated species used to obtain the best fit are also indicated: the major components are in red, while the minor components are in black. *Right insets:* Relative molecular composition ratios of types of sulfur species (S_8 (red), Li_2S (orange), radicals (yellow) and dianions) from our LSF. We separately consider short (Li_2S_2 to Li_2S_5 , blue) and long ($Li_2S_6/Li_2S_7/Li_2S_8$, green) polysulfide dianions.

3.3.4. Discharge mechanism

Some care must be taken when drawing conclusions regarding the sulfur reduction mechanism from the results given above. It is not clear for example, if the species we have identified arise due to electrochemical reactions or from subsequent chemical (disproportionation) reactions. Given the complexity and variety of the species identified in Table 3.1, it is clear that proposing a unique reaction scheme from this data alone is not possible. The same limitations apply to all previous efforts to determine the sulfur reduction mechanism.^(18, 44, 69, 83, 93) Nevertheless, we can propose reaction schemes that are consistent with our data. Such a scheme that accounts for the majority of species detected by our LSF procedure is shown below, and only applies to extremely slow discharge rates.

Step I: Discharging the battery from the original open circuit voltage to 2.25 V, and assuming that elemental sulfur is first converted to Li_2S_8 by reaction 3.1, the polysulfide radical anions of LiS_3 , LiS_4 , and LiS_5 are formed by reactions 3.2a and 3.2b.



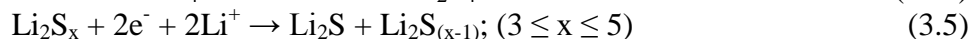
(We assume that the LSF signature of pure sulfur arises because reaction 3.1 does not go all the way to completion). From reaction 3.2a, we would expect equal amounts of LiS_3 and LiS_5 , however our molecular composition analysis indicates nearly twice as many molecules of LiS_5 ,

as well as the presence of Li_2S_6 . We note that due to the similarity in the XAS, we could not uniquely quantify the amount of Li_2S_6 versus Li_2S_8 (a 1:2 ratio leads to the best fit). Taken together, our results suggest an additional combination reaction of LiS_3 to form Li_2S_6 as given by reaction 3.3.



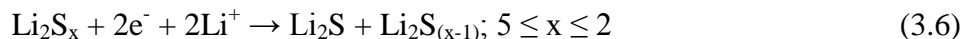
Note that reaction 3.3 is the reverse of the equilibrium reaction commonly assumed as the origin of the trisulfur radical species in the literature. ^(39, 40, 42, 65, 87)

Step II: Discharging the battery to 2.02 V, radical anions produced at the cathode in step I are no longer present at this step. This could, in principle, results from either electrochemical consumption or subsequent chemical reactions in the electrolyte. For concreteness, we propose an electrochemical pathway wherein the radical anions are electrochemically converted into dianions (reactions 3.4a, 3.4b, and 3.4c), which are reduced subsequently to give Li_2S (reaction 5).



Based on our LSF analysis, we propose that reactions 3.4a and 3.4c go to completion, while reaction 4b does not (i.e. a small amount of LiS_5 is still detected). Similarly reaction 3.5 appears not to go to completion, as Li_2S_6 and Li_2S_8 are detected. Due to the similarities in the XAS of Li_2S_5 and Li_2S_4 , we are unable to differentiate between these species. It is thus conceivable that Li_2S_4 is present in the electrolyte via reaction 3.4c. Alternatively, the electrochemical consumption of long chain polysulfides by reaction 3.5 may drive chemical reactions 3.2a and 3.2b in the reverse direction, thereby reducing radical anion concentrations.

Step III: Discharging the battery to 1.50 V results in significant quantities of short chain polysulfides. This implies that the longer chain polysulfide dianions continue to be converted to Li_2S in the cathode, as described by reaction 3.6. Presumably the experimentally measured XAS signal is dominated by polysulfides dissolved in the electrolyte, significantly attenuating the signal from the insoluble Li_2S in the cathode.



3.3.5. Comparison to previous work

Finally, we note that in a previous study, we determined species formed by chemical reaction of Li_2S and S_8 in the same electrolyte (poly(ethylene oxide)) used here, ⁽³⁰⁾ with one significant difference now being the presence of lithium perchlorate salt necessary for enabling electrochemical reactions in this study. The main conclusion of our previous work using chemically prepared samples was the proliferation of dissolved lithium polysulfide dianions and the absence of any signal of polysulfide radicals, in contrast to the significant signature of these

radicals in the present study in the sample discharged to 2.25V. Since these chemically prepared samples do not have a source of excess electrons, the electrochemical pathways enumerated above are unavailable and hence the speciation is fundamentally different. This fundamental difference is most clearly exemplified by noting the alternative pathway for the formation of Li_2S_6 during the electrochemical process, i.e. through the recombination of LiS_3 radical anions. In a recent study, Wang et al determined the nature of lithium polysulfide species formed in DOL-DME mixtures in both chemically and electrochemically synthesized systems.⁽⁴²⁾ They used ESR measurements to prove the presence of radical anions in both systems. This is qualitatively different from results obtained in PEO. Numerous studies have shown that polysulfide speciation is highly solvent-specific.^(33, 65, 86) Therefore, while illuminating for Li-S electrochemistry in general, the proposed discharge mechanism may prove specific only to solid-state ether-based electrolytes.

3.4. Conclusions and Outlook

The equilibrium populations of various lithium polysulfide species formed during the discharge of a lithium sulfur battery with an ether-based electrolyte were studied by a combination of theory and experiment. X-ray absorption spectroscopy experiments were conducted on batteries that were discharged to predefined potentials and allowed to rest for three days. The experiments were designed to probe the polysulfide species present in the electrolyte as opposed to the transient species formed at the cathode. Spectral fingerprints of S_8 and Li_2S solids, polysulfide dianions and polysulfide radical anions obtained from first-principles calculations were used to interpret the experimentally measured spectra. It was found that a collection of polysulfide radical anions and long polysulfide dianions dominate the electrolyte composition after the early stage of discharge. As discharge proceeds, the concentration of radical anions decreases and a mixture of short and long chain polysulfide dianions is obtained. At full discharge, the electrolyte contains neither radical anions nor long polysulfide dianions, but solid Li_2S and short polysulfide dianions. A suggested mechanism that is consistent with these findings is then presented. Our use of spectral fingerprints based on first-principles calculations distinguishes this study from previous attempts to determine the mechanism of electrochemical sulfur reductions.

Interpretation of S K-edge XAS on Li-S battery materials is challenging, primarily due to the lack of established standards, but also since the determined populations do not necessarily represent the species formed initially through the active electrochemical process. While some of the observed species may be active role players in the electrochemical process near the electrodes, others may only originate through subsequent disproportionation reactions within the electrolyte. The more explicit importance of our results is that they represent distributions of polysulfide intermediates thermodynamically favored at equilibrium at different points in the discharge curve. In particular, we have shown that radical anions are stable in ether-based electrolytes, and that their consumption most likely occurs electrochemically. In future work, we intend to explore how the composition of the polysulfide intermediates changes with time after discharge has been stopped. It will be critical to obtain first-principles predictions for the species initially formed electrochemically and their thermodynamic chemical stability. Such predictions will need to be correlated to a time-dependent mapping of polysulfide distributions using XAS. These studies will yield important information regarding the kinetics of disproportionation reactions, in particular those that result in the formation of radicals.

3.5 Acknowledgements

This work was supported by the Assistant Secretary for Energy Efficiency and Renewable Energy, Office of Vehicle Technologies of the U.S. Department of Energy under Contract DE-AC02-05CH11231 under the Batteries for Advanced Transportation Technologies program. Theoretical work was supported by a User Project at The Molecular Foundry and calculations were performed at NERSC, while XAS measurements were made at The Advanced Light Source. The Berkeley Lab User Facilities are supported by the Director, Office of Science, Office of Basic Energy Sciences, of the U.S. Department of Energy under Contract No. DE-AC02-05CH11231.

Chapter 4 – Lithium Polysulfide Radical Anions in Ether-Based Solvents[†]

ABSTRACT

Lithium sulfur batteries have a theoretical specific energy five times greater than current lithium ion battery standards, but suffer from the issue of lithium polysulfide dissolution. The reaction mechanisms that underlie the formation of lithium polysulfide reaction intermediates have been studied for over four decades, yet still elude researchers. Polysulfide radical anions formed during the redox processes have become a focal point of fundamental Li-S battery research. The formation of radical species has even been shown to be advantageous to the electrochemical pathways. However, whether or not polysulfide radical anions can form and be stabilized in common Li-S battery electrolytes that are ether-based is a point of contention in Li-S battery research. The goal of this work was to examine the presence of radical polysulfide species in ether-based solvents. Lithium polysulfide solutions in tetraethylene glycol dimethyl ether (TEGDME) and poly(ethylene oxide) (PEO) are probed using a combination of ultraviolet-visible (UV-vis) and electron paramagnetic resonance (EPR) spectroscopy. EPR results confirm the presence of radical species in ether-based electrolytes. Comparison of the UV-vis spectra to EPR spectra establishes that the UV-vis absorbance signature for radical species in ether-based solvents occurs at a wavelength of 617 nm, which is consistent with what is observed for high electron pair donor (EPD) solvents like dimethylformamide and dimethyl sulfoxide.

4.1. Introduction

Lithium sulfur (Li-S) batteries are attractive for energy storage applications because they have a theoretical specific energy of 2600 W h/kg, and because sulfur is affordable and naturally abundant.⁽²⁾ Unfortunately, Li-S cells are plagued by issues related to the dissolution of reaction intermediates, collectively called lithium polysulfides, that are formed during charge and discharge. As the redox reactions proceed, these polysulfides dissolve in the electrolyte and diffuse out of the cathode, causing the battery capacity to fade. Additionally, if diffusion to the cell anode occurs, polysulfides may react with lithium, forming insulative layers of Li_2S and Li_2S_2 , and leading to parasitic shuttles if soluble species are formed.^(8, 13, 57)

While lithium polysulfide molecules are most commonly thought to be dianion species (Li_2S_x , $2 \leq x \leq 8$),^(12, 114) evidence of polysulfide radical anions (LiS_x , $3 \leq x \leq 5$) in Li-S batteries has also been obtained.^(31, 32, 42, 93, 115) Recent studies have even suggested that radical anions may be of benefit to Li-S reaction pathways.^(93, 115) It has been argued that the presence of radical species (here we refer to polysulfide radical anions as radicals or radical species for simplicity) in a particular lithium sulfur cell depends primarily on the electron pair donor (EPD) number of the electrolyte.^(11, 116) Solvents with high EPD numbers may stabilize radical polysulfides, while solvents with low EPD numbers do not.

[†] This work is reported in *J. Phys. Chem. C* **120**, 18403-18410 (2016)

The long-term stability of polysulfide radicals in some environments is well-established. This is demonstrated most clearly by lapis lazuli, a blue mineral that is pulverized to form a pigment commonly known as ultramarine. Through extensive studies involving electron paramagnetic resonance (EPR) spectroscopy, Raman spectroscopy, ultra violet-visible light (UV-vis) spectroscopy, and X-ray absorption spectroscopy (XAS), the blue color of ultramarine/lapis lazuli has been attributed to the $S_3^{\cdot-}$ trisulfur radical anion.^(28, 97, 117) The crystalline tectosilicate cage-structure of the mineral stabilizes the radical anion, apparently isolating the individual molecules and preventing recombination of these reactive species. Additional studies on the chemical composition of ultramarine/lapis lazuli suggest that $S_2^{\cdot-}$ may also be present.⁽¹¹⁸⁾ The $S_3^{\cdot-}$ radicals that give the blue color of ultramarine pigments have been stable for thousands of years.

Polysulfide radicals have been reported to be stable in solvents such as DMF and DMSO that have high EPD numbers. Radical species like LiS_3 and LiS_4 were detected in equilibrium with dianion species (e.g. Li_2S_6) in these systems by X-ray absorption spectroscopy (XAS), electron paramagnetic resonance spectroscopy (EPR) and UV-vis absorbance spectroscopy.^(8, 11, 23, 26, 27, 33, 38, 40, 41, 43, 65, 87, 119-125) Solutions of polysulfide species in solvents with high EPD numbers are typically blue in color, owing to the presence of LiS_3 .^(8, 11, 43, 119)

It is not clear if polysulfide radicals are present in solvents with low EPD numbers, such as dimethylether (DME), 1,3-dioxolane (DOL), tetraethylene glycol dimethyl ether (TEGDME), and poly(ethylene oxide) (PEO). Some studies indicate the presence of radicals in these ether-based systems,^(31, 32, 42, 115, 116) while others do not.^(18, 30, 34, 35, 69, 93, 126) Establishing the stability of radicals in these ether-based electrolytes is important because these solvents are often used in Li-S cells.^(7, 12, 18, 31, 42, 69, 127)

In this paper, we quantify the presence of radicals in chemically synthesized lithium polysulfides in TEGDME and PEO using a combination of UV-vis and EPR spectroscopy. Our results provide unambiguous proof of the existence of radical anions in these solvents, and show that the concentration of radical species is a complex function of polysulfide type and concentration. Based on the observed EPR g-factors, the identification of the radical species present in the ether-based solvents is discussed, but further work is needed to confirm the exact radical species present in solutions.

4.2. Experimental

4.2.1 Materials

Lithium sulfide (Li_2S) and elemental sulfur (S_8) were purchased from Alfa Aesar and were received under argon. Tetraethylene glycol dimethyl ether (TEGDME) (99.0 %) was purchased from Sigma Aldrich and was obtained under argon. Poly(ethylene oxide) (PEO), also referred to as poly(ethylene glycol), was purchased from Polymer Source Inc. and had a molecular weight of 600 g/mol. The PEO was dried overnight at 90 °C under vacuum and then brought into the glovebox. All materials were stored in an argon filled glovebox.

4.2.2 Lithium polysulfide solutions

Lithium polysulfide solutions were prepared by adding stoichiometric amounts of S_8 and Li_2S to the solvent of interest as described by Rauh et al.⁽⁸⁾ The amounts of S_8 and Li_2S added to solutions were controlled by the following formula:



Here, ' x_{mix} ' is used to denote the polysulfide dianion that would be obtained if a single dianion polysulfide type were formed by the reaction. In reality, the solution is likely a mixture of various polysulfide species in equilibrium, formed through various disproportionation reactions. This distribution of polysulfide species can include both dianions (of the form Li_2S_x) and radical species (of the form LiS_x).⁽⁸⁾ Here, ' x_{mix} ' is used simply as a descriptor of the atomic ratio of lithium to sulfur. Solutions were mixed for at least 24 hours at 90 °C in a sealed vial within an argon-filled glovebox.

Solution sulfur concentrations (referred to as C_S) used here represent the overall atomic moles of sulfur per volume of solution. For instance, a 10 mM concentration solution contains 10 millimoles of atomic 'S' per liter of solution. The millimoles of 'S' atoms represents the sulfur added in the form of S_8 and Li_2S .

To maintain consistent ' x_{mix} ' values throughout the study, 'bulk', high concentration solutions were made for each x_{mix} value which were then used to produce the lower concentration solutions through dilution. For instance, the TEGDME $x_{\text{mix}} = 6$ solutions were made by first preparing a bulk $x_{\text{mix}} = 6$, 300 mM solution. This 300 mM solution was then diluted down to create the 100, 50, and 10 mM solutions. This procedure was used for all x_{mix} values. Additions of TEGDME and PEO were performed using a micropipette.

4.2.3 UV-vis spectroscopy

Liquid lithium polysulfide solutions were loaded into quartz cuvette sample holders inside an argon-filled glovebox. The quartz cuvettes had a path width of 1 mm. After loading, cuvettes were sealed and then placed in closed vials with Teflon tape wrapped between the glass threading of the vial and the cap. Vials were then brought out of the glovebox and to the UV-vis spectrophotometer. There, cuvettes containing the samples were taken out of the vials and immediately measured. An Agilent Cary 5000 UV-Vis-NIR spectrophotometer was used to measure the samples in a range of wavelengths spanning 200-820 nm. Data was obtained in transmission mode. Within the range of sulfur concentrations probed here ($C_S = 10, 50, \text{ and } 100$ mM), absorbance spectra became oversaturated below 300 nm. For that reason, our analysis of the UV-vis results is restricted only to the absorbance above 300 nm for all samples. This is of importance, given that the absorbance of elemental sulfur occurs in the 200-300 nm range.⁽³²⁾ The measured spectra thus may not represent all of the sulfur-containing species in the samples. Measurement of 300 mM sulfur concentration solutions was attempted, but spectra were oversaturated in the 200-820 nm wavelength range. Spectra were taken for each solvent (TEGDME and PEO); solvent spectra were subtracted from the polysulfide solution spectra shown throughout the rest of this writing. All solutions were measured at room temperature.

4.2.4 Electron paramagnetic resonance spectroscopy

Lithium polysulfide solutions were loaded into borosilicate capillary tubes obtained from Active Spectrum, having an outer diameter of 2.3 mm. Roughly 0.1 mL of solution was loaded into each capillary tube. This volume surpassed the volume of solution present in the measurement cavity of the EPR instrument, meaning that the sample geometry and total solution

volume probed for each measurement was identical from sample to sample. Capillary tubes were sealed using a Cha-seal tube sealing compound. The small capillary tubes were then placed inside larger 5 mm outer diameter quartz tubes (Wilmad-LabGlass) that were capped with standard NMR tube caps. Kapton tape was then wrapped around the top of the tube and over the cap to assure an air-tight seal. All sample preparation was performed in an argon-filled glovebox.

Continuous wave (CW) EPR was performed in the X-band frequency range, approximately 9.69 GHz, using an Active Spectrum extended range benchtop EPR instrument. All spectra were obtained at room temperature. The microwave power was set to be 15 mW for all samples. This power was in the linear regime of the power saturation curve obtained for the samples, indicating a quantitative relationship between the double integral of the EPR peaks and sample concentration. The magnetic field had a modulation frequency of 100 kHz, and a modulation amplitude of 2 G. Spectra were taken between 2900-3900 G at a sweep rate of 7.18 G/s. Two batches of samples were prepared for the set of polysulfide solutions (each solution thus had two separately prepared samples). Five scans were performed and averaged together for each sample. The spectra shown herein are the spectra obtained for one of the sample batches. Raw spectra were smoothed using a second order Savitsky-Golay filter algorithm, with a frame size of 4 G. Spectra were obtained for the capillary tubes, TEGDME, and PEO. These background spectra were subtracted from the lithium polysulfide mixture spectra.

4.3. Results/Discussion

4.3.1 UV-vis spectroscopy of lithium polysulfide solutions

Figure 4.1 shows UV-vis spectroscopy results for TEGDME lithium polysulfide solutions at a variety of x_{mix} values and sulfur concentrations (C_S). Here, x_{mix} denotes the ratio of sulfur to lithium ($\text{Li}_2\text{S}_{x_{\text{mix}}}$), as described in reaction 4.1 in the Experimental section. UV-vis spectra were obtained for x_{mix} values of 4, 6, 8, and 10; and sulfur concentrations of 10 mM, 50 mM, and 100 mM. For ether-based solvents, the peaks in the 300-550 nm range are generally attributed to polysulfide dianions.^(31, 32, 35) The identity of the peak at 617 nm has not been confirmed for ether-based polysulfide solutions. While some have attributed the peak to radical polysulfides,^(31, 32) others have attributed the peak to polysulfide dianions.⁽³⁵⁾ Since our primary interest is to characterize radical anions in ether-based solvents, we focus on the peak at 617 nm.

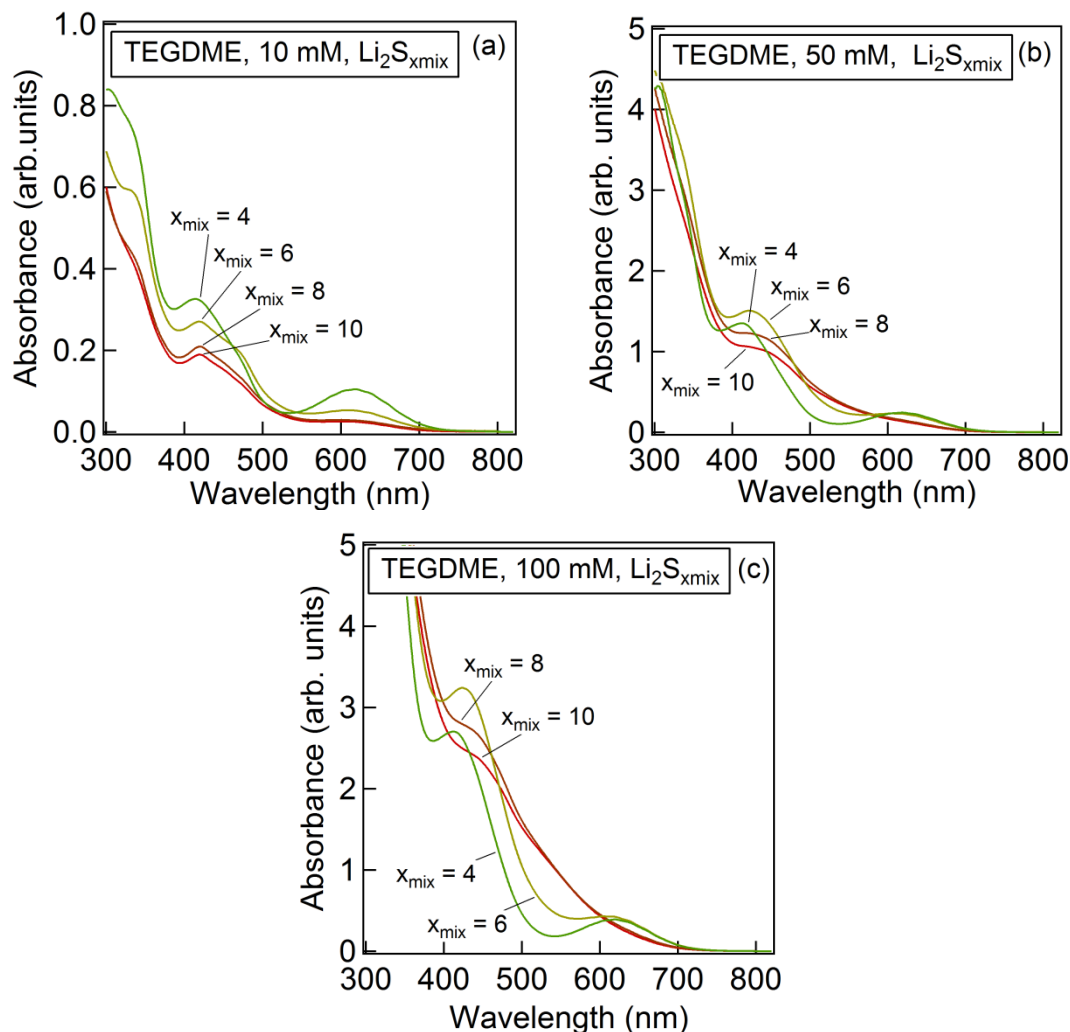


Figure 4.1 UV-vis spectra obtained for TEGDME lithium polysulfide solutions at sulfur concentrations of (a) 10 mM, (b) 50 mM, (c) 100 mM. Corresponding colors: $x_{\text{mix}} = 4$ (green), $x_{\text{mix}} = 6$ (yellow), $x_{\text{mix}} = 8$ (brown), $x_{\text{mix}} = 10$ (red).

At 10 mM sulfur concentration, the $x_{\text{mix}} = 4$ solution has the highest absorbance at 617 nm, followed by $x_{\text{mix}} = 6$, $x_{\text{mix}} = 8$, and $x_{\text{mix}} = 10$. At 50 mM (Figure 4.1b), $x_{\text{mix}} = 4$ and $x_{\text{mix}} = 6$ appear to have similar absorbances at 617 nm, again followed by $x_{\text{mix}} = 8$ and $x_{\text{mix}} = 10$. At 100 mM, (Figure 4.1c) an identical trend is observed. The highest absorbance at 617 nm in DMF solutions of lithium polysulfides occurs at $x_{\text{mix}} = 6$.⁽¹²⁰⁾ Our results for TEGDME are thus slightly different, but consistent with data obtained for DMF solutions.^(41, 120) The spectra shown in Figure 4.1 were fit using a series of Gaussian functions. Results of this fitting procedure for the 617 nm peak are shown in Table 4.1. (Parameters corresponding to the other peaks are given in Supporting Information.)

Table 4.1 Gaussian peak amplitude and area for 617 nm UV-vis peak at sulfur concentrations (C_S) of 10 mM, 50 mM, and 100 mM

	$C_S = 10 \text{ mM}$	$C_S = 50 \text{ mM}$	$C_S = 100 \text{ mM}$
--	-----------------------	-----------------------	------------------------

x_{mix}	Amplitude	Area	Amplitude	Area	Amplitude	Area
4	0.103	12.1	0.242	28.2	0.388	45.1
6	0.049	6.0	0.209	24.5	0.386	45.1
8	0.026	3.4	0.076	9.0	0.124	15.7
10	0.022	2.6	0.062	7.3	0.077	10.0

PEO solutions at x_{mix} values of 4, 6 and 8 at a concentration of 10 mM were also examined using UV-vis spectroscopy. The resulting spectra for these solutions are shown in Figure 4.2. Similar to the results obtained for TEGDME, the $x_{mix} = 4$ solution shows the largest absorbance at 617 nm, followed by $x_{mix} = 6$, and $x_{mix} = 8$.

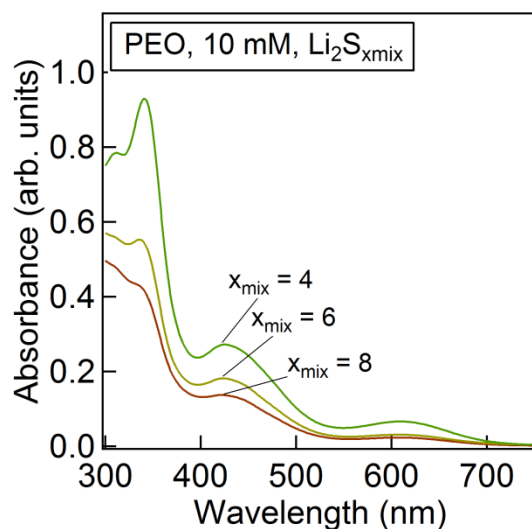















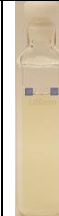




Figure 4.2 UV-vis spectra obtained for PEO lithium polysulfide ($C_s = 10$ mM) solutions

4.3.2 Photographs of lithium polysulfide solutions

Polysulfide mixtures in DMF, DMSO, and like solvents are typically blue in color.^(8, 11, 43, 119) Photographs of the TEGDME and PEO solutions examined in this study are shown in Table 4.2. TEGDME solutions with x_{mix} values equal to 4 were green in color for all concentrations. For $x_{mix} = 6$, solutions were light yellow/green at 10 mM, and then became a dark olive/brown color at high concentrations. The $x_{mix} = 8$ solutions were light yellow/green in color at 10 mM, orange/brown at 50 mM, and dark red at 100 mM. The $x_{mix} = 10$ were light yellow at 10 mM, orange/brown at 50 mM, and dark red at 100 mM. Low concentration $x_{mix} = 4$ PEO solutions were light green/yellow at low concentrations, and dark yellow/brown at higher concentrations; $x_{mix} = 6$ solutions were light yellow at low concentration and red at higher concentrations; $x_{mix} = 8$ solutions were light yellow at low concentration, and red at higher concentration.

Table 4.2 Photographs of UV-vis cuvettes filled with TEGDME and PEO lithium polysulfide solutions.

TEGDME	x_{mix} value			
	4	6	8	10
Concentration (C_S)				
10 mM				
50 mM				
100 mM				

PEO	x_{mix} value		
	4	6	8
Concentration (C_S)			
10 mM			
300 mM			

While the attribution of the 617 nm peak in the UV-vis spectra to a radical anion is consistent with what has been established for DMF and DMSO, the TEGDME and PEO solutions are not blue in color, as is typically the case for radical-containing polysulfide solutions. The low EPD number of TEGDME and PEO (compared to DMF and DMSO), and lack of blue color in these solutions thus brings to question whether or not the 617 nm peak truly represents a radical anion.

4.3.3 Electron paramagnetic resonance spectroscopy of lithium polysulfide solutions

Figures 4.3 and 4.4 show the EPR spectra obtained for TEGDME and PEO solutions, respectively, at a variety of x_{mix} values and concentrations. Radical species are detected in all TEGDME and PEO solutions at the range of concentrations probed. Additionally, the concentration of radical species increased as sulfur concentration increased, which is most clearly shown by the $x_{mix} = 4$ and 6 TEGDME solutions (Figures 4.3a and 4.3b).

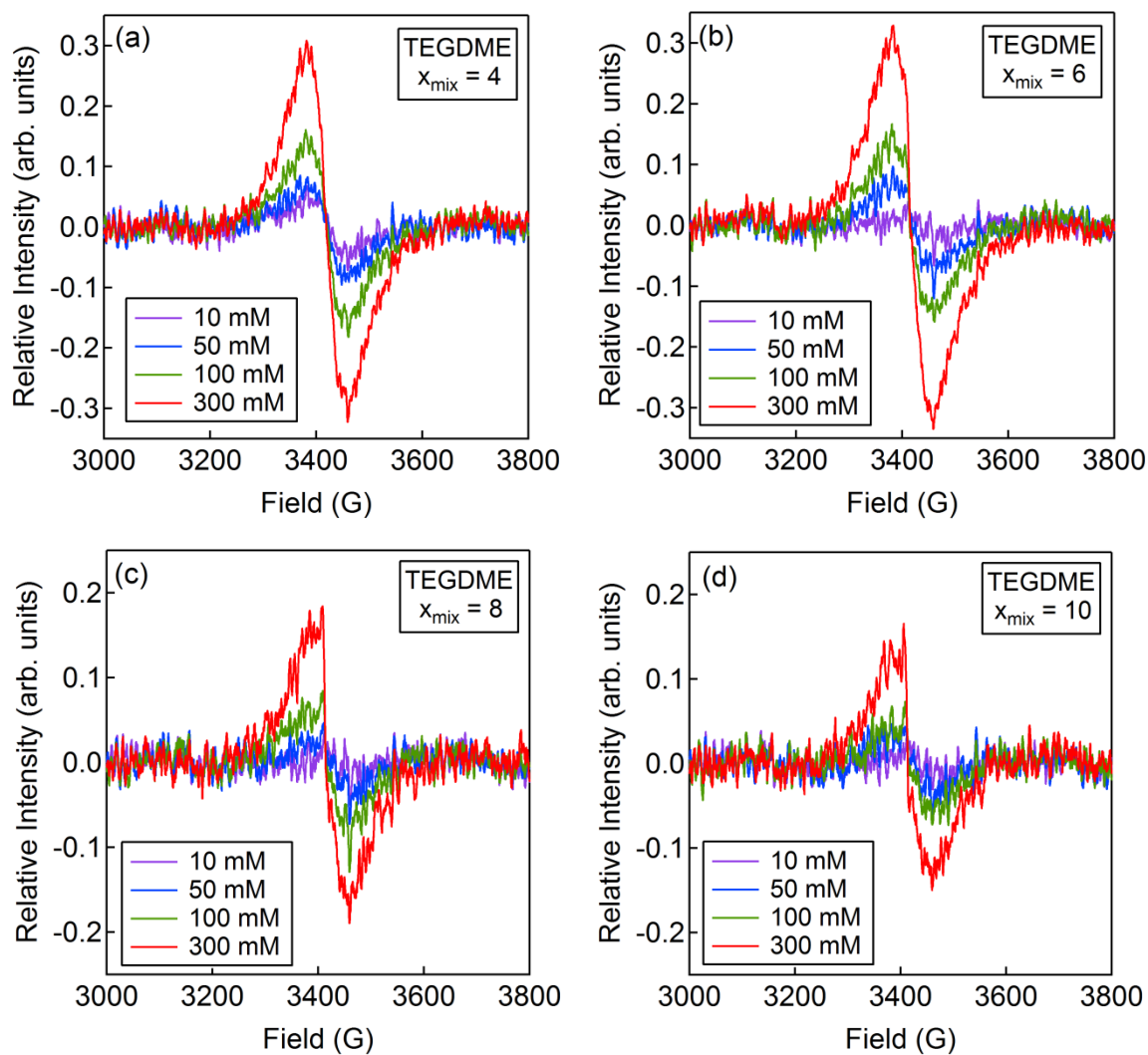


Figure 4.3 EPR spectra obtained for TEGDME lithium polysulfide solutions for x_{mix} values of: (a) $x_{\text{mix}} = 4$, (b) $x_{\text{mix}} = 6$, (c) $x_{\text{mix}} = 8$, (d) $x_{\text{mix}} = 10$ at a range of sulfur concentrations (C_S) between 10 and 300 mM. All spectra were obtained at room temperature.

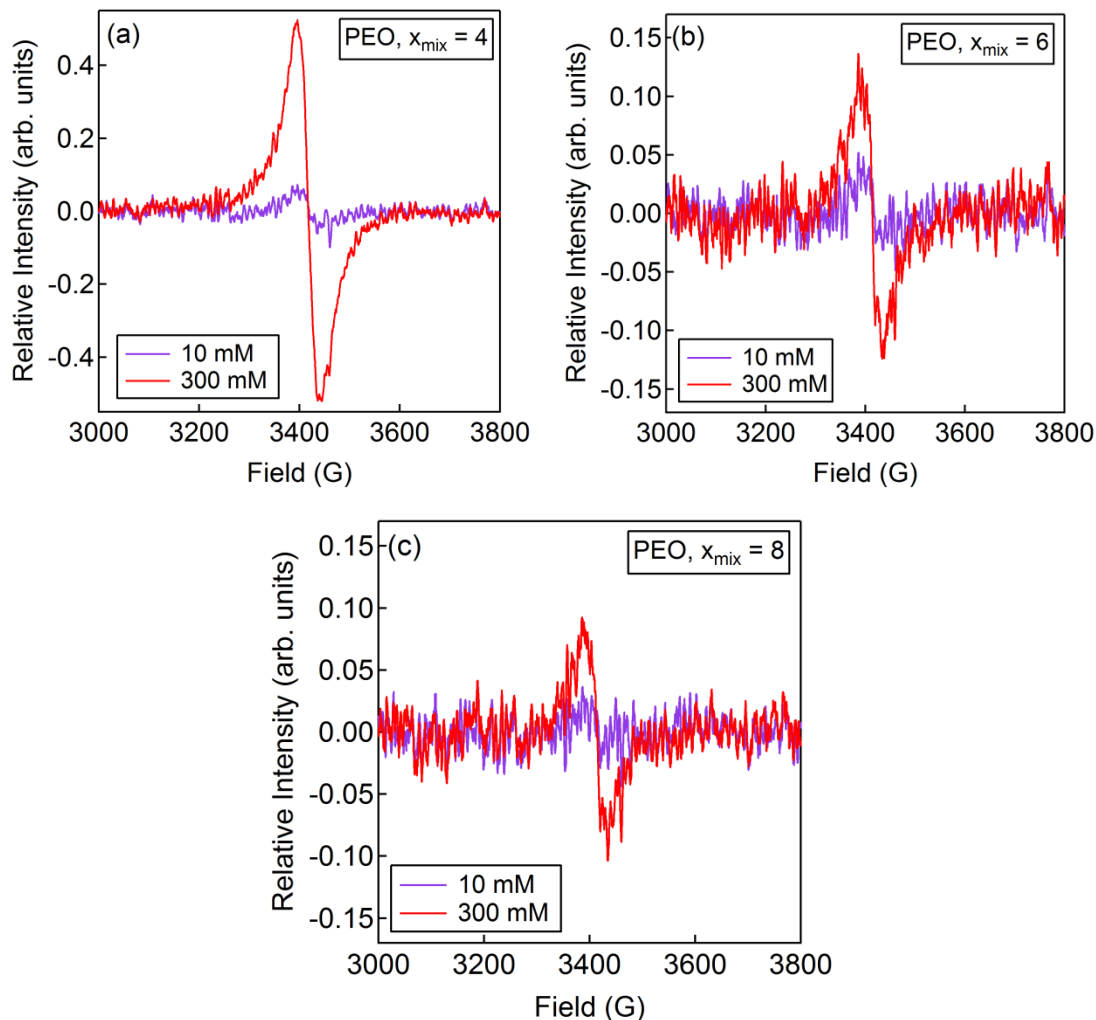


Figure 4.4 EPR spectra obtained for PEO lithium polysulfide solutions for x_{mix} values of: (a) $x_{\text{mix}} = 4$, (b) $x_{\text{mix}} = 6$, (c) $x_{\text{mix}} = 8$ at sulfur concentrations (C_S) of 10 and 300 mM. All spectra were obtained at room temperature.

To obtain more insight regarding the behavior of the EPR spectra in relation to concentration and x_{mix} value, the EPR spectra were fit using a Tsallian first derivative peak function, which was then double integrated to obtain an integrated peak area (here referred to as ‘Double Integral’) proportional to the overall concentration of radical species present.⁽¹²⁸⁾ Integration of the Tsallian fitting reduces the error due to noise and unsteady baselines in the raw data.^(129, 130) (Additional spin-counting experiments necessary to obtain absolute radical concentrations by EPR were not attempted.) Our analysis enables a comparison of radical concentrations in the solutions of interest. The results of the peak fitting are summarized in Table 4.3. The fitting of each spectrum and detailed parameters for each Tsallian fit can be found in the Supporting Information. It is worth noting that while a Tsallian line shape could be fit to the TEGDME $x_{\text{mix}} = 6$, $x_{\text{mix}} = 8$, and $x_{\text{mix}} = 10$, 10 mM spectra, the poor signal to noise of these spectra introduces significant error in the relative concentration of radical species measured in these low sulfur concentration samples, as can be seen from the large errors in the 10mM column of Table 4.3. Additionally, the noise present in these spectra made it difficult to obtain

reliable g-factors for these solutions. Thus, the 10mM solutions were omitted from the calculation of the TEGDME and PEO average g-factors.

Table 4.3 Peak areas obtained by double integration of TEGDME and PEO EPR spectra for $x_{\text{mix}} = 4, 6, 8,$ and 10; sulfur concentrations (C_S) of 10, 50, 100, and 300 mM

		TEGDME Double Integral (arbitrary units)				PEO Double Integral (arbitrary units)	
$x_{\text{mix}} \backslash C_S$	C_S	10 mM	50 mM	100 mM	300 mM	10 mM	300 mM
	4		328 ± 218	740 ± 13	1797 ± 59	3797 ± 702	140 ± 106
6		108 ± 70	632 ± 133	1536 ± 25	4438 ± 78	35 ± 49	510 ± 214
8		35 ± 25	329 ± 185	574 ± 131	1668 ± 200	17 ± 15	294 ± 110
10		23 ± 15	203 ± 3	337 ± 124	1216 ± 218	-	-

The average g-factor obtained for the TEGDME solutions was 2.0294 ± 0.0011 , while that obtained for the PEO solutions was 2.0323 ± 0.0021 . A comprehensive list of each solution's g-factor can be found in the Supporting Information. These g-factors are similar to those previously obtained for the S_3^- radical (2.029)^(11, 26, 42, 119, 120, 131) and the S_4^- radical (2.031).⁽⁴¹⁾ Conclusive identification of the radicals present in the TEGDME and PEO solutions will be a focus of future work, as it is difficult to determine given the broad line width and low signal to noise ratio of the spectra. For now, the general agreement between g-factors obtained here and those previously obtained for polysulfide solutions serves to show that the radical species elucidated by EPR are most likely polysulfide species.

4.3.4 Comparison of UV-vis and EPR results

The EPR results show that radical species are certainly present in the TEGDME and PEO polysulfide solutions, despite their green, red and brown colors and despite their low EPD numbers. Other researchers have also detected polysulfide radicals in ether-based solvents by EPR.⁽⁴²⁾ However, the correspondence between EPR signals and UV-vis data for ether-based polysulfide solutions has not been established. We do this in Figure 4.5. In Figure 4.5a, we plot the peak areas obtained at the 617 nm UV-vis wavelength versus x_{mix} value for three concentrations. In Figure 4.5b, we plot the peak area obtained by double integration of the EPR spectra versus x_{mix} for the same concentrations. The lines connecting the data points in Figures 4.5a and 4.5b are presented only as a guide for the eye. The trends observed in Figures 4.5a and 4.5b are nearly identical. Further, we plot the UV-vis peak areas versus the EPR double integral in Figure 4.6. To a first approximation, the UV-vis 617 nm peak area is directly proportional to the EPR double integral. It is evident that the UV-vis peak at 617 nm of TEGDME and PEO solutions is due to the presence of polysulfide radical anions.

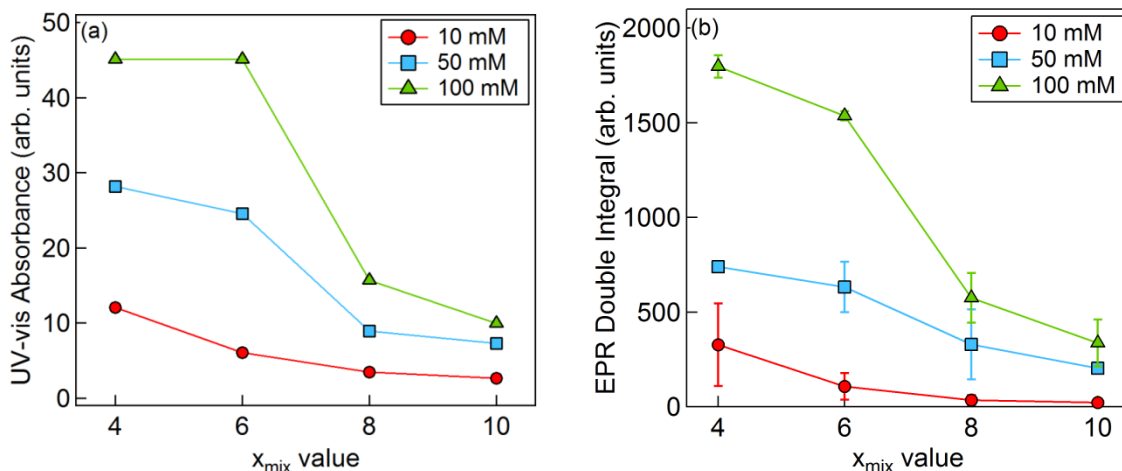


Figure 4.5 (a) Peak area obtained for the UV-vis 617 nm absorbance peak and (b) the double integral of the EPR spectra as a function of lithium to sulfur ratio (x_{mix}) at sulfur concentration (Cs) between 10 and 100 mM. Lines connecting the data points provided as a guide for the eye.

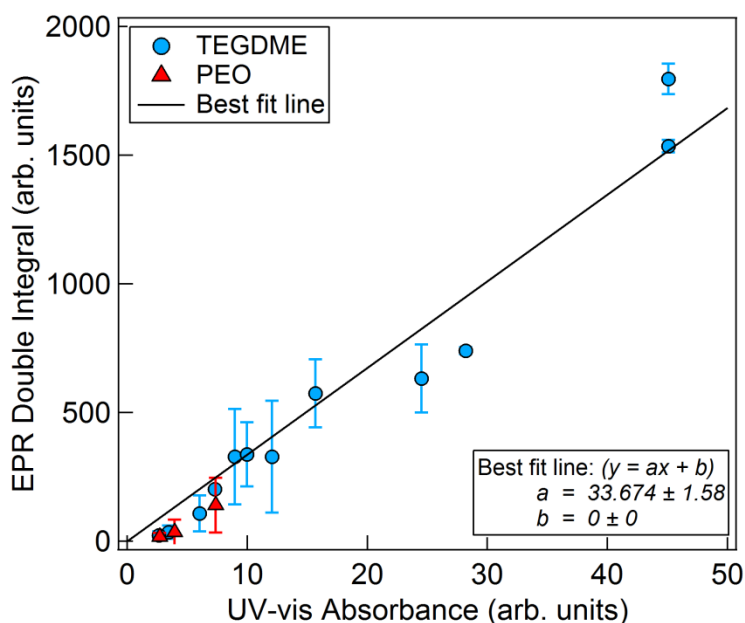


Figure 4.6 UV-vis peak area (617 nm) versus the double integral of the EPR spectra for TEGDME and PEO solutions. Peak areas obtained from UV-vis and the EPR double integrals are proportional, indicating a direct relationship between the 617 nm UV-vis feature and presence of radical anions.

4.3.5 Determination of polysulfide radical anion concentration in TEGDME

To gain insight into the concentration of radical species present in the TEGDME polysulfide solutions, the UV-vis data was used to calculate radical concentrations according to Beer-Lambert Law:

$$A = \varepsilon C_R l \quad (4.2)$$

Here, the absorbance, A , is taken to be the absorbance value at the 617 nm peak maximum; C_R is the concentration of radical species present, l is the path length within the cuvette, and ϵ is the absorption coefficient at 617 nm. We used an absorption coefficient of $4115 \text{ M}^{-1} \text{ cm}^{-1}$, as previously obtained by Levillain et al.⁽¹²⁰⁾ The radical concentration calculated for each TEGDME solution is plotted in Figure 4.7 as a function of sulfur concentration (C_S), and x_{mix} .

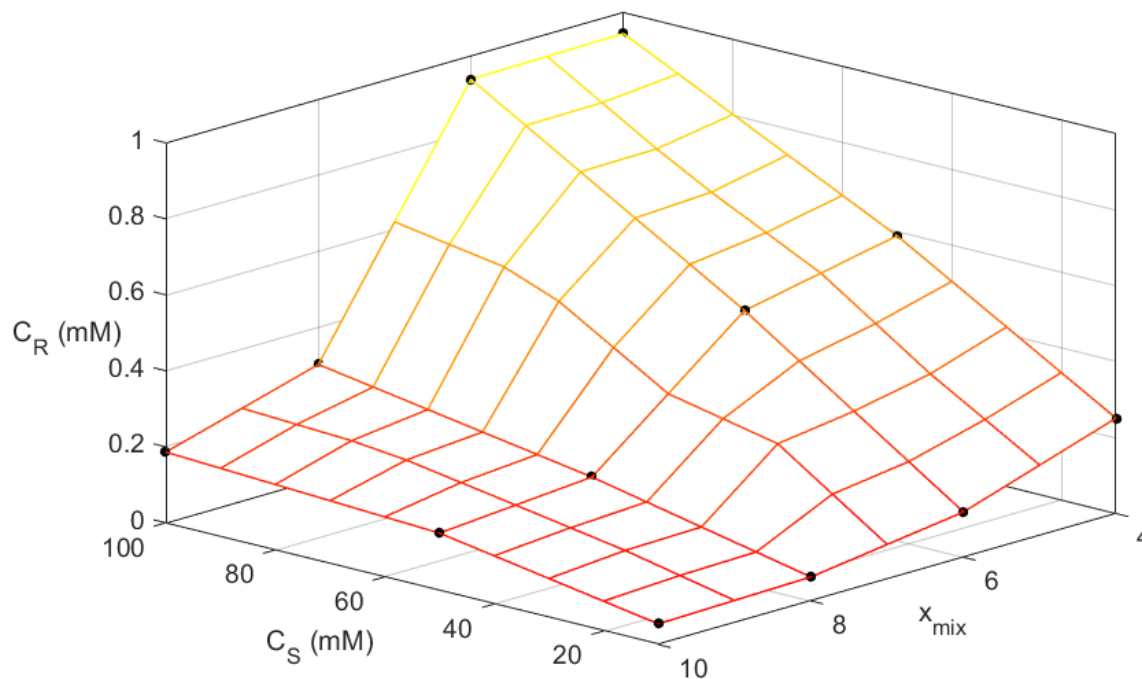


Figure 4.7 Polysulfide radical anion concentrations (C_R) determined by applying the Beer-Lambert law to the 617 nm peak of the TEGDME UV-vis spectra. Radical concentration is plotted against C_S , the concentration of atomic sulfur, and x_{mix} ($\text{Li}_2\text{S}_{x_{\text{mix}}}$). Data points for polysulfide solutions are shown as black circles, the surface-mesh was calculated via linear interpolation. Yellow indicates a high concentration of radical species; red denotes a low concentration of radical species.

Figure 4.7 shows that polysulfide radical concentration is a complex function of C_S and x_{mix} . In general, radical concentration increases with C_S , but the increase is dramatic for low values of x_{mix} (e.g. $x_{\text{mix}} = 4$). At constant C_S , radical concentration (C_R) is a sigmoidal function of x_{mix} , increasing rapidly in the vicinity of $x_{\text{mix}} = 7$. The fact that radical concentration increases with sulfur concentration is not surprising. One can use these data to elucidate the fraction of sulfur present as radical species in these solutions, f . In order to do this, one needs information about the distribution of radical anions in solutions. While conclusive identification of the radical species present in the TEGDME solutions will be a focus of future work, we calculate f assuming that the radical species were present in the form of LiS_3 . This assumption is supported by the similarity of the EPR g -factors obtained for the TEGDME solutions and those previously obtained for LiS_3 . One may thus view f as a crude estimate of the fraction of sulfur atoms in radical form.

$$f = \frac{C_R \cdot 3}{C_S} \quad (4.3)$$

This fraction, f , calculated according to equation (4.3), is plotted in Figure 4.8 as a function of sulfur concentration (C_S), and x_{mix} .

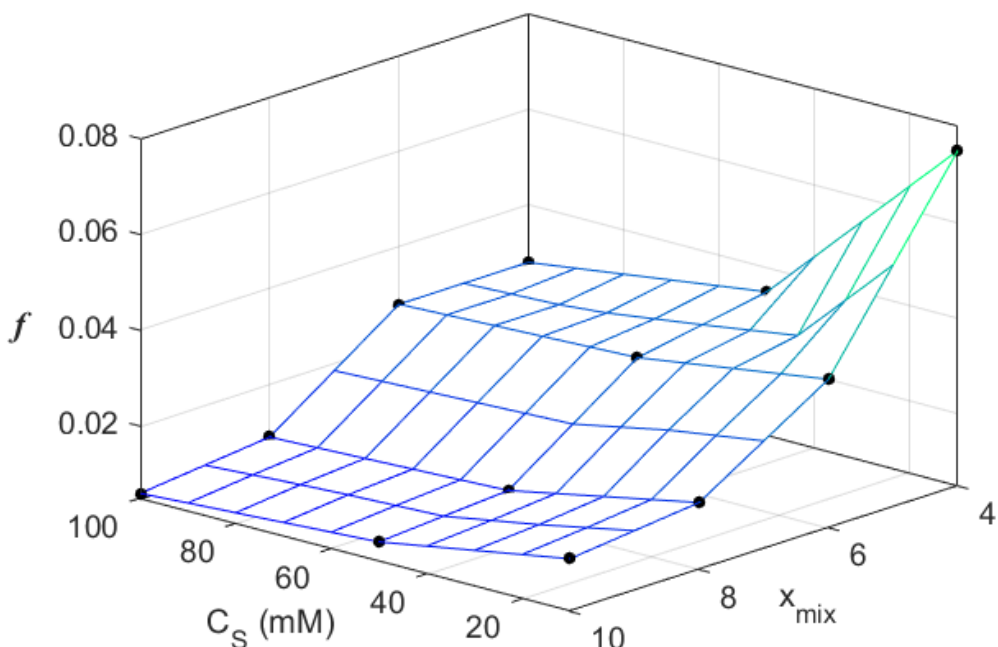


Figure 4.8 The estimated fraction of sulfur present as radical species (f) in TEGDME plotted against C_S , the concentration of atomic sulfur, and x_{mix} ($\text{Li}_2\text{S}_{x_{\text{mix}}}$). Data points for polysulfide solutions are shown as black circles, the surface-mesh was calculated via linear interpolation. Green indicates the highest fraction of radical species, while blue/purple denotes a lower fraction of radical species.

The values of f lie between 0.005 and 0.080 depending on the sulfur concentration and lithium to sulfur ratio. The radical fraction, f , is highest at low values of x_{mix} and low sulfur concentrations. The physiochemical properties of lithium polysulfide solutions will depend on both C_R and f ; solutions with large f have low values of C_R . The increase of f with decreasing C_S is consistent with what has previously been observed in DMF solutions, and is evidence of the dianion:radical anion dissociation equilibrium.⁽⁸⁾ Radical species are favored at low concentrations, while recombination of radicals to form dianion polysulfides is favored at higher sulfur concentrations.

4.4 Conclusions

We conclude that polysulfide radical anions are present in ether-based solvents, TEGDME and PEO. This conclusion is based both on UV-vis and EPR spectroscopy. We demonstrate quantitative relationships between the UV-vis and EPR signals in our solutions. We determine both the total radical concentration and fraction of sulfur in radical form. These parameters are complex functions of sulfur concentration and lithium to sulfur ratio, as shown in Figures 4.7 and 4.8. The fraction of radical species is high in dilute solutions and when the lithium to sulfur ratio is high.

4.5 Acknowledgements

This work was supported by the Assistant Secretary for Energy Efficiency and Renewable Energy, Office of Vehicle Technologies of the US Department of Energy under Contract DE-AC02-05CH11231 under the Battery Materials Research program. UV-vis spectroscopy was performed under a User Project at The Molecular Foundry. The authors would like to thank Professor Jeffrey Reimer for enabling the EPR experiments and Eric Scott for his support and useful discussions regarding EPR.

4.6 Supporting Information

4.6.1 UV-vis Spectra Peak Fitting and Parameters

UV-vis spectra obtained for polysulfide solutions were fit using a series of Gaussian functions in Igor Pro's MultipeakFit peak fitting program. An example of the peak fitting is shown below in Figure 4.S1, where the raw spectrum of the TEGDME, $x_{\text{mix}} = 4$, 50 mM sample is plotted along with the calculated fit and the individual Gaussian functions comprising the fit

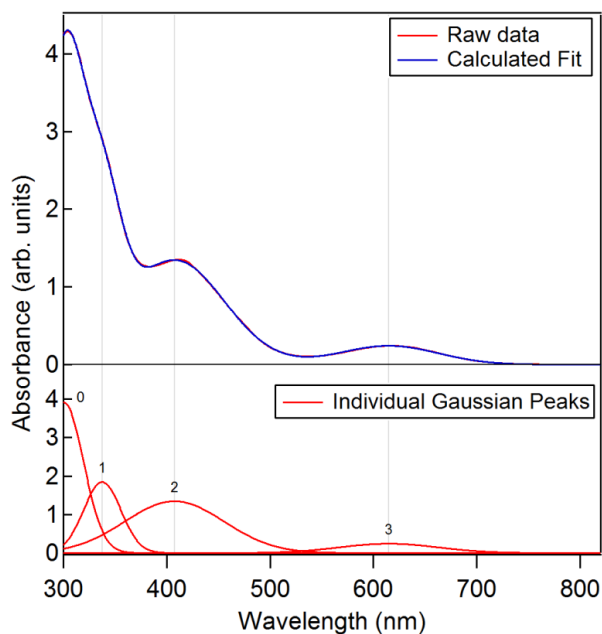


Figure 4.S1 Peak fitting for the TEGDME, $x_{\text{mix}} = 4$, $C_S = 50$ mM UV-vis spectrum

The parameters pertaining to each solution's UV-vis spectrum are shown in Tables 4.S1-S15 below.

Table 4.S1 UV-vis peak fitting parameters for TEGDME $x_{\text{mix}} = 4$, $C_S = 10$ mM

TEGDME $x_{\text{mix}} = 4$, $C_S = 10$ mM			
	Location	Amplitude	Area
Peak 0	297.93	0.77	42.88
Peak 1	339.16	0.44	19.65
Peak 2	410.92	0.32	42.74
Peak 3	472.20	0.01	0.24
Peak 4	617.00	0.10	12.05

Table 4.S2 UV-vis peak fitting parameters for TEGDME $x_{\text{mix}} = 4$, $C_S = 50$ mM

TEGDME $x_{\text{mix}} = 4$, $C_S = 50$ mM			
	Location	Amplitude	Area
Peak 0	300.72	3.95	191.84
Peak 1	338.28	1.77	78.23
Peak 2	407.32	1.35	164.09
Peak 3	617.00	0.24	28.19

Table 4.S3 UV-vis peak fitting parameters for TEGDME $x_{\text{mix}} = 4$, $C_S = 100$ mM

TEGDME $x_{\text{mix}} = 4$, $C_S = 100$ mM			
	Location	Amplitude	Area
Peak 0	321.76	6.44	409.40
Peak 1	411.54	2.70	316.65
Peak 2	617.00	0.39	45.07

Table 4.S4 UV-vis peak fitting parameters for TEGDME $x_{\text{mix}} = 6$, $C_S = 10$ mM

TEGDME $x_{\text{mix}} = 6$, $C_S = 10$ mM			
	Location	Amplitude	Area
Peak 0	291.01	0.48	24.28
Peak 1	337.24	0.32	14.91

Peak 2	334.99	0.22	54.49
Peak 3	442.37	0.13	13.52
Peak 4	617.00	0.05	6.04

Table 4.S5 UV-vis peak fitting parameters for TEGDME $x_{\text{mix}} = 6$, $C_S = 50$ mM

TEGDME $x_{\text{mix}} = 6$, $C_S = 50$ mM			
	Location	Amplitude	Area
Peak 0	292.43	3.85	216.60
Peak 1	335.76	2.30	128.79
Peak 2	418.34	1.50	218.79
Peak 3	617.00	0.21	24.52

Table 4.S6 UV-vis peak fitting parameters for TEGDME $x_{\text{mix}} = 6$, $C_S = 100$ mM

TEGDME $x_{\text{mix}} = 6$, $C_S = 100$ mM			
	Location	Amplitude	Area
Peak 0	345.13	3.65	175.41
Peak 1	417.63	3.24	455.74
Peak 2	617.00	0.39	45.09

Table 4.S7 UV-vis peak fitting parameters for TEGDME $x_{\text{mix}} = 8$, $C_S = 10$ mM

TEGDME $x_{\text{mix}} = 8$, $C_S = 10$ mM			
	Location	Amplitude	Area
Peak 0	275.30	0.69	55.44
Peak 1	337.99	0.24	12.72
Peak 2	418.26	0.20	29.60
Peak 3	617.00	0.03	3.45

Table 4.S8 UV-vis peak fitting parameters for TEGDME $x_{\text{mix}} = 8$, $C_S = 50$ mM

TEGDME $x_{\text{mix}} = 8$, $C_S = 50$ mM			
	Location	Amplitude	Area
Peak 0	283.30	3.96	326.05
Peak 1	341.47	1.07	59.53
Peak 2	405.33	1.25	264.77
Peak 3	617.00	0.08	8.95

Table 4.S9 UV-vis peak fitting parameters for TEGDME $x_{\text{mix}} = 8$, $C_S = 100$ mM

TEGDME $x_{\text{mix}} = 8$, $C_S = 100$ mM			
	Location	Amplitude	Area
Peak 0	268.74	11.93	1901.30
Peak 1	440.64	0.71	54.73
Peak 2	457.16	1.72	342.99
Peak 3	617.00	0.12	15.67

Table 4.S10 UV-vis peak fitting parameters for TEGDME $x_{\text{mix}} = 10$, $C_S = 10$ mM

TEGDME $x_{\text{mix}} = 10$, $C_S = 10$ mM			
	Location	Amplitude	Area
Peak 0	278.26	0.67	50.54
Peak 1	337.39	0.23	12.45
Peak 2	416.51	0.18	27.42
Peak 3	617.00	0.02	2.64

Table 4.S11 UV-vis peak fitting parameters for TEGDME $x_{\text{mix}} = 10$, $C_S = 50$ mM

TEGDME $x_{\text{mix}} = 10$, $C_S = 50$ mM			
	Location	Amplitude	Area
Peak 0	259.19	4.61	833.28
Peak 1	442.92	0.45	37.09
Peak 2	482.41	0.46	80.51
Peak 3	617.00	0.06	7.29

Table 4.S12 UV-vis peak fitting parameters for TEGDME $x_{\text{mix}} = 10$, $C_S = 100$ mM

TEGDME $x_{\text{mix}} = 10$, $C_S = 100$ mM			
	Location	Amplitude	Area
Peak 0	255.63	11.81	2102.40
Peak 1	444.38	0.52	38.15
Peak 2	464.25	1.56	313.01
Peak 3	617.00	0.08	9.98

Table 4.S13 UV-vis peak fitting parameters for PEO $x_{\text{mix}} = 4$, $C_S = 10$ mM

PEO $x_{\text{mix}} = 4$, $C_S = 10$ mM			
	Location	Amplitude	Area
Peak 0	305.33	0.75	68.44
Peak 1	345.67	0.42	13.79
Peak 2	428.60	0.26	34.66

Peak 3	617.00	0.06	7.38
--------	--------	------	------

Table 4.S14 UV-vis peak fitting parameters for PEO $x_{\text{mix}} = 6$, $C_S = 10$ mM

PEO $x_{\text{mix}} = 6$, $C_S = 10$ mM			
	Location	Amplitude	Area
Peak 0	299.13	0.56	53.20
Peak 1	344.48	0.20	6.87
Peak 2	425.35	0.17	22.55
Peak 3	617.00	0.03	3.94

Table 4.S15 UV-vis peak fitting parameters for PEO $x_{\text{mix}} = 8$, $C_S = 10$ mM

PEO $x_{\text{mix}} = 8$, $C_S = 10$ mM			
	Location	Amplitude	Area
Peak 0	296.63	0.41	18.07
Peak 1	336.83	0.35	17.93
Peak 2	416.55	0.14	19.78
Peak 3	617.00	0.02	2.71

4.6.2 EPR Spectra Fitting and Parameters

EPR spectra were fit using a first derivative Tsallian function as described by Weir et al. and shown in Equation 4.S1:

$$y = a \frac{(2^{(b-1)} - 1)}{(b-1)} \frac{2}{d^2} (x - c) \left[1 + (2^{b-1} - 1) \left(\frac{x-c}{2d} \right)^2 \right]^{\frac{(-b)}{(b-1)}} \quad (\text{Equation 4.S1})$$

Here, four parameters (a , b , c , and d) were fit for each spectrum. The spectra were fit using Igor Pro's Curve Fitting program. An example fitting is shown in Figure 4.S2, for the TEGDME, $x_{\text{mix}} = 6$, 100 mM spectrum.

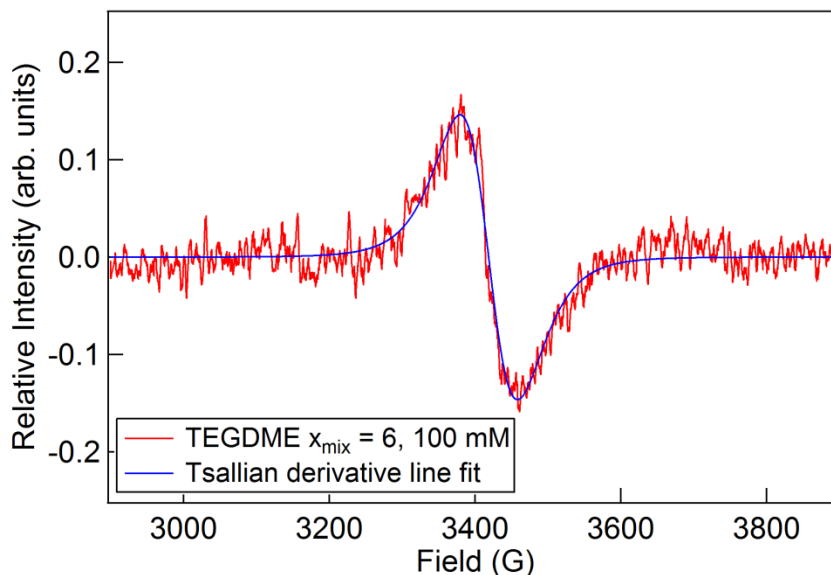


Figure 4.S2: Peak fitting for the TEGDME, $x_{\text{mix}} = 6$, $C_S = 100$ mM EPR spectrum

After fitting the EPR spectra with the Tsallian first derivative line functions, the fits were then integrated using Igor Pro's built-in Integration function (using a trapezoidal integration algorithm). The areas of the resulting integrated Tsallian curves were then obtained using Igor Pro's "areaxy" code. The g-factors (g) for each solution were obtained using equation 4.S2:

$$g = \frac{B\mu_B}{h\nu} \quad (\text{Equation 4.S2})$$

Here, h represents Planck's constant; ν is the microwave frequency of the given EPR experiment; B is the center of the EPR spectrum (the field strength at which the EPR spectrum intersects $y = 0$), which for each spectrum was parameter c determined from fitting of equation 4.S1 above; and μ_B the Bohr magneton.

The fitting parameters, g-factors, and integrated areas for each EPR spectrum are shown below in Tables 4.S16 and 4.S17.

Table 4.S16 EPR peak fitting parameters for TEGDME polysulfide solutions

TEGDME EPR Spectra Fit Parameters										
x_{mix}	C_S	a	\pm	b	\pm	c	\pm	d	\pm	g-factor
4	10	0.91	0.01	1.68	0.06	3424.3	0.35	25.9	0.4	2.0280
	50	1.52	0.01	1.35	0.03	3420.5	0.23	26.55	0.2	2.0298
	100	3.18	0.02	1.59	0.02	3420.3	0.12	27.76	0.13	2.0307
	300	6.18	0.02	1.49	0.01	3420.1	0.08	27.81	0.08	2.0302
6	10	0.22	0.01	1	0	3435.1	0.08	15.77	0	2.0221
	50	1.47	0.01	1.34	0.03	3422.4	0.23	26.66	0.19	2.0294

	100	2.96	0.02	1.39	0.02	3418.7	0.14	27.26	0.13	2.0305
	300	7.24	0.02	1.8	0.01	3418.9	0.07	29.84	0.09	2.0308
8	10	0.18	0.01	1.21	0.16	3438.4	0.97	16.74	0.7	2.0203
	50	0.52	0	1	0	3425.8	0.03	22.46	0	2.0274
	100	1.39	0.02	1.37	0.03	3421.1	0.26	25.6	0.22	2.0302
	300	3.35	0.02	1.69	0.02	3420.7	0.13	26.41	0.15	2.0298
10	10	0.13	0.01	1.01	0.15	3442	1	14.62	0.61	2.0176
	50	0.56	0.05	1	0	3424.3	0.04	21.43	0.86	2.0280
	100	0.97	0.01	1.18	0.04	3423.2	0.34	24.7	0.24	2.0288
	300	2.67	0.02	1.52	0.02	3419.6	0.16	26.29	0.16	2.0299

Table 4.S17 EPR peak fitting parameters for PEO polysulfide solutions

PEO EPR Spectra Fit Parameters										
x_{mix}	C_s	a	±	b	±	c	±	d	±	g-factor
4	10	0.62	0.01	1.43	0.06	3421.7	0.3	17.03	0.27	2.0315
	300	7.98	0.02	2	0.01	3418.4	0.03	19.99	0.05	2.0318
6	10	0.27	0.01	1	0.07	3423.6	0.55	15.32	0.36	2.0289
	300	1.6	0.02	2	0.04	3414.1	0.14	18.11	0.22	2.0327
8	10	0.126	0.01	1.56	0.27	3413.2	0.74	10.98	0.76	2.0351
	300	1.03	0.01	1.8	0.05	3413	0.17	16.7	0.22	2.0340

Chapter 5 – In situ X-ray absorption spectroscopy studies of discharge reactions in a thick cathode of a lithium sulfur battery[†]

ABSTRACT

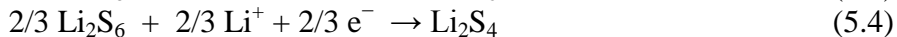
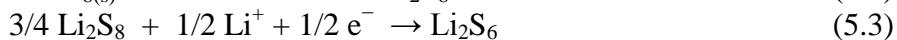
Lithium sulfur (Li-S) batteries are well known for their high theoretical specific capacities, but are plagued with scientific obstacles that make practical implementation of the technology impossible. The success of Li-S batteries will likely necessitate the use of thick sulfur cathodes that enable high specific energy densities. However, little is known about the fundamental reaction mechanisms and chemical processes that take place in thick cathodes, as most research has focused on studying thinner cathodes that enable high performance. In this work, in situ X-ray absorption spectroscopy at the sulfur K-edge is used to examine the back of a 115 μm thick Li-S cathode during discharge. Our results show that in such systems, where electrochemical reactions between sulfur and lithium are likely to proceed preferentially toward the front of the cathode, lithium polysulfide dianions formed in this region diffuse to the back of the cathode during discharge. We show that high conversion of elemental sulfur is achieved by chemical reactions between elemental sulfur and polysulfide dianions of intermediate chain length (Li_2S_x , $4 \leq x \leq 6$). Our work suggests that controlling the formation and diffusion of intermediate chain length polysulfide dianions is crucial for insuring full utilization of thick sulfur cathodes.

5.1 Introduction

Lithium sulfur batteries have become a widely popular focus of energy storage research due to their high theoretical specific capacity of 1672 mA-h/g.^(1, 2) The overall reaction mechanism that governs the Li-S discharge processes is given by:



The actual reaction mechanism involves a series of electrochemical reactions with lithium polysulfide reaction intermediates (Li_2S_x , $2 \leq x \leq 8$, referred to as polysulfide dianions; or LiS_x , $3 \leq x \leq 5$, referred to as polysulfide radical anions).^(8, 9, 31, 32, 42, 115) One example of an electrochemical reaction pathway is:



A decrease in the chain length of polysulfides is thus an unambiguous signature of electrochemical reactions. However, polysulfides are also known to undergo chemical reactions,

[†]This work has been submitted to *J. Electrochem. Soc.*

for example⁽¹³²⁾:



The evolution of polysulfide chain length in the presence of both electrochemical and chemical reactions is difficult to predict.

Lithium polysulfides tend to dissolve into the electrolyte, resulting in loss of cell capacity. It is thus not surprising that a great deal of research focuses on solving the issues related to polysulfide dissolution.^(7, 10, 60, 133) Many researchers have recognized that in order for Li-S cells to have high specific energy density and be competitive in cost with current lithium ion battery technology, Li-S cell cathodes must have high area-specific sulfur loadings.⁽¹³⁴⁻¹³⁶⁾ These high sulfur loadings can only be achieved by making the Li-S cell cathodes thicker. Hagen and Cheon et al. have shown that increasing cathode thickness leads to significant drops in cell capacity, as additional scientific challenges are introduced.^(136, 137) Increasing cathode thickness amplifies concentration polarization effects and plating of Li₂S (and possibly Li₂S₂) at the front of the electrode.⁽¹³⁷⁾ These problems are magnified if the battery is cycled at high rates of charge and discharge.

Despite their apparent importance, little is known about the chemical and electrochemical reactions that take place in thick sulfur cathodes. The purpose of this paper is to shed light on these reactions. In particular, we focus on chemical/electrochemical processes that take place at the back of thick sulfur cathodes. This is accomplished by in situ X-ray absorption spectroscopy (XAS).

X-ray absorption spectroscopy at the sulfur K-edge has become a popular technique for studying Li-S battery chemistry.^(18, 30, 55, 69, 93-95, 115, 126, 127, 138) XAS is element-specific and capable of detecting species that are amorphous or crystalline, dilute or concentrated. It also allows researchers to probe Li-S cells without any deconstruction of the cell itself. Interpretation of XAS data from Li-S cells is challenging due to the lack of spectral standards for the polysulfide species.^(24, 28, 30) However, we have recently shown that the X-ray absorption spectra for lithium polysulfide molecules can be calculated from first principles, thus enabling unambiguous interpretation of experimentally obtained X-ray spectra.^(54, 55)

In this work, in situ X-ray absorption spectroscopy at the sulfur K-edge is used to examine an Li-S cell cathode during discharge. The low energy of sulfur K-edge X-rays, and the presence of sulfur in the cathode (which absorbs sulfur K-edge X-rays) limited the penetration of X-rays into the cathode. Thus, our data reflects the products of chemical and electrochemical reactions that occur at the back of the thick cathode.

5.2 Experimental

5.2.1 Electrolyte Preparation

All electrolyte, cathode, and cell preparation was performed in an argon-filled glovebox (MBraun). Electrolyte films were prepared using a diblock copolymer of polystyrene-poly(ethylene oxide) (SEO) purchased from Polymer Source Inc., having polystyrene and poly(ethylene oxide) molecular weights of 165 kg/mol and 205 kg/mol, respectively. Lithium perchlorate (LiClO₄) (Sigma-Aldrich) was dried for 24 hours under vacuum at 90 °C before use. SEO and LiClO₄ were added to n-methylpyrrolidone (NMP) (EMD Millipore) in an amount equivalent to 11 wt% solids, and allowed to mix overnight at 90 °C. The solution was then cast

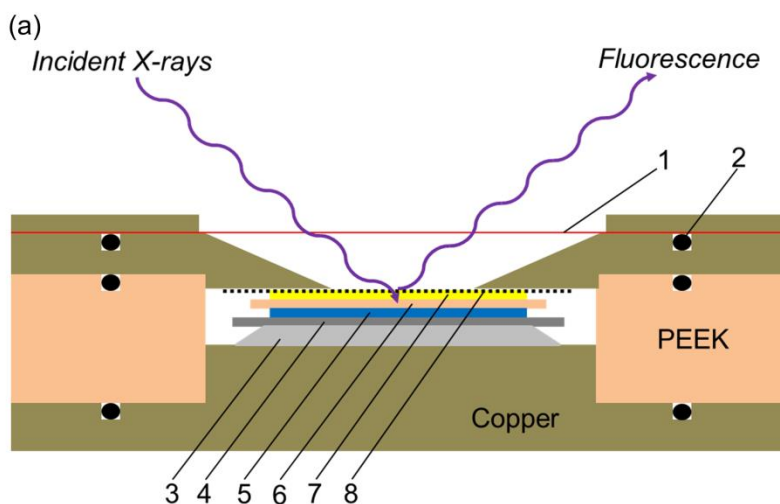
onto nickel foil using a doctor blade and allowed to dry at 60 °C overnight. The resulting film was peeled from the nickel foil and dried under vacuum at 90 °C overnight. The dry film composition had a LiClO₄ amount equivalent to an ‘r’ value of $r = 0.085$, where ‘r’ is the ratio of lithium ions per ethylene oxide monomer.

5.2.2 Cathode Preparation

Cathode slurries contained S₈ (Alfa Aesar), carbon black (Denka), LiClO₄, and SEO (identical to that which was used in the electrolyte separator) mixed in NMP, such that the slurry was 15 wt% solids. The slurry was mixed overnight at 90°C and subsequently mixed using a homogenizer (Polytron) set to 15,000 RPM. Homogenization was performed three times, five minutes each time with five minute breaks in between each homogenization to prevent the solution from heating up past undesirable temperatures. The resulting slurry was then poured into a clean Teflon petri dish that was placed on a hot plate at 60 °C. The slurry was routinely spread along the bottom of the petri dish using a clean spatula every 30 minutes for 4 hours until the cast slurry was dry enough that it no longer dewet the Teflon surface. The temperature of the hot plate was then set to 50 °C and the film was allowed to dry overnight. The film was then peeled from the petri dish and dried overnight under vacuum at 50°C. The dry composition of all cathodes used in the study was 13.0 wt% S₈, 50.7% SEO, 6.2% LiClO₄ and 30.0% carbon.

5.2.3 In situ XAS cell

In situ X-ray absorption spectroscopy was performed using a custom designed cell that enabled X-rays to probe the cathode during charge/discharge. Figure 5.1a shows the cell schematic along with the corresponding identity for all of its components. Figure 5.1b shows an image of the in situ cell.



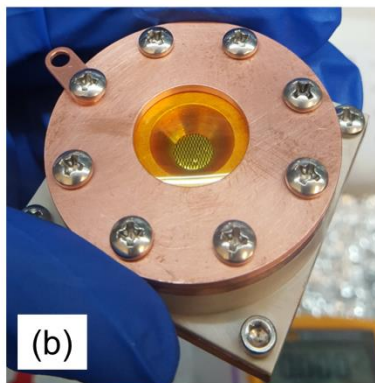


Figure 5.1 (a) Schematic of cell housing used for in situ XAS experiments: (1) Ultrathin Kapton film (8 μ m thick), (2) O-ring, (3) stainless steel spring, (4) stainless steel shim, (5) lithium metal anode, (6) SEO/LiClO₄ electrolyte separator, (7) sulfur cathode (elemental sulfur, carbon black, SEO, LiClO₄), (8) electronic grade aluminum mesh. (b) Image of in situ XAS cell

A circular piece of the free-standing cathode film was punched at a diameter of 7/16". The thickness of the disc was measured using a micrometer, and determined to initially be $130 \pm 10 \mu\text{m}$. The disc was then placed between two fluorinated ethylene propylene (FEP) sheets and pressed for 30 seconds using a hand press at room temperature. The film thickness was then measured again and determined to be $115 \pm 5 \mu\text{m}$. An electrolyte disc was then cut from the electrolyte film described above, at a diameter of 9/16". The cathode disc was then gently pressed to the punched electrolyte disc, placed between two (FEP) sheets and pressed for 30 seconds using a hand press at room temperature. The electrolyte disc used in this experiment had a thickness of $35 \mu\text{m}$.

Lithium metal chips (MTI), having a thickness of $250 \mu\text{m}$ were used as the anode material and were further punched to be 7/16" in diameter. To assemble the cell, the lithium metal chip was placed on a stainless steel shim (component #4 in Figure 5.1). The shim had a ring of Kapton tape placed around the edges that had an inner diameter of 8/16", and an outer diameter equal to the diameter of the shim. This tape ring assured that the lithium metal would stay in place during cell assembly and prevented any unwanted contact between the positive and negative electrodes.

After the lithium was pressed to the stainless steel shim, the electrolyte/cathode assembly was then placed on top of the lithium metal. A circular piece of $55 \mu\text{m}$ thick aluminum mesh (MTI), punched to a diameter of 7/16" was then placed on top of the cathode film. This assembly was then placed inside the cell housing as shown in Figure 5.1. The cell was fastened down to insure contact between the lithium metal, electrolyte separator, cathode, and aluminum mesh interfaces. The O-rings shown in Figure 5.1a assured that the cell was air-tight. The ultrathin Kapton film (8 μm thick) (Fralock) allowed X-ray photons to enter and leave the cell while also preventing air exposure of the Li-S cell inside.

5.2.4 Battery Cycling

The Li-S cell was held at a temperature of $80 \text{ }^\circ\text{C}$ for 8 hours before discharge, and discharged at $80 \text{ }^\circ\text{C}$ while X-rays probed the cathode. Discharge was performed using a VMP3

Potentiostat (Bio-Logic). The cell was discharged at a rate of C/80, calculated using the measured mass of the cathode electrode, the known weight percent of sulfur in the cathode, and assuming a theoretical capacity of 1672 mA-h/g for sulfur. Discharge was stopped at 1.50 V.

5.2.5 Experimental X-ray Absorption Spectroscopy Measurements

XAS measurements were performed at beamline 4-3 of the Stanford Synchrotron Radiation Lightsource. Preliminary XAS experiments were performed at beamline 9.3.1 of the Advanced Light Source (Lawrence Berkeley National Laboratory). Measurements were taken in fluorescence mode using a four element Vortex detector, with 0.1 eV energy resolution around the absorption K-edge. One scan took roughly 8 minutes to collect, equivalent to roughly 2.75 mA-h/g of capacity was passed per scan. The beam spot size was 5 mm² and was not moved during discharge. The Li-S cell was measured in a helium-filled chamber, and was placed on a custom-made heating stage equipped with a PID temperature controller. Calibration of the X-ray energy was performed using sodium thiosulfate (Sigma-Aldrich), setting the first peak maximum to 2472.02 eV.

5.2.6 Data Analysis

Data was normalized and background subtracted using Athena⁽¹³⁹⁾. Least squares fitting of the experimental spectra with the theoretical spectra was performed using a least squares fitting program created by Matthew Marcus at the Advanced Light Source. The theoretical spectra used to analyze the data were those presented by Pascal et al. in a previous publication.⁽⁵⁵⁾ In our previous work, least squares fitting of the experimental spectra with theoretical spectra was only performed up to an X-ray energy of 2474.5 eV.⁽¹¹⁵⁾ This was done, in part, because above ~2473.0 eV, the original theoretical spectra lack absorption intensity compared to the experimental spectra. Obtaining accurate absorption intensities in this region would require a significant amount of computational resources. To correct for this difference in intensity, and allow fitting of the theoretical and experimental spectra to be performed at all energies, an arctangent step function was added to the theoretical spectra to account for the lack of intensity above the main edge. To determine the parameters of the arctangent function added to the theoretical spectra, an arctangent function was added to the theoretical spectrum of S₈, and its parameters regressed until the theoretical spectrum matched the known experimental spectrum. The arctangent function was centered at 2473.0 eV, had a height of 0.40 (arb. units) and a width of 0.20 eV. We note that because the arctangent step function was centered at 2473.0 eV, its addition has little effect on the main-edge and pre-edge intensities, areas, and ratio.

5.3 Results

We begin our analysis by examining the schematic of the cell used for the XAS measurements, shown in Figure 5.2. The Li-S cell probed in this study consisted of a lithium metal anode, a block copolymer electrolyte separator of SEO with LiClO₄, and a cathode that contained elemental sulfur, carbon black, SEO, and LiClO₄. X-rays entered the cell through an aluminum mesh current collector on the back of the cathode. The cathode used in this experiment had a thickness of 115 μm. At this thickness, and given that the experiments were

carried out at the sulfur K-edge, it is expected that X-ray photons do not probe the entire cathode thickness. To gain an accurate understanding as to what depth of the cathode incident X-rays did probe, the X-ray transmission to a variety of depths within the cathode was calculated using the known cathode composition and atomic absorption coefficients (see Supporting Information for details). The results of these calculations are summarized in Table 5.1, where we report the expected fraction of incident photons that are capable of penetrating to the reported depth in column 2. After incoming photons have taken part in the excitation of a core-shell electron, fluorescent photons, which have a lower energy than incident photons, must then emerge from within the cathode to arrive at the detector. Column 3 of Table 5.1 thus represents the fraction of photons emerging from a given depth. The detected signal depends on the product of the fractions given in columns 2 and 3. This enables estimation of the fraction of the XAS signal that can be attributed to each slice through the cathode. This fraction is given in column 4. It is evident from this calculation that the signal is dominated by sulfur species in the back of the cathode, about 30 μm from the current collector. The darkened region of the cathode in Figure 5.2 represents the portion of the cathode probed in this study.

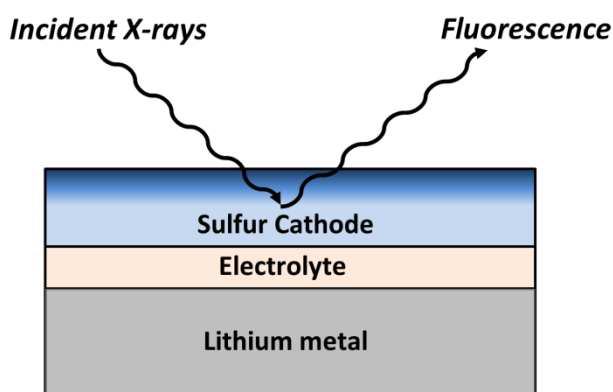


Figure 5.2 Simplified X-ray absorption spectroscopy experiment schematic. Darkened (upper) region of the cathode represents the thickness that was probed by X-rays.

Table 5.1 Depth of penetration analysis for the Li-S cathode based on the known cathode composition and X-ray absorption coefficients

Cathode depth (μm)	Fraction of incoming photons transmitted to given depth	Fraction of fluorescent photons emerging out of the cathode from a given depth	Fraction of XAS signal from a given slice
0	0.811	0.628	-
5	0.652	0.442	0.296
10	0.524	0.311	0.209
15	0.422	0.219	0.147
20	0.339	0.154	0.103
25	0.273	0.108	0.073
30	0.219	0.076	0.051

35	0.176	0.054	0.036
40	0.142	0.038	0.025
45	0.114	0.027	0.018
50	0.092	0.019	0.013
75	0.031	0.003	0.025
100	0.010	0.001	0.004
115	0.005	0.000	0.001

The Li-S cell was discharged at a constant rate of $C/80$ based on the sulfur loading. The voltage profile for the discharge process is shown in Figure 5.3. Here, cell capacity is represented by the variable Q . The overall capacity obtained for the cell was 252 mAh/g, which corresponds to 15.1% of the overall theoretical capacity of lithium sulfur batteries. Cheon et al. studied the effect of increasing cathode thickness on discharge capacity:⁽¹³⁷⁾ discharge capacities of 78.9%, 62.8%, and 53.1% of the theoretical capacity were obtained as cathode thickness was increased from 15, to 30, to 60 μm , using discharge rates that were roughly $C/25$, $C/50$ and $C/100$, respectively. Extrapolating the results of Cheon, we would expect the 115 μm thick cathode cell probed here to obtain only 22 % of the theoretical capacity, which is similar to that which was obtained here.

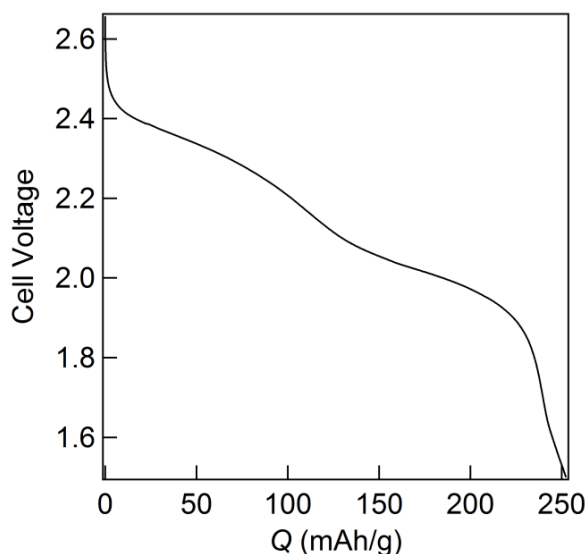


Figure 5.3 Cell voltage versus capacity (Q) obtained for the first discharge of the Li-S cell probed with X-ray's at a constant discharge rate corresponding to $C/80$.

The discharge profile reported in Figure 5.3 is qualitatively similar to that obtained by Cheon et al. in thick cathodes, and contains two regimes (sloping plateaus). Generally, the first plateau announces the formation of soluble polysulfides while the second plateau is taken as a signature of the formation of Li_2S . The extent to which this is true in thick cathodes remains to be established. It is important to note that the second plateau in our cells and the cells used by Cheon et al. is much shorter than that obtained in thin sulfur cathodes. Cheon et al. suggest that this is due to preferential plating of Li_2S at the front of the cathode, leading to pore blockage.

While phenomena that are occurring throughout the entire cathode are outside the scope of our experiment, it is likely that the 115 μm thick cathode used in this study discharges unevenly. Electrochemical reactions are more likely to occur at the front of the electrode than the back.

Figure 5.4 shows the sulfur K-edge X-ray absorption spectra obtained throughout discharge. The spectra are characterized by two peaks: one peak at 2472.6 eV, referred to as the main-edge peak due to its occurrence at the expected absorption edge of sulfur, and a second at roughly 2471.0 eV, referred to as the pre-edge peak due to its occurrence being just below the sulfur absorption edge.

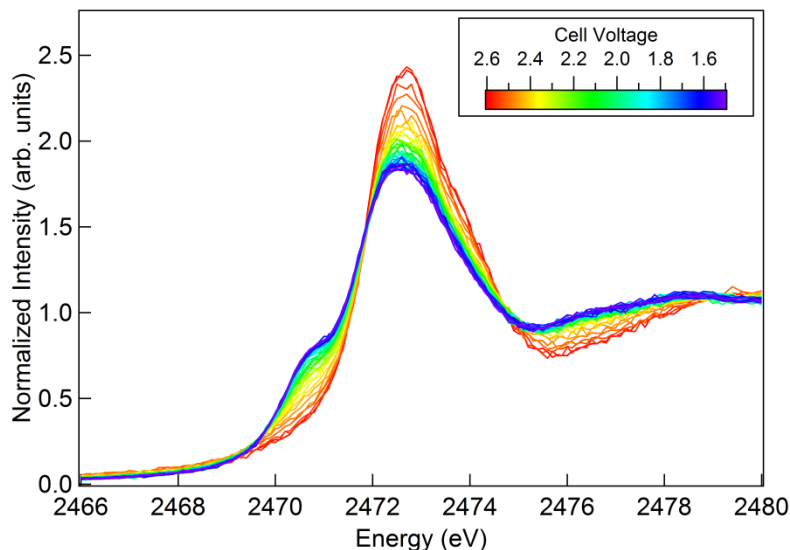


Figure 5.4 Sulfur K-edge X-ray absorption spectra obtained for the Li-S cell cathode during first discharge.

X-ray spectra of lithium polysulfides based on first principles calculations given by Pascal et al. are shown in Figure 5.5a.⁽⁵⁵⁾ The X-ray spectra of the reactant and expected final product, S_8 and Li_2S , are shown in Figure 5.5b. The spectrum of Li_2S is based on first principle calculations; the similarity of the theoretical Li_2S spectrum to the established experimental spectrum for Li_2S validates the methods used to calculate the spectra of lithium polysulfide dianion species.⁽⁵⁵⁾ The S_8 spectrum corresponds to that measured before the cell was discharged. (The S_8 spectrum in Figure 5.5b is qualitatively similar to the theoretical S_8 spectrum given in reference⁽⁵⁵⁾) We use the spectra in Figure 5.5 to interpret the experimental data presented in Figure 5.4.

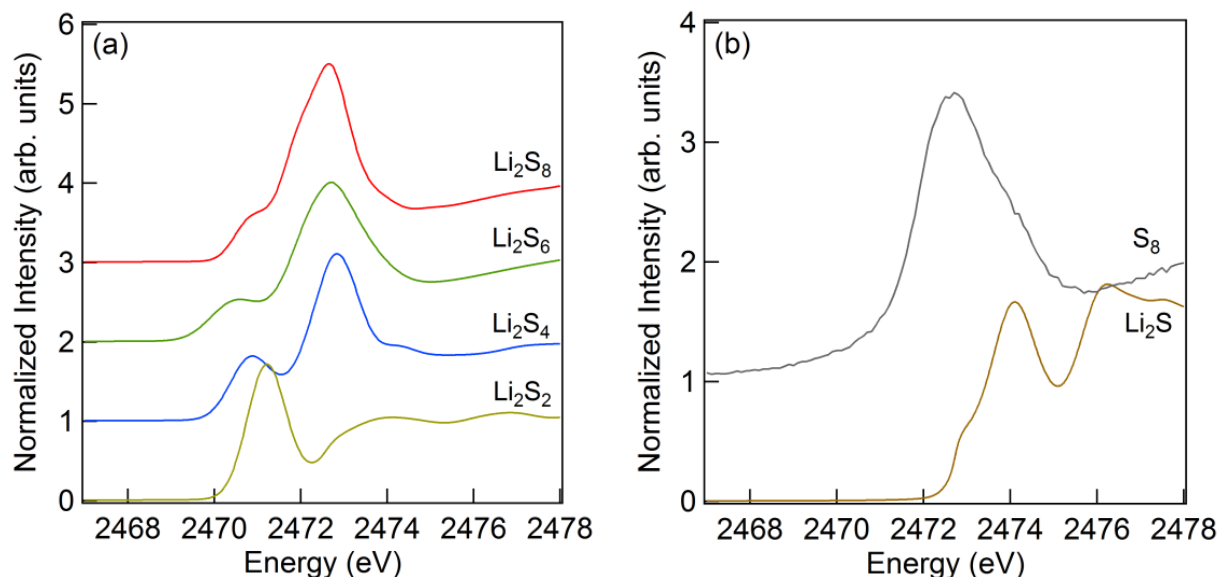


Figure 5.5 (a) Polysulfide dianion spectral standards, and (b) spectral standards for elemental sulfur and lithium sulfide used to analyze the experimental X-ray spectra.

First principles calculations indicate that the pre-edge peak is the signature of X-ray excitations of the charged terminal sulfur ions, while the main-edge peak is related to the uncharged internal sulfur atoms of the polysulfide chain. Therefore, the main-edge to pre-edge peak area ratio reflects the relative population of these sulfur atom types in a given sample, and as such could be regarded as a proxy for the average polysulfide chain length, realizing that a given sample may comprise polysulfide molecules with a distribution of lengths.⁽⁵⁵⁾ The relationship between spectral features and average chain length is quantified in Figure 5.6a. It is evident from simulations of single polysulfide species that polysulfide chain length ‘x’ of a given polysulfide Li_2S_x is approximately a linear function of the area ratio. The equation corresponding to the least squares fit of the data is given in Figure 5.6a. We can think of this equation as a calibration for converting the XAS signal into a polysulfide chain length.

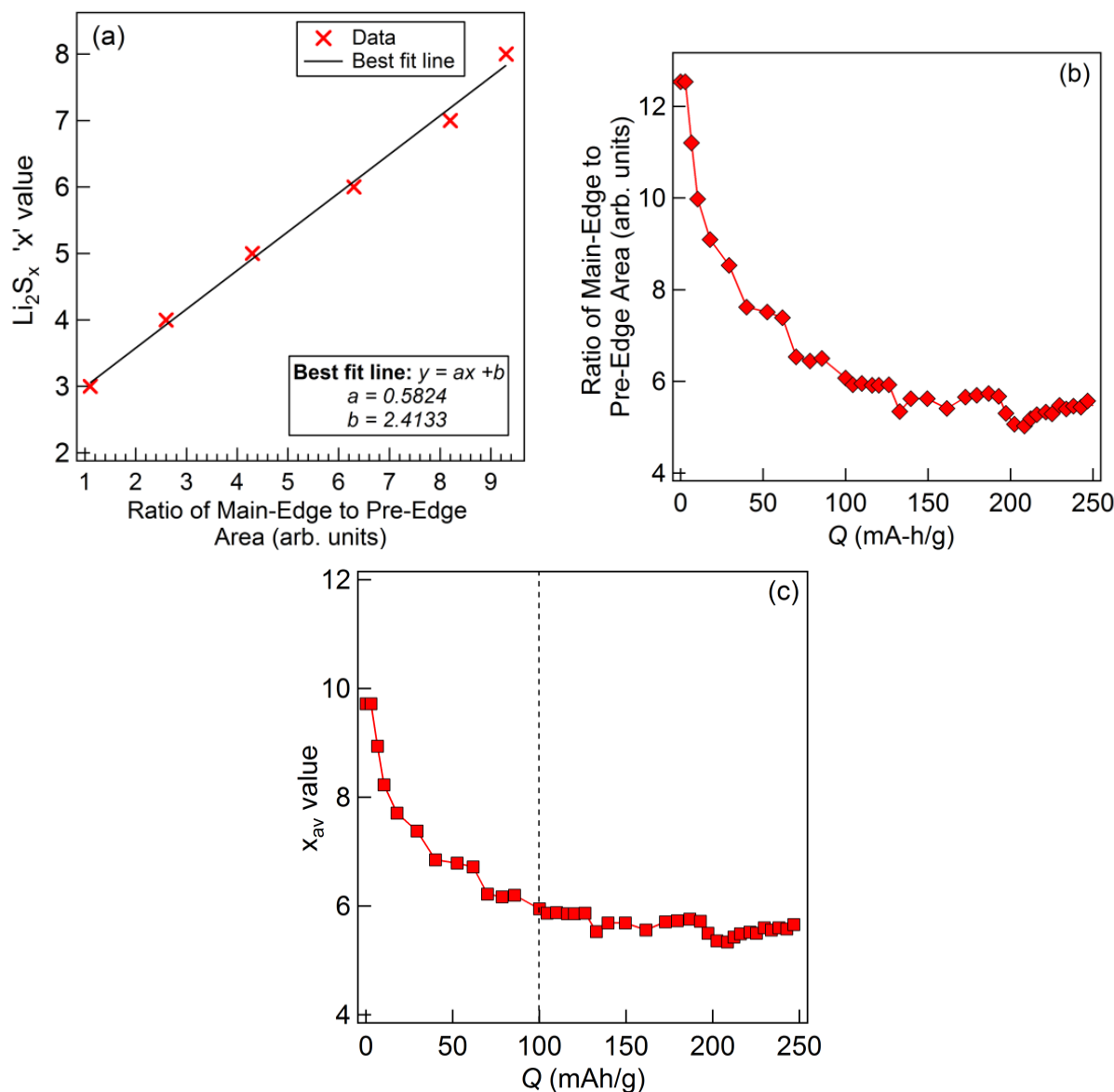


Figure 5.6 (a) Ratio of main-edge peak area to pre-edge peak area versus corresponding Li₂S_x 'x' value, derived from theoretical spectra as described by Pascal et al.,⁽⁵⁵⁾ (b) Ratio of main-edge peak area to pre-edge peak area based on fitting of the experimental spectra shown in Figure 5.4, (c) Average polysulfide chain length for representing the distribution of polysulfide dianion species present in the cathode as a function of capacity, calculated using the relationship shown in (a) and the ratios shown in (b)

The in situ X-ray spectra shown in Figure 5.4 were fit using two Gaussian peaks (one for the main edge peak and one for the pre-edge peak) and an arctangent function to represent the absorption edge's increase in intensity (see Supporting Information for more details). The resulting ratio of main-edge to pre-edge peak area was calculated for each scan and is shown in Figure 5.6b as a function of capacity. The expression given in Figure 5.6a was then used to calculate an approximate average polysulfide chain length, x_{av} . While our calibration expression was developed for single chemical species, we expect it to hold for mixtures because of the fact that we have established the origin of the pre-edge and main-edge features.⁽⁵⁵⁾ In principle, the

expected value of x_{av} at $t = 0$ is infinity, because lithium is not incorporated into any of the sulfur containing species. Our fitting procedure results in an x_{av} value of 9.72, because the main edge peak of the cathode at $t = 0$ is not perfectly Gaussian. If electrochemical reactions were taking place, then the value of x_{av} determined from XAS would decrease continuously with capacity. This is clearly not the case in Figure 5.6c. A decrease in x_{av} is detected in the range $0 \leq Q \leq 100$ mAh/g. In contrast, x_{av} is a weak function of capacity in the range $100 \leq Q \leq 252$ mAh/g, suggesting the absence of electrochemical reactions in this regime.

To further elucidate the chemical species formed during discharge, the X-ray spectra were fit using theoretical X-ray absorption spectra given in Figure 5.5a and 5.5b.⁽⁵⁵⁾ A least squares approach similar to that used in reference⁽¹¹⁵⁾ was used to fit the experimental spectra. The composition of the back of the cathode thus obtained is plotted as a function of capacity in Figure 5.7.

It is evident that no Li_2S is formed at the back of the cathode. Note that the formation of Li_2S is indicated by a peak at 2474.0 eV (Figure 5.5b). This feature is absent in the XAS spectra from our cell (Figure 5.4). In other words, the reduction of sulfur at the back of the cathode is far from complete. This is consistent with the findings of Cheon et al..⁽¹³⁷⁾

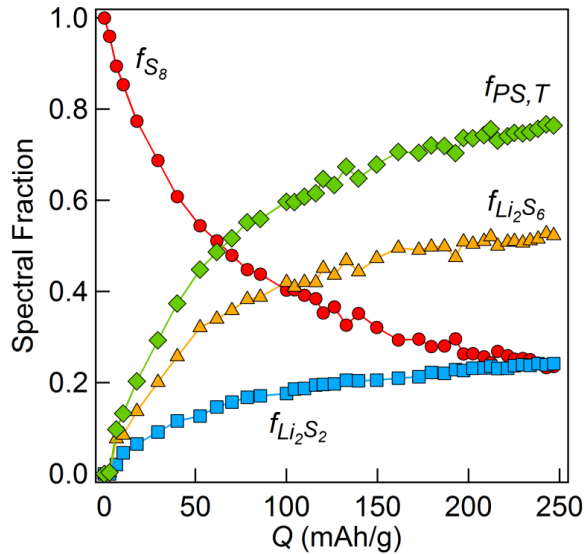


Figure 5.7 Composition of each in situ spectrum determined by least squares fitting of experimental X-ray spectra with theoretically calculated X-ray spectra as a function of capacity. Here, $f_{PS,T}$ refers to the spectral fraction of polysulfide dianions present, obtained by summing the spectral fractions $f_{\text{Li}_2\text{S}_2}$ and $f_{\text{Li}_2\text{S}_6}$, that have an average polysulfide dianion chain length of x_{avps} .

Figure 5.7 also shows that spectra were found to consist of a combination of S_8 , Li_2S_2 , and Li_2S_6 . For simplicity, we characterize the polysulfide dianion species using an average chain length for the polysulfide dianions, here referred to as x_{avps} and calculated as:

$$x_{avps} = \frac{(f_{\text{Li}_2\text{S}_2} \cdot 2) + (f_{\text{Li}_2\text{S}_6} \cdot 6)}{f_{\text{Li}_2\text{S}_2} + f_{\text{Li}_2\text{S}_6}} \quad (5.8)$$

Here, $f_{Li_2S_2}$ and $f_{Li_2S_6}$ are the spectral fractions of Li_2S_2 and Li_2S_6 for each experimental spectrum's fit, as shown in Figure 5.7.

Because the spectra were found to consist of only elemental sulfur and polysulfide dianions, the spectral fraction of sulfur (on an atomic basis) present in the form of polysulfide dianions ($f_{PS,T}$) can then be calculated using equation 5.9:

$$f_{PS,T} = 1 - f_{S_8} \quad (5.9)$$

The spectral fraction of polysulfide dianions ($f_{PS,T}$) is also plotted in Figure 5.7.

With that, the spectra shown in Figure 5.4 can be represented as a two component mixture of polysulfide dianions having an average chain length of $x_{av_{ps}}$, and present in a spectral fraction represented by $f_{PS,T}$, and elemental sulfur (S_8) represented by the spectral fraction f_{S_8} . The measured signal from a sulfur-containing molecule is proportional to the number of sulfur atoms in the molecule. Thus, the spectral fractions shown in Figure 5.7 are converted to mole fractions using equations 5.10 and 5.11:

$$y_{S_8} = \frac{\left(\frac{f_{S_8}}{8}\right)}{\left(\frac{f_{S_8}}{8}\right) + \left(\frac{f_{PS,T}}{x_{av_{ps}}}\right)} \quad (5.10)$$

$$y_{PS,T} = \frac{\left(\frac{f_{PS,T}}{x_{av_{ps}}}\right)}{\left(\frac{f_{S_8}}{8}\right) + \left(\frac{f_{PS,T}}{x_{av_{ps}}}\right)} \quad (5.11)$$

The mole fractions of S_8 and polysulfide dianions are referred to as y_{S_8} and $y_{PS,T}$, respectively. It is then convenient to determine the amount of lithium that has reacted with sulfur as a function of capacity, which we do in equation 5.12:

$$x_{av_{all}} = \frac{y_{S_8} \cdot 8 + y_{PS,T} \cdot x_{av_{ps}}}{y_{PS,T}} \quad (5.12)$$

Here, $x_{av_{all}}$ represents the expected polysulfide dianion chain length if all of the sulfur were to react with lithium to create a single polysulfide species with a chain of length $x_{av_{all}}$. The parameter $x_{av_{all}}$ is a hypothetical chain length that would be identical to x_{av} reported in Figure 5.6c if our analysis were perfect. The estimated chain length of the polysulfide species is $x_{av_{ps}}$. The values of $x_{av_{all}}$, as well as $x_{av_{ps}}$ are plotted as a function of capacity in Figure 5.8.

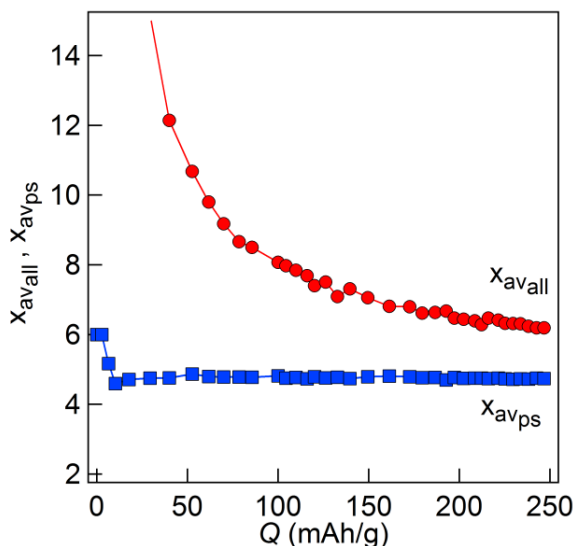


Figure 5.8 Ratio of lithium to sulfur represented in the stoichiometric form of a polysulfide dianion for the overall system and just the polysulfide dianion species

Examining Figure 5.8, we see that the value of x_{avall} drops rapidly at the beginning of discharge, signaling reactions between sulfur and lithium. If reduction were to go to completion, we would expect the value of x_{avall} to decrease at a consistent rate as a function of capacity. Instead, we see that the decrease in x_{avall} slows down, suggesting that transport of lithium to the back of the cathode is limited during later stages of discharge. Interestingly, x_{avps} remains nearly constant through most of the discharge process.

In principle, polysulfides obtained at the back of the cathode could be either produced by electrochemical reduction of sulfur at the back of the cathode or diffusion of polysulfides produced at the front of the cathode. To distinguish between these possibilities, we examined the total fluorescence intensity reaching the detector during each scan. This intensity is directly proportional to the concentration of sulfur atoms in the back of the cathode that is probed by XAS. For each scan, the fluorescence intensity was averaged over the energy range of 2490-2565 eV, where there are no absorption features. The averaged fluorescence intensity was then normalized by the incoming X-ray intensity measured during each scan. The normalized fluorescence intensity for the zeroth scan (prior to the start of discharge) is called I_0 , and the normalized intensity for the 'nth' scan is referred to as I_n . Plotting the ratio of I_n to I_0 as a function of capacity reveals the changes in sulfur content at the back of the cathode through the discharge process. If polysulfides were not diffusing into or out of the back of the cathode then I_n/I_0 would be constant. In Figure 5.9a we plot I_n/I_0 as a function of capacity. It is evident that I_n/I_0 increases as the cell is discharged. This indicates that polysulfides formed at the front of the cathode are diffusing into the back.

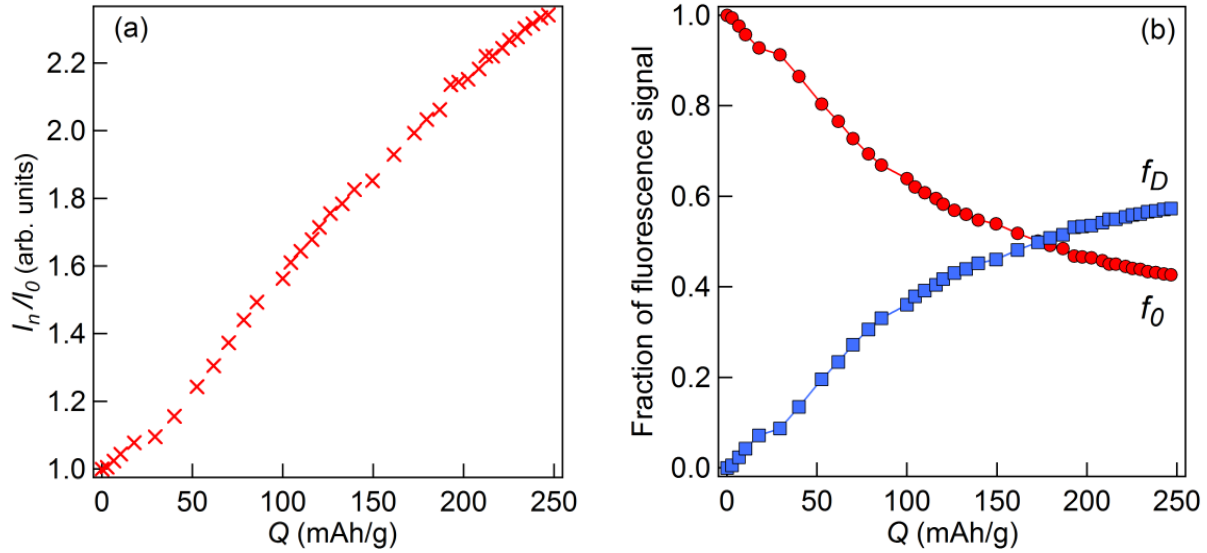


Figure 5.9 (a) Ratio of fluorescence intensity to initial fluorescence intensity measured before discharge as a function of capacity (I_n/I_0); (b) fraction of fluorescence signal pertaining to sulfur in the back of the cathode since the beginning of discharge (f_0) and fraction of sulfur diffused to the back of the cathode during discharge (f_D).

Changes in the sulfur content at the back of the cathode were quantified by noting that:

$$\frac{I_n}{I_0} = \frac{S_T}{S_0} \quad (5.13)$$

Here, S_0 represents the moles of sulfur atoms in the back of the cathode for the zeroth scan (obtained before discharge began), and S_T is the total moles of sulfur atoms in the back of the cathode for any scan thereafter. The amount of sulfur (on an atomic basis) that has diffused to the back of the cathode can then be determined through equation 5.14:

$$S_T - S_0 = S_D \quad (5.14)$$

Here, S_D represents the amount of sulfur (on an atomic basis) that has diffused to the back of the cathode during discharge. The fraction of sulfur that is present in the back of the cathode as a result of diffusion is given by f_D :

$$\frac{S_D}{S_T} = f_D \quad (5.15)$$

The fraction of sulfur (on an atomic basis) that corresponds to sulfur originally present in the back of the cathode since the beginning of discharge is then given by f_0 :

$$1 - f_D = f_0 \quad (5.16)$$

At the beginning of discharge, f_0 is equal to 1, because polysulfide diffusion has not begun. As discharge proceeds, f_0 decreases as polysulfide dianions diffuse to the back of the

cathode and f_D increases. The values of f_D and f_0 are plotted as a function of capacity in Figure 5.9b.

As a result of polysulfide diffusion to the back of the cathode, the spectral fraction of polysulfide dianions ($f_{PS,T}$) consists of two components: (1) polysulfide dianions that have diffused into the back of the cathode, and (2) polysulfide dianions that have been created in the back of the cathode. The spectral fraction of polysulfides present in the back of the cathode as a result of diffusion ($f_{PS,D}$) is equal to the spectral fraction of sulfur (on an atomic basis) present in the back of the cathode as a result of diffusion:

$$f_{PS,D} = f_D \quad (5.17)$$

The spectral fraction of polysulfide dianions created in the back of the cathode ($f_{PS,0}$) is then given by:

$$f_{PS,0} = f_{PS,T} - f_{PS,D} \quad (5.18)$$

The overall mole fraction of polysulfide dianions, $y_{PS,T}$, thus consists of a mole fraction of diffused polysulfide dianions ($y_{PS,D}$), and a mole fraction of polysulfide dianions created in the back of the cathode ($y_{PS,0}$), calculated through equations 5.19 and 5.20, respectively:

$$y_{PS,D} = \frac{\left(f_{PS,D} / x_{avps} \right)}{\left(f_{S_8/8} \right) + \left(f_{PS,T} / x_{avps} \right)} \quad (5.19)$$

$$y_{PS,0} = \frac{\left(f_{PS,0} / x_{avps} \right)}{\left(f_{S_8/8} \right) + \left(f_{PS,T} / x_{avps} \right)} \quad (5.20)$$

A second implication of the results shown in Figure 5.9a and 5.9b is that the measured fractions of elemental sulfur (f_{S_8} and y_{S_8}) are affected by diffusion of polysulfides from the front of the cathode. In order to determine the true spectral fraction of elemental sulfur in the back of the cathode that was unreacted, we can calculate a corrected spectral fraction of elemental sulfur (referred to as F_{S_8}) through equation 5.21:

$$\frac{f_{S_8}}{f_0} = F_{S_8} \quad (5.21)$$

The dependence of F_{S_8} on capacity is obtained from the dependences of f_{S_8} and f_0 on capacity (Figures 5.7 and 5.9b). By definition, the corrected spectral fraction of polysulfides created in the back of the cathode is given by:

$$1 - F_{S_8} = F_{PS,0} \quad (5.22)$$

The true mole fractions of elemental sulfur and polysulfide dianions for the sulfur in the back of the cathode, Y_{S_8} and $Y_{PS,0}$, are then obtained by using equations 5.23 and 5.24 to convert spectral fractions into mole fractions:

$$Y_{S_8} = \frac{\left(\frac{F_{S_8}}{8}\right)}{\left(\frac{F_{S_8}}{8}\right) + \left(\frac{F_{PS,0}}{x_{avps}}\right)} \quad (5.23)$$

$$Y_{PS,0} = \frac{\left(\frac{F_{PS,0}}{x_{avps}}\right)}{\left(\frac{F_{S_8}}{8}\right) + \left(\frac{F_{PS,0}}{x_{avps}}\right)} \quad (5.24)$$

The dependence of Y_{S_8} and $Y_{PS,0}$ on capacity is shown in Figure 5.10. It is evident from this figure that 58% of S_8 is converted to polysulfides at the back of the cathode. Note that in equations 5.8 through 5.24 all quantities are functions of capacity, Q , (or scan number) except I_0 and S_0 . For simplicity, this is not explicitly indicated in the equations.

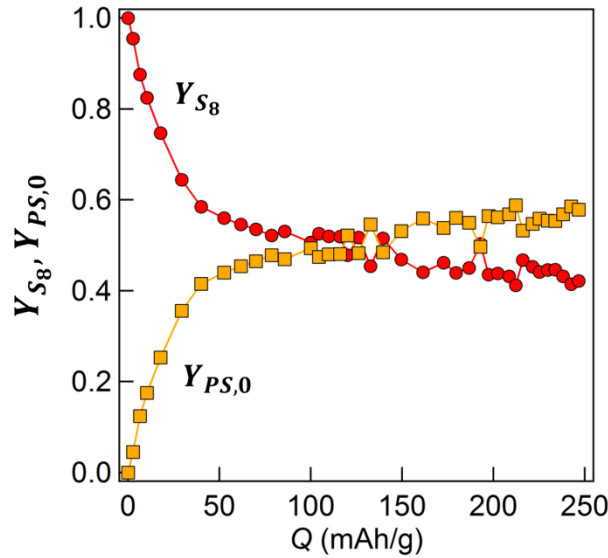


Figure 5.10 The fraction of sulfur (on an atomic basis) originally in the back of the cathode at the beginning of discharge proportioned into two components: unreacted elemental sulfur, having a mole

fraction of Y_{S_8} and polysulfide dianions, having a mole fraction of $Y_{PS,0}$.

We can then examine how the fraction of elemental sulfur remaining in the back of the cathode compares to what is expected assuming three highly simplified electrochemical reactions:



The fraction of sulfur remaining for each hypothetical reaction is calculated using the known number of electrons per sulfur molecule based on the discharge current and known cathode composition. The calculated mole fractions of S_8 remaining for reaction equations (5.25), (5.26), and (5.27), represented by $Y_{S_8}(25)$, $Y_{S_8}(26)$, and $Y_{S_8}(27)$, respectively, are plotted as a function of capacity in Figure 5.11, along with the measured mole fraction of elemental sulfur remaining in the back of the cathode.

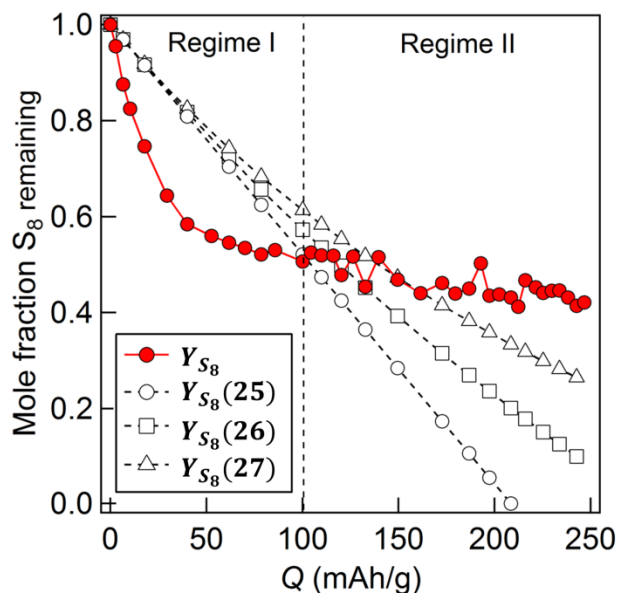


Figure 5.11 Mole fraction of elemental sulfur remaining based on the spectroscopic analysis (filled symbols) and three assumed hypothetical electrochemical reduction reactions (5.25), (5.26), and (5.27) (open symbols).

Figure 5.11 shows that the fraction of elemental sulfur remaining in the cathode decreases more rapidly than the three assumed electrochemical reactions would allow. This indicates that elemental sulfur cannot be consumed by electrochemical reactions alone. In other words, elemental sulfur at the back of the cathode is consumed both electrochemically and chemically. This mode of elemental sulfur consumption continues until $Q = 100$ mAh/g, and we refer to this as Regime I. Beyond this point, elemental sulfur consumption is much slower than that expected based on electrochemical reactions. We conclude that sulfur consumption in this regime (Regime II) is dominated by chemical reactions. The crossover from Regime I to Regime II is

coincident with the crossover in the voltage profile from the low capacity plateau to the high capacity plateau.

We interpret these results as follows: in Regime I, a combination of chemical and electrochemical reactions result in a systematic decrease of x_{av} at the back of the cathode. At the end of this regime, polysulfides with x_{avps} of about 5 are obtained, and about 50% of the sulfur at the back of the cathode is consumed. This is followed by Regime II, wherein elemental sulfur is only consumed by chemical reactions. About 58% of the elemental sulfur is consumed at the end of Regime II. Polysulfides with an x_{avps} of about 5, formed in the front of the cathode, diffuse into the back throughout both regimes, resulting in a dilution of the signal from the elemental sulfur. The slowing down of electrochemical reactions in Regime II may arise due to pore blockage in the front of the electrode and concomitant absence of lithium salt at the back of the cathode or, the coating of the electronically conducting carbon particles by an insulating precipitate of Li_2S_2 around the electronically conducting carbon particles (see Figure 5.7).

The nature of chemical reactions occurring in the cathode is not entirely clear. Examining the identity of the polysulfide dianion species (Figure 5.8) that were present in the cathode, it is also apparent that the chemical consumption of elemental sulfur is coupled to the presence of intermediate chain length polysulfide dianions (Li_2S_x , $4 \leq x \leq 6$). Reactions between elemental sulfur and polysulfide dianions are governed by the following general equation:



Assuming that Li_2S_8 is the longest polysulfide that can be formed, the polysulfide dianion reactant in equation 5.28 cannot be Li_2S_8 . If the reactant were Li_2S_6 , the lowest value of y would be $y = 4$. For shorter chain polysulfides, such as Li_2S_4 , $y = 2$. The likelihood that a reaction requiring five reactant molecules would take place (i.e. when Li_2S_6 is the reactant) is lower than that requiring three or fewer molecules. We thus propose that chemical reactions between elemental sulfur and polysulfide dianions likely involve short chain polysulfide dianions (i.e. when Li_2S_2 , Li_2S_3 , or Li_2S_4 are the reactants), such as:



Our observation that x_{avps} remains constant in Regimes I and II indicates that a decrease in polysulfide chain length due to electrochemical reactions is compensated for by an increase in chain length due to chemical reactions, e.g. reaction 5.29.

To summarize our overall findings, we present Figure 5.12, which plots the ratio of total sulfur in the back of the cathode (on an atomic basis) (S_T) to the original amount of sulfur in the back of the cathode (on an atomic basis) (S_0). This ratio is equal to the measured ratio I_n/I_0 presented in Figure 5.9a. The back of the cathode consists of three components: elemental sulfur, polysulfide dianions that were created in the back of the cathode by electrochemical conversion of sulfur, and polysulfide dianions that diffused to the back of the cathode. The lengths ‘a’, ‘b’, and ‘c’ are used along with equations presented below the plot in Figure 5.12 to illustrate how the different spectral fractions of each component were calculated. Without the diffusion of polysulfide dianion species, the composition of the back of the cathode could be described by only F_{S_8} and $F_{PS,0}$. However, because polysulfide dianion species diffused to the back of the cathode, the spectral fractions F_{S_8} and $F_{PS,0}$ are effectively diluted, resulting in the

spectral fractions f_{S_8} , and $f_{PS,0}$. The spectral fraction of diffused polysulfide dianion species is given by $f_{PS,D}$, which is equal to the fraction of sulfur (on an atomic basis) that has diffused to the back of the cathode (f_D). The spectral fractions f_{S_8} , $f_{PS,0}$, and $f_{PS,D}$ describe the spectra shown in Figure 5.4.

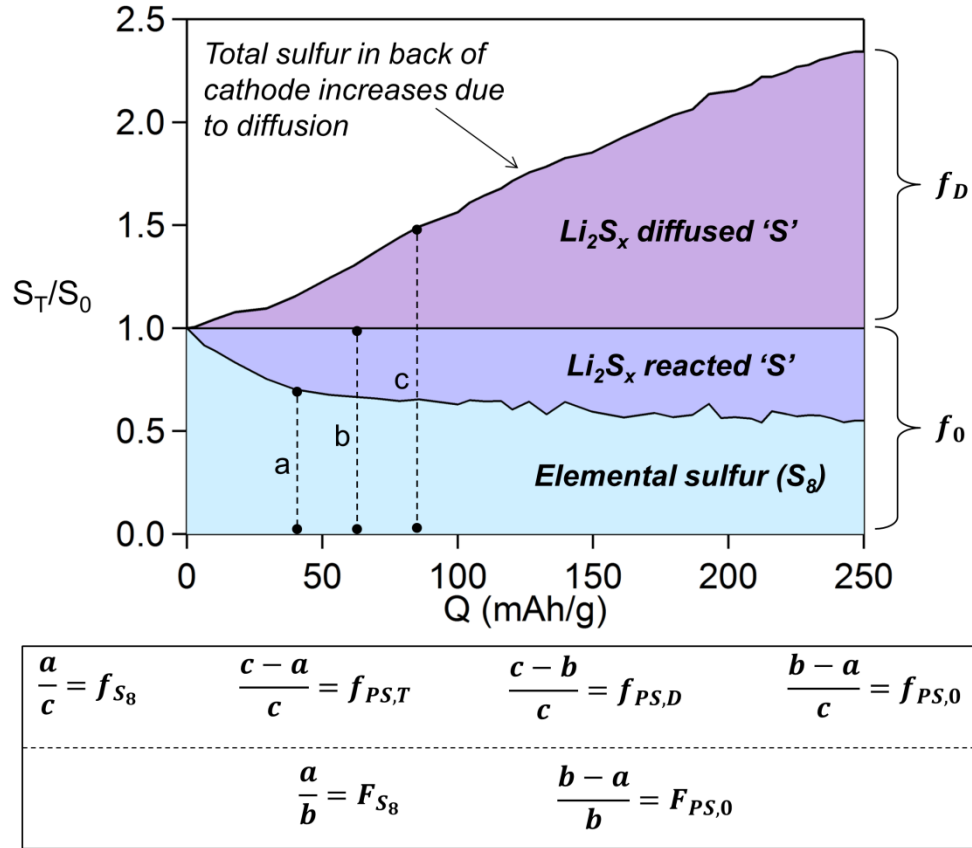


Figure 5.12 Spectral fractions of elemental sulfur and polysulfide dianions in the back of the cathode as a function of capacity. Here, the lines ‘a’, ‘b’, and ‘c’ are provided along with equations below the plot to graphically illustrate how each variable was calculated. The spectral fractions f_{S_8} , $f_{PS,T}$, $f_{PS,D}$, and $f_{PS,0}$ describe the composition of the back of the cathode as a function of capacity. The variable f_0 represents the fraction of sulfur in the back of the cathode that was present since the beginning of discharge; f_D represents the fraction of sulfur present in the back of the cathode as a result of polysulfide dianion diffusion. The corrected spectral fractions F_{S_8} and $F_{PS,0}$ represent the composition of the sulfur (on an atomic basis) that was present in the back of the cathode since the beginning of discharge.

Converting the spectral fractions of elemental sulfur and polysulfide dianion species to mole fractions, we arrive at Figure 5.13. Here, we plot the mole fractions of elemental sulfur (y_{S_8}) and all polysulfide dianions ($y_{PS,T}$) in the back of the cathode as a function of capacity. The total mole fraction of polysulfide dianions ($y_{PS,T}$) consists of two components, diffused polysulfide dianions ($y_{PS,D}$), and polysulfide dianions created in the back of the cathode ($y_{PS,0}$). Figure 5.13 describes the mole fraction of all sulfur containing species in the back of the cathode,

whereas Figures 5.10 and 5.11 only describe the composition of sulfur (on an atomic basis) that was present in the back of the cathode since the beginning of discharge.

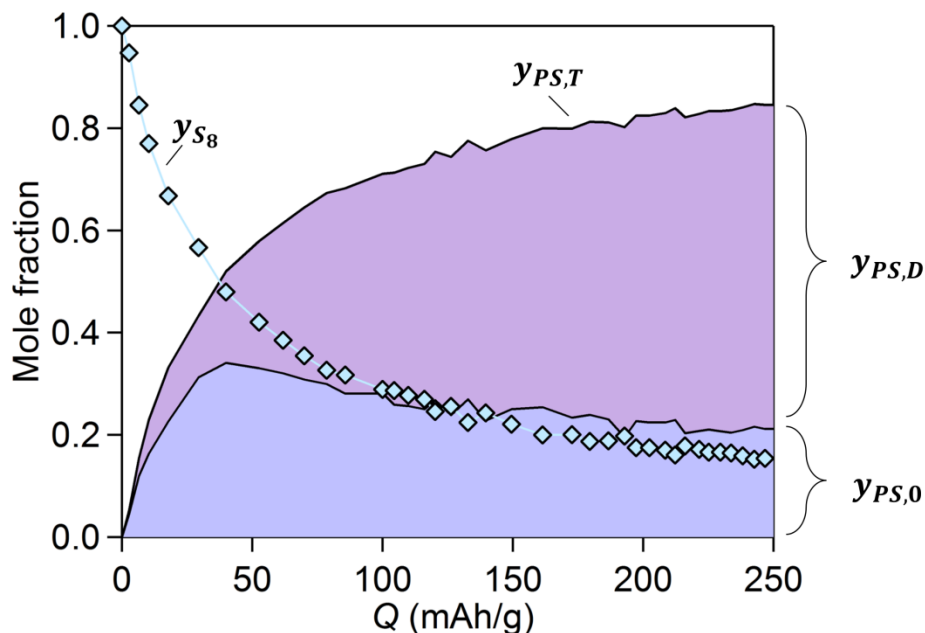


Figure 5.13 Mole fractions of elemental sulfur (S_8) (y_{S_8}) and polysulfide dianions ($y_{PS,T}$) in the back of the cathode as a function of capacity. The polysulfide dianions in the back of the cathode are split into two components: a mole fraction representing polysulfide dianions that have diffused to the back of the cathode ($y_{PS,D}$) and a mole fraction representing polysulfide dianions created in the back of the cathode ($y_{PS,0}$).

In Figure 5.13, it is evident that the electrochemical conversion of sulfur into polysulfides dominates the back of the cathode for $0 \leq Q \leq 50$. Beyond this point, electrochemical conversion of elemental sulfur slows down, and diffusion of polysulfides from the front of the cathode becomes increasingly important. In the $Q \geq 100$ mAh/g regime, electrochemical conversion of sulfur is negligible and polysulfide build-up in the back of the cathode is dominated by diffusion from the front. Diffusion of new polysulfide dianions from the front of the cathode slows down as Q approaches 252 mAh/g, because as this point is reached, electrochemical reactions throughout the cathode slow down.

It is perhaps appropriate to conclude this section by highlighting the differences between the approach used in the present study and work we have previously reported.⁽¹¹⁵⁾ In reference⁽¹¹⁵⁾, our group studied the first discharge of an Li-S cell using an X-ray beam that was incident on the lithium side (anode side). The XAS data in this study was thus dominated by polysulfides that were present in the electrolyte separator, rather than the cathode. An important conclusion of the work in reference⁽¹¹⁵⁾ was that polysulfide radical anions were detected in the electrolyte due to the presence of an XAS signal at 2468-2469 eV. Signatures of polysulfide radicals were not detected in our experiments reported in this paper. The formation of radical anions likely occurs through disproportionation reactions with electrochemically formed polysulfide dianions as reactants.^(42, 115, 140) We have also recently shown that in ether based solvents, polysulfide radical anion formation is favored at low concentrations of sulfur.⁽¹⁴⁰⁾ Thus, it is likely that the

low concentration of polysulfide species in the electrolyte separator in reference ⁽¹¹⁵⁾ enabled the formation of polysulfide radical anions. Additionally, the sulfur cathode used in reference ⁽¹¹⁵⁾ was only 35 μm thick. The roles of differences in cathode geometry and the presence of lithium metal in the vicinity of the portion of the cell that was probed by XAS are not clear at this juncture. In the future, we will examine Li-S cells with thick cathodes from the anode side.

In references ^(18, 69, 93, 94, 126, 127, 132), in situ XAS was similarly used to probe the Li-S cell cathode, but different results were obtained than those shown here. For instance, Cuisiner et al. detected radical polysulfide anions when dimethylacetamide was used as the solvent.⁽⁹³⁾ It is well-known that this solvent stabilizes significant concentrations of polysulfide radical anions. Additional differences in the results shown here and the results reported by other in situ XAS studies of Li-S cathodes may stem from: (1) differences in cathode thickness, sulfur loading, or discharge rate (2) the use of low molecular weight solvents rather than the high molecular weight polymer electrolyte used here, and (3) differences in spectral standards and analysis than those presented here. Reconciliation of results obtained in different Li-S cells is a worthwhile but challenging goal that is well beyond the scope of the present study.

5.4 Conclusions

In situ X-ray absorption spectroscopy at the sulfur K-edge was used to probe the back of a thick Li-S cathode during discharge. The experimentally obtained spectra were interpreted using theoretical spectral standards. Analysis of the spectra and the fluorescence intensity measured during each scan showed that polysulfide dianion species produced by electrochemical reactions diffused to the back of the cathode during discharge. To our knowledge, this is the first time this phenomenon has been quantified. We explain this finding as follows: the limited diffusion of lithium ions to the back of a thick Li-S cathode will lead to higher reaction rates in the front of the cathode relative to the back of the cathode. This difference in reaction rate leads to a higher concentration of polysulfide dianions in the front of the cathode, which in turn creates a concentration gradient that leads to the diffusion of polysulfide dianions to the back of the cathode.

The conversion of sulfur in the back of the cathode occurs in two distinct steps. In the first step, elemental sulfur is consumed by a combination of electrochemical reduction and chemical reactions. In the second step, elemental sulfur is consumed by chemical reactions alone. Although the capacity obtained for the Li-S cell was low (only 15% of the Li-S cell theoretical capacity), 58% of the elemental sulfur in the back of the cathode was converted to polysulfide dianion species due to a combination of electrochemical and chemical reactions. This result has important implications for our understanding of how Li-S redox reactions proceed, and also when considering the shelf life of partially discharged Li-S cells.

Going further, our results suggest that intermediate chain polysulfide dianions (Li_2S_x , $4 \leq x \leq 6$) are the dominant species at the back of the cathode. Since elemental sulfur is a crystalline insulating solid, it is likely that reactions between elemental sulfur and these intermediate chain length polysulfide dianions are essential for complete utilization of a sulfur cathode.

Our study is but one step toward the complete understanding of processes that occur during the first discharge in an Li-S cell with a thick sulfur electrode.

5.5 Acknowledgements

This work was supported by the Assistant Secretary for Energy Efficiency and Renewable Energy, Office of Vehicle Technologies of the US Department of Energy under Contract DE-AC02-05CH11231 under the Battery Materials Research program. Use of the Stanford Synchrotron Radiation Lightsource, SLAC National Accelerator Laboratory, is supported by the U.S. Department of Energy, Office of Science, Office of Basic Energy Sciences under Contract No. DE-AC02-76SF00515. The Advanced Light Source is supported by the Director, Office of Science, Office of Basic Energy Sciences, of the U.S. Department of Energy under Contract No. DE-AC02-05CH11231. We also acknowledge the help of Erik Nelson and Matthew Latimer of SSRL, and Ethan Crumlin and Wayne Stolte of ALS.

5.6 Supporting information

5.6.1 Calculation of X-ray penetration depth/fraction of photons reaching each depth

The intensity of photons at a given depth, ' t ' is related to the intensity of incoming photons via Beer's law. The ratio of photon intensity at a given depth to the incoming photon intensity represents the fraction of photons capable of penetrating to a given depth, as given by Equation (5.S1):

$$\frac{I_f}{I_0} = e^{-\mu(E)\rho t} \quad (5.S1)$$

Here, I_f is the X-ray intensity at depth ' t ', I_0 is the incoming X-ray intensity, and $\mu(E)$ is the energy-dependent absorption coefficient of the material through which X-ray photons pass, which has a density denoted by ρ .

During the in situ XAS experiments, incoming photons first passed through a thin Kapton film, and then entered the cathode. The fraction of incident photons capable of transmitting to a given cathode depth is thus given by equation 5.S2, which was used to calculate the values shown in column 2 of Table 5.1:

$$\frac{I_f}{I_0} = e^{(-\mu_{Kap}(E) \cdot \rho_{Kap} \cdot t_{Kap})} \cdot e^{\left(-\mu_{cat}(E) \cdot \rho_{cat} \cdot \left(\frac{T}{\sin(45^\circ)}\right)\right)} \quad (5.S2)$$

Here, $\mu_{Kap}(E)$ is the absorption coefficient of Kapton, t_{Kap} is the thickness of the Kapton film (8 μm), and ρ_{Kap} is the density of Kapton (taken to be 1.43 g/cm^3). The overall absorption coefficient for the cathode is given by $\mu_{cat}(E)$, and ρ_{cat} represents the cathode density (which was assumed to be 1.0 g/cm^3). The cathode thicknesses presented in column 1 of Table 5.1 are represented in equation 5.S2 by the variable ' T '. Here, ' T ' is divided by $\sin(45^\circ)$, as the incident X-rays enter the cathode at a 45° angle. The overall absorption coefficient for the cathode ($\mu_{cat}(E)$) is determined by multiplying each element's absorption coefficient by the element's mass fraction in the cathode, and summing the mass weighted element absorption coefficients together, as shown in equation 5.S3. In our case, the cathode contained chemicals that consisted only of carbon, hydrogen, oxygen, chlorine, lithium, and sulfur atoms.

$$\mu_{cat}(E) = \mu_C(E) \cdot x_C + \mu_H(E) \cdot x_H + \mu_O(E) \cdot x_O + \mu_{Cl}(E) \cdot x_{Cl} + \mu_{Li}(E) \cdot x_{Li} + \mu_S(E) \cdot x_S \quad (5.S3)$$

Here, $\mu_C(E)$ is the absorption coefficient of carbon, $\mu_H(E)$ is the absorption coefficient of hydrogen, $\mu_O(E)$ is the absorption coefficient of oxygen, $\mu_{Cl}(E)$ is the absorption coefficient of chlorine, $\mu_{Li}(E)$ is the absorption coefficient of lithium, and $\mu_S(E)$ is the absorption coefficient of sulfur. The values of x are the mass fraction of each element in the cathode. Similarly, the absorption coefficient of Kapton is calculated using equation 5.S4:

$$\mu_{Kap}(E) = \mu_C(E) \cdot y_C + \mu_H(E) \cdot y_H + \mu_O(E) \cdot y_O + \mu_N(E) \cdot y_N \quad (5.S4)$$

Here, the cathode mass fractions for each element have been replaced by mass fractions for each element determined through the chemical equation of Kapton (i.e. polyimide). These mass fractions are denoted by the variable y .

The absorption coefficient values in equations 5.S1 through 5.S4 depend on the energy of the transmitting X-ray photons. Thus, each absorption coefficient must be evaluated at a chosen energy. To estimate the fraction of incident photons capable arriving at each depth (the values shown in column 2 of Table 5.1), the element absorption coefficients in equation 5.S3 and S4 were determined at an X-ray energy of 2473.0 eV. The absorption coefficient values were obtained using the X-ray data analysis program Hephaestus⁽¹³⁹⁾ and are given in Table 5.S1 below. The overall absorption coefficients for $\mu_{Kap}(E)$ and $\mu_{cat}(E)$ are shown in Table 5.S2 below.

Equation 5.S2 was also used to calculate the fraction of photons capable of emerging from a given depth ‘ T ’ and making it to the fluorescence detector. However, the element absorption coefficients and the Kapton absorption coefficient were determined at the energy of fluorescent photons emitted during the XAS process, rather than the energy of incoming X-ray photons. For estimation, this energy was assumed to be the energy of the sulfur $K\alpha_1$ emission line: 2309.0 eV

The fraction shown in column 3 of Table 5.1 is calculated by multiplying the fraction of incoming photons capable of transmitting to a given depth by the fraction of fluorescent photons capable of emerging from a given depth. This calculated fraction, given by $\left(\frac{I_f}{I_0}\right)_{tot}$, is calculated through equation 5.S5:

$$\left(\frac{I_f}{I_0}\right)_{tot} = e^{-(\mu_{cat}(2473.0 \text{ eV}) + \mu_{cat}(2309.0 \text{ eV})) \cdot \rho_{cat} \cdot (T/\sin(45^\circ))} \cdot e^{-(\mu_{Kap}(2473.0 \text{ eV}) + \mu_{Kap}(2309.0 \text{ eV})) \cdot \rho_{Kap} \cdot t_{Kap}} \quad (5.S5)$$

To determine the fraction of measured fluorescence signal that corresponds to each slice of the cathode (the values shown in column 4 of Table 5.1), we use equation 5.S6:

$$\frac{\left(\frac{I_f}{I_0}\right)_{tot_i} - \left(\frac{I_f}{I_0}\right)_{tot_{i+1}}}{\sum_i^N \left(\frac{I_f}{I_0}\right)_{tot_i}} \quad (5.S6)$$

Here, $\left(\frac{I_f}{I_0}\right)_{tot_i}$ is the fraction determined by equation 5.S5 and shown in column 3 of Table 5.1 for depth ‘ i ’ in column 1. The variable $\left(\frac{I_f}{I_0}\right)_{tot_{i+1}}$ is the fraction determined by equation 5.S5 for

next depth in column 1. The summation in the denominator of equation 5.S6 is the sum of all fractions given in column 3 of Table 5.1. This is perhaps more clearly shown by equation 5.S7 below.

Table 5.S1 Absorption coefficients for each element and mass fractions of each element in cathode and Kapton

	Absorption coefficients (cm²/g) for cathode						
	Carbon	Hydrogen	Oxygen	Sulfur	Lithium	Chlorine	Nitrogen
2473.0 eV	161.17 7	0.718	379.58 3	2068.49	13.855	253.834	257.330
2309.0 eV	197.71 9	0.803	462.03 4	260.936	17.205	305.829	314.464
	Mass fractions						
Mass fraction in cathode	0.699	0.038	0.125	0.116	0.004	0.019	0
Mass fraction in Kapton	0.69	0.03	0.21	0	0	0	0.07

Table 5.S2 Overall absorption coefficients for cathode and Kapton

	$\mu_{cat}(E)$ (cm ² /g)	$\mu_{Kap}(E)$ (cm ² /g)
2473.0 eV	370.991	183.429
2309.0 eV	227.110	223.762

5.6.1.2 Sample calculations

Calculation of fraction of incident photons that reach a depth into the cathode (values shown in column 2 of Table 5.1) using a cathode depth of 5 μm for example:

$$0.652 = e^{-183.429 \cdot 1.43 \cdot (8 \cdot 10^{-4})} \cdot e^{\left(-370.991 \cdot 1 \cdot \left(\frac{5 \cdot 10^{-4}}{\sin(45^\circ)} \right) \right)}$$

Calculation of fraction of incident photons emerging from a given depth of the cathode (values shown in column 3 of Table 5.1) using a cathode depth of 5 μm for example:

$$0.442 = 0.652 \cdot e^{-223.762 \cdot 1.43 \cdot (8 \cdot 10^{-4})} \cdot e^{\left(-227.11 \cdot 1 \cdot \left(\frac{5 \cdot 10^{-4}}{\sin(45^\circ)} \right) \right)}$$

Equation 5.S7 below is an example of the format equation 5.S6 would take for the calculation of the fraction of fluorescence signal that corresponds to the slice of cathode between 5 to 10 μm . Below equation 5.S7 is the corresponding sample calculation for the 5-10 μm slice:

$$\frac{\left(\frac{I_f}{I_0}\right)_{5\mu\text{m}} - \left(\frac{I_f}{I_0}\right)_{10\mu\text{m}}}{\sum_i^N \left(\frac{I_f}{I_0}\right)_{\text{tot}_i}} \quad (5.S7)$$

$$\frac{0.442 - .311}{.627} = .209$$

5.6.2 Fitting of experimental in situ XAS spectra

To determine the ratio of the main edge to pre-edge peak areas, the experimental spectra shown in Figure 5.4 were each fit with two Gaussian peak functions and an arctangent function. The arctangent function was held to be constant for the fitting of each spectrum. The Gaussian peak parameters (peak height, width, and location along the energy axis) were fit using a least squares fitting approach. An example of the fitting is provided below in Figure 5.S1:

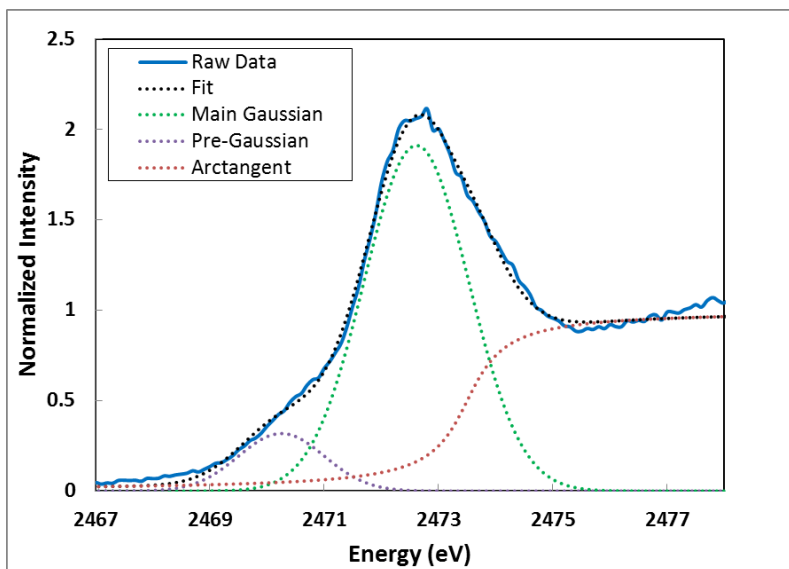


Figure 5.S1 Example of fitting in situ X-ray spectra with Gaussian peaks and an arctangent function. Spectrum shown is the eighth spectrum measured during discharge.

The parameters of the arctangent function used for the fitting of each spectrum are shown in Table 5.S3. The parameters determined for each Gaussian peak are shown in Table 5.S4.

Table 5.S3 Arctangent parameters used for the fitting of each in situ XAS spectrum

Arctangent parameters	
Center	2473.5
Width	0.25

Height	1
---------------	---

Table 5.S4 Gaussian peak parameters determined for each in situ XAS spectrum

Scan #	Main edge Gaussian Peak Parameters				Pre-edge Gaussian Peak Parameters			
	Center	Sigma	Height	Area	Center	Sigma	Height	Area
0	2472.67	0.87	2.21	4.81	2470.00	0.75	0.20	0.38
1	2472.67	0.87	2.21	4.81	2470.00	0.75	0.20	0.38
2	2472.66	0.87	2.13	4.66	2470.00	0.75	0.22	0.42
3	2472.66	0.89	2.08	4.64	2470.00	0.75	0.25	0.47
4	2472.65	0.90	2.01	4.51	2470.03	0.75	0.26	0.50
5	2472.64	0.90	1.97	4.47	2470.08	0.75	0.28	0.52
6	2472.63	0.91	1.92	4.36	2470.15	0.75	0.30	0.57
7	2472.62	0.90	1.92	4.34	2470.22	0.75	0.31	0.58
8	2472.61	0.92	1.91	4.39	2470.25	0.75	0.32	0.59
9	2472.61	0.91	1.87	4.27	2470.25	0.78	0.33	0.65
10	2472.61	0.92	1.87	4.29	2470.31	0.75	0.36	0.67
11	2472.60	0.92	1.85	4.27	2470.30	0.74	0.35	0.66
12	2472.60	0.91	1.84	4.20	2470.36	0.73	0.38	0.69
13	2472.60	0.92	1.84	4.23	2470.36	0.74	0.39	0.71
14	2472.60	0.92	1.84	4.25	2470.36	0.74	0.39	0.71
15	2472.59	0.93	1.82	4.22	2470.37	0.74	0.39	0.71
16	2472.59	0.93	1.82	4.22	2470.37	0.74	0.39	0.71
17	2472.59	0.92	1.80	4.15	2470.40	0.70	0.40	0.70
18	2472.58	0.92	1.78	4.11	2470.39	0.76	0.40	0.77
19	2472.58	0.92	1.78	4.11	2470.42	0.72	0.40	0.73
20	2472.58	0.92	1.78	4.11	2470.42	0.72	0.40	0.73
21	2472.56	0.91	1.75	3.99	2470.44	0.69	0.43	0.74
22	2472.57	0.92	1.77	4.11	2470.44	0.67	0.43	0.73
23	2472.55	0.94	1.76	4.15	2470.40	0.67	0.43	0.73
24	2472.55	0.94	1.78	4.18	2470.41	0.67	0.43	0.73
25	2472.56	0.94	1.75	4.13	2470.42	0.67	0.43	0.73
26	2472.55	0.92	1.74	4.03	2470.45	0.67	0.45	0.76
27	2472.55	0.93	1.73	4.01	2470.44	0.71	0.44	0.79
28	2472.56	0.92	1.72	3.98	2470.47	0.71	0.44	0.79
29	2472.56	0.93	1.74	4.06	2470.45	0.69	0.45	0.78
30	2472.57	0.94	1.76	4.13	2470.45	0.69	0.45	0.78
31	2472.55	0.93	1.73	4.04	2470.45	0.67	0.45	0.76
32	2472.55	0.93	1.71	4.01	2470.45	0.67	0.45	0.76

33	2472.55	0.95	1.74	4.12	2470.44	0.67	0.45	0.75
34	2472.54	0.94	1.74	4.08	2470.45	0.66	0.46	0.76
35	2472.54	0.94	1.71	4.06	2470.43	0.66	0.45	0.74
36	2472.54	0.94	1.71	4.01	2470.45	0.65	0.45	0.74
37	2472.54	0.95	1.74	4.11	2470.44	0.65	0.45	0.74
38	2472.53	0.94	1.71	4.00	2470.45	0.65	0.45	0.74

Chapter 6 – Summary

X-ray absorption spectroscopy at the sulfur K-edge has proven to be a valuable technique for studying Li-S battery reaction chemistry. This work began with experiments that were aimed at obtaining spectral standards for lithium polysulfide dianions, and elucidating the molecular origin for these species spectral features. XAS was used to probe chemically synthesized mixtures of lithium polysulfide species dissolved in a block copolymer of poly(styrene)-poly(ethylene oxide) (SEO), and a homopolymer of poly(ethylene oxide) (PEO). For both solvents, a series of spectra were gathered for polysulfide mixtures that had stoichiometric Li_2S_x 'x' values of 2, 4, 6 and 8. The simplest interpretation of the obtained system of X-ray spectra, as suggested by principal component analysis, is that Li_2S , Li_2S_4 , and Li_2S_8 are the stable lithium-sulfur containing species in polymer electrolytes. Additional theoretical calculations revealed that the main-edge peak of polysulfide dianion spectra is attributed to uncharged, internal sulfur atoms of the polysulfide chain, while the pre-edge peak is attributed to negatively charged, terminal sulfur atoms. The ratio of the main-edge to pre-edge peak can be used as an indicator of the polysulfide dianion chain length.

After examining lithium polysulfide mixtures that were chemically synthesized, the focus of this work shifted toward studying the reactions that take place in Li-S cells. Here, sulfur K-edge XAS was used to probe the electrolyte separator of partially discharged Li-S cells. Analysis of the experimentally obtained spectra using theoretically derived spectra revealed that lithium polysulfide radical anions were present in the Li-S cell electrolyte after discharge. Evidence of polysulfide radical species was only obtained for a cell that was stopped at an early depth of discharge, which is congruent with what has previously been observed in literature. Analysis of the distribution of polysulfide species present suggested that the radical species were formed through chemical disproportionation reactions, rather than through electrochemical reactions. The evidence of polysulfide radical species in these cells is notable, as it has been debated whether or not radical species are stable in ether-based solvents like the one employed in the Li-S cells studied here. This motivated the next phase of the work.

The presence of polysulfide radical species in ether-based studies was then studied using a combination of UV-vis and EPR spectroscopy. Some authors claimed that an absorption feature observed at a wavelength of 600-620 nm in the spectra of ether-based polysulfide mixtures could be attributed to polysulfide radical species. Other authors claimed that the peak is attributed to polysulfide dianion species. By coupling EPR to UV-vis, we unequivocally showed that radical species were present in TEGDME, and that their characteristic peak occurred at 600-620 nm. Further analysis of the UV-vis spectra revealed that as the concentration of polysulfide species (and sulfur) increases, the fraction of sulfur present in the form of polysulfide radical species decreases. That is, at higher concentrations, radical species are less favored and likely recombine to form their respective polysulfide dianion via reactions like: $2 \text{LiS}_3 \rightarrow \text{Li}_2\text{S}_6$.

Lastly, XAS was used to probe the back of a thick Li-S cathode during discharge. Analysis of the in situ spectra was performed using the theoretically derived spectra of lithium polysulfide species. This analysis, along with examination of the fluorescence intensity, revealed that polysulfide dianion species formed in the front of the cathode diffused to the back of the cathode during discharge. The polysulfide dianion species detected in the cathode were of intermediate chain length (i.e. $4 \leq x \leq 6$). High conversion of elemental sulfur to polysulfide dianion species was also observed. This suggests that intermediate polysulfide dianion species may play a critical role in the conversion of elemental sulfur. This result is critical to our

understanding of how elemental sulfur is chemically consumed in an Li-S cathode, and has important implications for the Li-S cell charge/discharge processes. If sulfur is not electrochemically reduced during discharge, it likely will not be converted to polysulfide dianion species until polysulfide dianion species of intermediate chain length (or shorter) are present. In the case of charging, if polysulfide dianion species of intermediate chain length (or shorter) are present at the end of charging, elemental sulfur that is formed will likely react with the leftover intermediate chain length polysulfide dianion species. However, if only long chain polysulfide dianion species are leftover, this conversion likely will not occur.

Chapter 7 – References

1. D. Bresser, S. Passerini and B. Scrosati, *Chemical Communications*, **49**, 10545 (2013).
2. P. G. Bruce, S. A. Freunberger, L. J. Hardwick and J.-M. Tarascon, *Nature materials*, **11**, 19 (2012).
3. M. Armand and J. M. Tarascon, *Nature*, **451**, 652 (2008).
4. M. S. Whittingham, *Proceedings of the IEEE*, **100**, 1518 (2012).
5. M.-K. Song, E. J. Cairns and Y. Zhang, *Nanoscale*, **5**, 2186 (2013).
6. R. Xu, J. Lu and K. Amine, *Advanced Energy Materials*, **5**, n/a (2015).
7. A. Manthiram, Y. Fu and Y.-S. Su, *Accounts of Chemical Research*, **46**, 1125 (2012).
8. R. D. Rauh, F. S. Shuker, J. M. Marston and S. B. Brummer, *Journal of Inorganic and Nuclear Chemistry*, **39**, 1761 (1977).
9. H. Yamin, A. Gorenshstein, J. Penciner, Y. Sternberg and E. Peled, *Journal of The Electrochemical Society*, **135**, 1045 (1988).
10. A. Rosenman, E. Markevich, G. Salitra, D. Aurbach, A. Garsuch and F. F. Chesneau, *Advanced Energy Materials*, **5**, n/a (2015).
11. F. Seel, H. J. Güttler, G. Simon and A. Wieckowski, in *Non-Aqueous Solutions-5*, p. 45, Pergamon (1977).
12. A. Manthiram, Y. Fu, S.-H. Chung, C. Zu and Y.-S. Su, *Chemical Reviews*, **114**, 11751 (2014).
13. Y. V. Mikhaylik and J. R. Akridge, *Journal of The Electrochemical Society*, **151**, A1969 (2004).
14. B. E. Warren and J. T. Burwell, *The Journal of Chemical Physics*, **3**, 6 (1935).
15. R. A. Sharma, *Journal of The Electrochemical Society*, **119**, 1439 (1972).
16. H. Okamoto, *Journal of Phase Equilibria*, **16**, 94 (1995).
17. N. A. Cañas, S. Wolf, N. Wagner and K. A. Friedrich, *Journal of Power Sources*, **226**, 313 (2013).
18. M. A. Lowe, J. Gao and H. D. Abruna, *RSC Advances*, **4**, 18347 (2014).
19. J. Nelson, S. Misra, Y. Yang, A. Jackson, Y. Liu, H. Wang, H. Dai, J. C. Andrews, Y. Cui and M. F. Toney, *Journal of the American Chemical Society*, **134**, 6337 (2012).
20. S.-E. Cheon, K.-S. Ko, J.-H. Cho, S.-W. Kim, E.-Y. Chin and H.-T. Kim, *Journal of The Electrochemical Society*, **150**, A796 (2003).
21. H.-S. Ryu, H.-J. Ahn, K.-W. Kim, J.-H. Ahn and J.-Y. Lee, *Journal of Power Sources*, **153**, 360 (2006).
22. L. Yuan, X. Qiu, L. Chen and W. Zhu, *Journal of Power Sources*, **189**, 127 (2009).
23. W. Giggenschbach, *Journal of Inorganic and Nuclear Chemistry*, **30**, 3189 (1968).
24. A. Kamysny, I. Ekelchik, J. Gun and O. Lev, *Analytical chemistry*, **78**, 2631 (2006).
25. A. Kamysny, A. Goifman, J. Gun, D. Rizkov and O. Lev, *Environmental Science & Technology*, **38**, 6633 (2004).
26. B. S. Kim and S. M. Park, *Journal of The Electrochemical Society*, **140**, 115 (1993).
27. E. Levillain, F. Gaillard and J. P. Lelieur, *Journal of Electroanalytical Chemistry*, **440**, 243 (1997).
28. R. Steudel, *Elemental Sulfur and Sulfur-Rich Compounds II*, Springer Berlin Heidelberg (2003).
29. D. Marmorstein, Solid state lithium/sulfur batteries for electric vehicles: Electrochemical and spectroelectrochemical investigations, in *Chemical Engineering*, p. 183, University of California, Berkeley, Ann Arbor (2002).
30. K. H. Wujcik, J. Velasco-Velez, C. H. Wu, T. Pascal, A. A. Teran, M. A. Marcus, J. Cabana, J. Guo, D. Prendergast, M. Salmeron and N. P. Balsara, *Journal of The Electrochemical Society*, **161**, A1100 (2014).
31. C. Barchasz, F. Molton, C. Duboc, J. C. Lepretre, S. Patoux and F. Alloin, *Analytical chemistry*, **84**, 3973 (2012).
32. N. A. Cañas, D. N. Fronczek, N. Wagner, A. Latz and K. A. Friedrich, *The Journal of Physical Chemistry C*, **118**, 12106 (2014).
33. F. Gaillard and E. Levillain, *Journal of Electroanalytical Chemistry*, **398**, 77 (1995).

34. M. U. M. Patel, R. Demir-Cakan, M. Morcrette, J.-M. Tarascon, M. Gaberscek and R. Dominko, *ChemSusChem*, **6**, 1177 (2013).
35. M. U. M. Patel and R. Dominko, *ChemSusChem*, **7**, 2167 (2014).
36. Q. Zou and Y.-C. Lu, *The journal of physical chemistry letters*, **7**, 1518 (2016).
37. N. S. A. Manan, L. Aldous, Y. Alias, P. Murray, L. J. Yellowlees, M. C. Lagunas and C. Hardacre, *The Journal of Physical Chemistry B*, **115**, 13873 (2011).
38. S.-I. Tobishima, H. Yamamoto and M. Matsuda, *Electrochimica Acta*, **42**, 1019 (1997).
39. J. Badoz-Lambling, R. Bonnaterre, G. Cauquis, M. Delamar and G. Demange, *Electrochimica Acta*, **21**, 119 (1976).
40. D.-H. Han, B.-S. Kim, S.-J. Choi, Y. Jung, J. Kwak and S.-M. Park, *Journal of The Electrochemical Society*, **151**, E283 (2004).
41. E. L. Levillain, P.; Gobeltz, N.; Lelieur, J. P., *New Journal of Chemistry*, **21**, 335 (1997).
42. Q. Wang, J. Zheng, E. Walter, H. Pan, D. Lv, P. Zuo, H. Chen, Z. D. Deng, B. Y. Liaw, X. Yu, X. Yang, J.-G. Zhang, J. Liu and J. Xiao, *Journal of The Electrochemical Society*, **162**, A474 (2015).
43. T. Chivers and I. Drummond, *Inorganic Chemistry*, **11**, 2525 (1972).
44. M. Hagen, P. Schiffels, M. Hammer, S. Dörfler, J. Tübke, M. J. Hoffmann, H. Althues and S. Kaskel, *Journal of The Electrochemical Society*, **160**, A1205 (2013).
45. A. Kawase, S. Shirai, Y. Yamoto, R. Arakawa and T. Takata, *Physical Chemistry Chemical Physics*, **16**, 9344 (2014).
46. Y. Diao, K. Xie, S. Xiong and X. Hong, *Journal of The Electrochemical Society*, **159**, A1816 (2012).
47. J.-T. Yeon, J.-Y. Jang, J.-G. Han, J. Cho, K. T. Lee and N.-S. Choi, *Journal of The Electrochemical Society*, **159**, A1308 (2012).
48. J. Yano and V. K. Yachandra, *Photosynthesis research*, **102**, 241 (2009).
49. M. Newville, Fundamentals of XAFS, in *Consortium for Advanced Radiation Sources* (2004).
50. P. Pfalzer, J. P. Urbach, M. Klemm, S. Horn, M. L. denBoer, A. I. Frenkel and J. P. Kirkland, *Physical Review B*, **60**, 9335 (1999).
51. L. Tröger, D. Arvanitis, K. Baberschke, H. Michaelis, U. Grimm and E. Zschech, *Physical Review B*, **46**, 3283 (1992).
52. M. A. M. Marcus, A., Overabsorption("Self-absorption"), Thickness and Hole Effects in EXAFS, in (2002).
53. F. Jalilehvand, *Chemical Society Reviews*, **35**, 1256 (2006).
54. T. A. Pascal, C. D. Pemmaraju and D. Prendergast, *Physical Chemistry Chemical Physics*, **17**, 7743 (2015).
55. T. A. Pascal, K. H. Wujcik, J. Velasco-Velez, C. Wu, A. A. Teran, M. Kapilashrami, J. Cabana, J. Guo, M. Salmeron, N. Balsara and D. Prendergast, *The Journal of Physical Chemistry Letters*, **5**, 1547 (2014).
56. D. Prendergast and G. Galli, *Physical review letters*, **96**, 215502 (2006).
57. R. D. Rauh, K. M. Abraham, G. F. Pearson, J. K. Surprenant and S. B. Brummer, *Journal of The Electrochemical Society*, **126**, 523 (1979).
58. V. S. Kolosnitsyn and E. V. Karaseva, *Russ J Electrochem*, **44**, 506 (2008).
59. S. B. R. Brummer, R. D.; Marston, J. M.; Shuker, R.S., Low Temperature Lithium/Sulfur Secondary Battery, in, p. 1, Research and Development Administration, US Department of Energy, Washington, DC (1976).
60. X. Ji, K. T. Lee and L. F. Nazar, *Nature materials*, **8**, 500 (2009).
61. H. Wang, Y. Yang, Y. Liang, J. T. Robinson, Y. Li, A. Jackson, Y. Cui and H. Dai, *Nano Letters*, **11**, 2644 (2011).
62. C. Liang, N. J. Dudney and J. Y. Howe, *Chemistry of Materials*, **21**, 4724 (2009).
63. H. Yamin, J. Penciner, A. Gorenshtain, M. Elam and E. Peled, *Journal of Power Sources*, **14**, 129 (1985).

64. T. T. Pickering, A., *Sulfur in Organic and Inorganic Chemistry*, New York (1972).
65. R. P. Martin, W. H. Doub, J. L. Roberts and D. T. Sawyer, *Inorganic Chemistry*, **12**, 1921 (1973).
66. P. Eisenberger and B. M. Kincaid, *Science*, **200**, 1441 (1978).
67. D. E. Sayers, E. A. Stern and F. W. Lytle, *Physical review letters*, **27**, 1204 (1971).
68. J. Gao, M. A. Lowe, Y. Kiya and H. D. Abruña, *The Journal of Physical Chemistry C*, **115**, 25132 (2011).
69. M. Cuisinier, P.-E. Cabelguen, S. Evers, G. He, M. Kolbeck, A. Garsuch, T. Bolin, M. Balasubramanian and L. F. Nazar, *The Journal of Physical Chemistry Letters*, **4**, 3227 (2013).
70. M. Ruitenbeek, A. J. van Dillen, F. M. F. de Groot, I. E. Wachs, J. W. Geus and D. C. Koningsberger, *Topics in Catalysis*, **10**, 241 (2000).
71. S. Beauchemin, D. Hesterberg and M. Beauchemin, *Soil Science Society of America Journal*, **66**, 83 (2002).
72. T. Ressler, J. Wong, J. Roos and I. L. Smith, *Environmental Science & Technology*, **34**, 950 (2000).
73. J. Goulon, C. Goulon-Ginet, R. Cortes and J. M. Dubois, *Journal De Physique*, **43**, 539 (1982).
74. M. Singh, O. Odusanya, G. M. Wilmes, H. B. Eitouni, E. D. Gomez, A. J. Patel, V. L. Chen, M. J. Park, P. Fragouli, H. Iatrou, N. Hadjichristidis, D. Cookson and N. P. Balsara, *Macromolecules*, **40**, 4578 (2007).
75. S. M. Webb, *Physica Scripta*, **2005**, 1011 (2005).
76. A. Manceau and K. L. Nagy, *Geochimica et Cosmochimica Acta*, **99**, 206 (2012).
77. I. J. Pickering, G. N. George, E. Y. Yu, D. C. Brune, C. Tuschak, J. Overmann, J. T. Beatty and R. C. Prince, *Biochemistry*, **40**, 8138 (2001).
78. F. I. Allen, M. Watanabe, Z. Lee, N. P. Balsara and A. M. Minor, *Ultramicroscopy*, **111**, 239 (2011).
79. E. R. Malinowski, *Factor Analysis in Chemistry*, John Wiley & Sons, Inc., New York (1991).
80. A. I. Frenkel, O. Kleinfeld, S. R. Wasserman and I. Sagi, *Journal of Chemical Physics*, **116**, 9449 (2002).
81. S. R. Wasserman, P. G. Allen, D. K. Shuh, J. J. Bucher and N. M. Edelstein, *Journal of Synchrotron Radiation*, **6**, 284 (1999).
82. A. C. Scheinost, A. Rossberg, M. Marcus, S. Pfister and R. Kretzschmar, *Physica Scripta*, **2005**, 1038 (2005).
83. C. Barchasz, F. Molton, C. Duboc, J.-C. Leprêtre, S. Patoux and F. Alloin, *Analytical Chemistry*, **84**, 3973 (2012).
84. L. Nazar, M. Cuisinier, P.-E. Cabelguen, B. Adams, A. Garsuch and M. Balasubramanian, *Energy & Environmental Science* (2014).
85. M. U. M. Patel, I. Arčon, G. Aquilanti, L. Stievano, G. Mali and R. Dominko, *ChemPhysChem*, (In press) (2014).
86. R. D. Rauh, F. S. Shuker, J. M. Marston and S. B. Brummer, *J. Inorg. Nucl. Chem.*, **39**, 1761 (1977).
87. R. Bonnaterre and G. Cauquis, *Journal of the Chemical Society, Chemical Communications*, 293 (1972).
88. T. Chivers and I. Drummond, *Inorganic Chemistry*, **11**, 2525 (1972).
89. T. Chivers and P. J. Elder, *Chemical Society Reviews*, **42**, 5996 (2013).
90. J. M. Durand, J. OlivierFourcade, J. C. Jumas, M. Womes, C. M. Teodorescu, A. Elafif, J. M. Esteva and R. C. Karnatak, *J Phys B-at Mol Opt*, **29**, 5773 (1996).
91. V. L. Tauson, J. Goettlicher, A. N. Sapozhnikov, S. Mangold and E. E. Lustenberg, *European Journal of Mineralogy*, **24**, 133 (2012).
92. S. Tarling, P. Barnes and J. Klinowski, *Acta Crystallographica Section B: Structural Science*, **44**, 128 (1988).
93. M. Cuisinier, C. Hart, M. Balasubramanian, A. Garsuch and L. F. Nazar, *Advanced Energy Materials*, n/a (2015).

94. M. Cuisinier, P. E. Cabelguen, B. D. Adams, A. Garsuch, M. Balasubramanian and L. F. Nazar, *Energy & Environmental Science*, **7**, 2697 (2014).
95. M. Vijayakumar, N. Govind, E. Walter, S. D. Burton, A. Shukla, A. Devaraj, J. Xiao, J. Liu, C. Wang, A. Karim and S. Thevuthasan, *Physical Chemistry Chemical Physics*, **16**, 10923 (2014).
96. D. Prendergast and G. Galli, *Physical review letters*, **96**, 215502 (2006).
97. M. E. Fleet and X. Liu, *Spectrochimica Acta Part B: Atomic Spectroscopy*, **65**, 75 (2010).
98. T. A. Pascal, C. D. Pemmaraju and D. Prendergast, *Physical Chemistry Chemical Physics*, **In Revision** (2015).
99. S. A. Mullin, G. M. Stone, A. Panday and N. P. Balsara, *Journal of The Electrochemical Society*, **158**, A619 (2011).
100. J. P. Perdew, K. Burke and M. Ernzerhof, *Physical Review Letters*, **77**, 3865 (1996).
101. P. Giannozzi, S. Baroni, N. Bonini, M. Calandra, R. Car, C. Cavazzoni, D. Ceresoli, G. L. Chiarotti, M. Cococcioni and I. Dabo, *Journal of Physics: Condensed Matter*, **21**, 395502 (2009).
102. G. Lippert, J. Hutter and M. Parrinello, *Mol Phys*, **92**, 477 (1997).
103. J. VandeVondele, M. Krack, F. Mohamed, M. Parrinello, T. Chassaing and J. Hutter, *Comput Phys Commun*, **167**, 103 (2005).
104. J. VandeVondele and J. Hutter, *J Chem Phys*, **127** (2007).
105. M. Krack, *Theor Chem Acc*, **114**, 145 (2005).
106. S. Goedecker, M. Teter and J. Hutter, *Phys Rev B*, **54**, 1703 (1996).
107. L. Genovese, T. Deutsch and S. Goedecker, *J Chem Phys*, **127** (2007).
108. S. Grimme, J. Antony, S. Ehrlich and H. Krieg, *The Journal of Chemical Physics*, **132**, 154104 (2010).
109. D. Vanderbilt, *Phys Rev B*, **41**, 7892 (1990).
110. G. Kresse and D. Joubert, *Phys Rev B*, **59**, 1758 (1999).
111. E. L. Shirley, *Phys Rev B*, **54**, 16464 (1996).
112. A. Manthiram, Y. Fu and Y.-S. Su, *Accounts of chemical research*, **46**, 1125 (2012).
113. A. Kawase, S. Shirai, Y. Yamoto, R. Arakawa and T. Takata, *Physical Chemistry Chemical Physics*, **16**, 9344 (2014).
114. Y.-X. Yin, S. Xin, Y.-G. Guo and L.-J. Wan, *Angewandte Chemie International Edition*, **52**, 13186 (2013).
115. K. H. Wujcik, T. A. Pascal, C. D. Pemmaraju, D. Devaux, W. C. Stolte, N. P. Balsara and D. Prendergast, *Advanced Energy Materials*, **5**, n/a (2015).
116. K. Dokko, N. Tachikawa, K. Yamauchi, M. Tsuchiya, A. Yamazaki, E. Takashima, J.-W. Park, K. Ueno, S. Seki, N. Serizawa and M. Watanabe, *Journal of The Electrochemical Society*, **160**, A1304 (2013).
117. T. Chivers and P. J. W. Elder, *Chemical Society Reviews*, **42**, 5996 (2013).
118. D. Reinen and G.-G. Lindner, *Chemical Society Reviews*, **28**, 75 (1999).
119. R. J. H. Clark and D. G. Cobbold, *Inorganic Chemistry*, **17**, 3169 (1978).
120. P. L. Leghie, E.; Lelieur, J. P., *New Journal of Chemistry*, **20**, 1121 (1996).
121. F. Gaillard, E. Levillain, M. C. Dhamelincourt, P. Dhamelincourt and J. P. Lelieur, *Journal of Raman Spectroscopy*, **28**, 511 (1997).
122. F. Gaillard, E. Levillain and J. P. Lelieur, *Journal of Electroanalytical Chemistry*, **432**, 129 (1997).
123. E. Levillain, F. Gaillard, P. Leghie, A. Demortier and J. P. Lelieur, *Journal of Electroanalytical Chemistry*, **420**, 167 (1997).
124. M. V. Merritt and D. T. Sawyer, *Inorganic Chemistry*, **9**, 211 (1970).
125. J. Paris and V. Plichon, *Electrochimica Acta*, **26**, 1823 (1981).
126. M. U. M. Patel, I. Arçon, G. Aquilanti, L. Stievano, G. Mali and R. Dominko, *ChemPhysChem*, n/a (2014).

127. Y. Gorlin, A. Siebel, M. Piana, T. Huthwelker, H. Jha, G. Monsch, F. Kraus, H. A. Gasteiger and M. Tromp, *Journal of The Electrochemical Society*, **162**, A1146 (2015).
128. J. B. Weil, James, *Electron Paramagnetic Resonance Elementary Theory and Practical Applications*, John Wiley & Sons, Inc., Hoboken, New Jersey (2007).
129. D. F. Howarth, J. A. Weil and Z. Zimpel, *Journal of Magnetic Resonance*, **161**, 215 (2003).
130. M. Tseitlin, S. S. Eaton and G. R. Eaton, *Concepts in Magnetic Resonance Part A*, **40A**, 295 (2012).
131. P. Dubois, J. P. Lelieur and G. Lepoutre, *Inorganic Chemistry*, **27**, 73 (1988).
132. Y. Gorlin, M. U. Patel, A. Freiberg, Q. He, M. Piana, M. Tromp and H. A. Gasteiger, *Journal of The Electrochemical Society*, **163**, A930 (2016).
133. X. Ji and L. F. Nazar, *Journal of Materials Chemistry*, **20**, 9821 (2010).
134. D. Eroglu, K. R. Zavadil and K. G. Gallagher, *Journal of The Electrochemical Society*, **162**, A982 (2015).
135. M. Hagen, S. Dörfler, P. Fanz, T. Berger, R. Speck, J. Tübke, H. Althues, M. J. Hoffmann, C. Scherr and S. Kaskel, *Journal of Power Sources*, **224**, 260 (2013).
136. M. Hagen, P. Fanz and J. Tübke, *Journal of Power Sources*, **264**, 30 (2014).
137. S.-E. Cheon, K.-S. Ko, J.-H. Cho, S.-W. Kim, E.-Y. Chin and H.-T. Kim, *Journal of The Electrochemical Society*, **150**, A800 (2003).
138. X. Feng, M.-K. Song, W. C. Stolte, D. Gardenghi, D. Zhang, X. Sun, J. Zhu, E. J. Cairns and J. Guo, *Physical Chemistry Chemical Physics*, **16**, 16931 (2014).
139. B. Ravel and M. Newville, *Journal of Synchrotron Radiation*, **12**, 537 (2005).
140. K. H. Wujcik, D. R. Wang, A. Raghunathan, M. Drake, T. A. Pascal, D. Prendergast and N. P. Balsara, *The Journal of Physical Chemistry C* (2016).

Chapter 8 – Appendix

Table 8.1 List of symbols

A	UV-vis absorbance
C_R	Radical concentration
C_S	Sulfur concentration (mM)
CW	Continuous wave
DMF	dimethylformamide
DME	Dimethylether
DMSO	Dimethyl sulfoxide
DOL	Dioxolane
EPD	Electron pair donor
EPR	Electron paramagnetic resonance
ε	UV-vis absorption coefficient
f	Fraction of atomic sulfur in the form of radicals
$f_{Li_2S_2}$	Spectral fraction of Li_2S_2 determined through least squares fitting of the experimental spectra with theoretical spectra
$f_{Li_2S_6}$	Spectral fraction of Li_2S_6 determined through least squares fitting of the experimental spectra with theoretical spectra
$f_{PS,T}$	Spectral fraction of polysulfide dianion species in the back of the cathode
f_{S_8}	Spectral fraction of elemental sulfur in the back of the cathode
f_D	Fraction of sulfur (on an atomic basis) in the back of the cathode as a result of diffusion
f_0	Fraction of sulfur (on an atomic basis) in the back of the cathode since the beginning of discharge
F_{S_8}	Corrected/undiluted spectral fraction of elemental sulfur in the back of the cathode
$F_{PS,0}$	Corrected/undiluted spectral fraction of polysulfide dianions in the back of the cathode
FEP	Fluorinated ethylene propylene
G	Gauss
I_0	Normalized fluorescence intensity for the zeroth scan
I_n	Normalized fluorescence intensity for the 'nth' scan
IND	indicator function
ITFA	iterative transformation factor analysis
L	Path length of UV-vis cuvette
Li-S	Lithium-sulfur
NIR	Near infrared
NMP	n-methylpyrrolidone

NMR	Nuclear magnetic resonance
PCA	principal component analysis
PEO	poly(ethylene oxide)
PID	Proportional-integral-derivative
Q	Cell capacity
S_T	Total moles of sulfur (on an atomic basis) in the back of the cathode
S_0	Total moles of sulfur (on an atomic basis) in the back of the cathode at the beginning of discharge
S_D	Total moles of sulfur (on an atomic basis) that have diffused from the front of the cathode to the back of the cathode
SEO	polystyrene-poly(ethylene oxide)
SIXPACK	Sam's Interface for XAS analysis Package
TEGDME	Tetraethylene glycol dimethyl ether
THF	tetrahydrofuran
UV-vis	Ultra violet-visible
XAS	x-ray absorption spectroscopy
x_{mix}	Ratio of lithium to sulfur in a chemically synthesized polysulfide solution
x_{av}	Average polysulfide dianion chain length for all sulfur containing species in the back of the cathode, calculated using the peak area ratios
$x_{av_{all}}$	Average polysulfide dianion chain length accounting for all sulfur containing species in the back of the cathode
$x_{av_{ps}}$	Average polysulfide dianion chain length for polysulfide dianion species in the back of the cathode
$y_{PS,T}$	Mole fraction of polysulfide dianion species in the back of the cathode
y_{S_8}	Mole fraction of elemental sulfur in the back of the cathode
$y_{PS,D}$	Mole fraction of polysulfide dianions in the back of the cathode as a result of diffusion
$y_{PS,0}$	Mole fraction of polysulfide dianions in the back of the cathode that were created in the back of the cathode
Y_{S_8}	Corrected/undiluted mole fraction of elemental sulfur in the back of the cathode
$Y_{PS,0}$	Corrected/undiluted mole fraction of polysulfide dianions in the back of the cathode
$Y_{S_8}(25)$	Calculated mole fraction of elemental sulfur that would remain assuming the hypothetical reaction shown in equation 5.25
$Y_{S_8}(26)$	Calculated mole fraction of elemental sulfur that would remain assuming the hypothetical reaction shown in equation 5.26
$Y_{S_8}(27)$	Calculated mole fraction of elemental sulfur that would remain assuming the hypothetical reaction shown in equation 5.27

8.2 Spin coating of SEO thin films

The polysulfide containing polymer thin films described in Chapter 2 were prepared by spin coating solutions that contained dimethylformamide, polystyrene-poly(ethylene oxide), and lithium polysulfides. The parameters (i.e. spin coating time, revolutions per minute (RPM), and solution concentration) used to spin coat the films were determined by first studying solutions that contained only DMF and SEO. The SEO used for this study was the same used in Chapter 2, and had a styrene molecular weight of 60 kg/mol and an ethylene oxide molecular weight of 63 kg/mol.

For these experiments, the polymer solution concentration was varied between two values: 50 mg SEO per mL of DMF and 100 mg SEO per mL of DMF. The rate of revolution of the spin coater (Chemat KW-4A) was varied between 1000 and 4000 RPM, and the duration of spin coating was varied between 20 and 60 seconds. For all samples, 30 μ L of solution was pipetted using a micropipette onto pieces of silicon wafer (Addison Engineering, Inc.) that were cleaned with a Kim Wipe beforehand. After the solution was pipette onto the silicon wafer, it was gently spread around the wafer surface using the pipette tip. Spin coating was then started immediately after (roughly 4-5 seconds after the solution was initially dropped onto the wafer). The acceleration of the spin coater could not be varied for these experiments. After spin coating, the samples were allowed to dry at room temperature overnight. It is worth noting that with the exception of the 20 second spin duration samples, all of the samples appeared dry after spin coating. After drying overnight, the samples were measured using an ellipsometer (α -SE Ellipsometer, J.A. Woolman Co., Inc.).

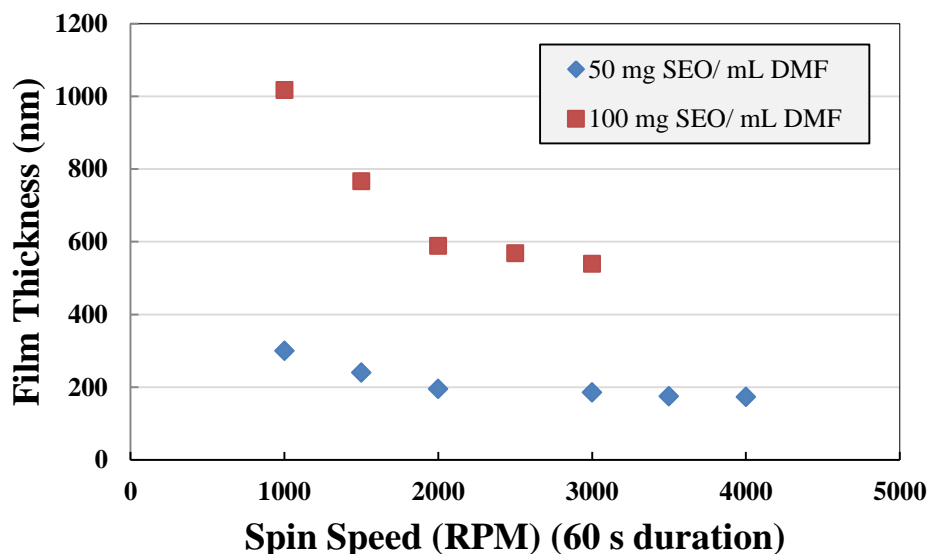


Figure 8.1 SEO thin film thickness as a function of spin coater spin rate (RPM) for a spin duration of 60 seconds for 50 and 100 mg SEO/ mL DMF

In Figure 8.1, the obtained film thickness is plotted versus spin coater speed (RPM) for a 60 second spin duration for 50 and 100 mg SEO/ mL DMF solutions. As the spin speed was increased, resulting films became thinner. For the 50 mg SEO/ mL DMF solution were thinner

than the 100 mg SEO/ mL DMF solution, as a result of the 50 mg SEO/ mL DMF solution being less viscosity. Additionally, around 2000 RPM, the rate of decrease in film thickness with increasing spin speed drops significantly. Film thickness nearly flattens out beyond 2000 RPM for both solutions.

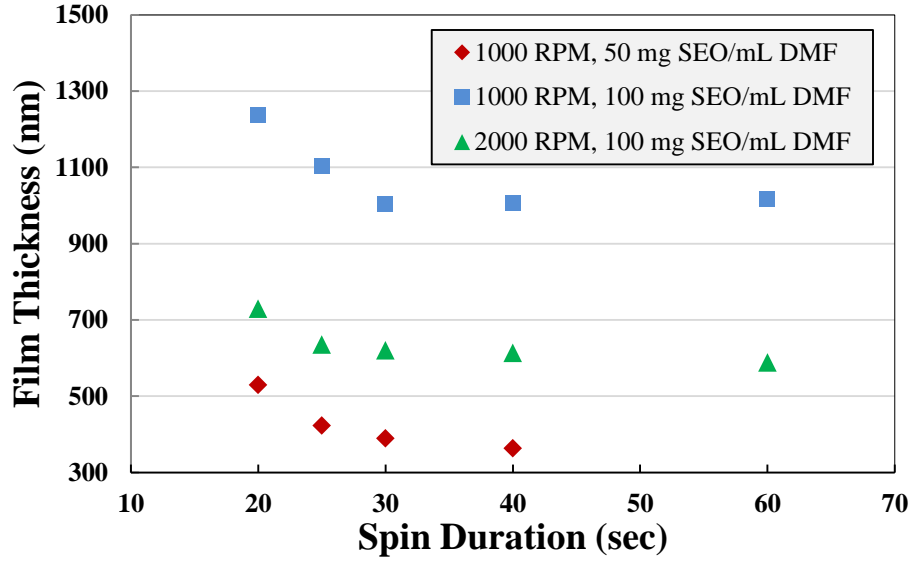


Figure 8.2 SEO film thickness as a function of spin coat duration for three different sets of parameters: (1) 1000 RPM, 50 mg SEO/ mL DMF, (2) 1000 RPM, 100 mg SEO/ mL DMF, (3) 2000 RPM, 100 mg SEO/ mL DMF

In Figure 8.2, the obtained film thickness is plotted versus spin coat duration (the amount of time the sample was rotated for). Three curves are shown: (1) a spin rate of 1000 RPM using a solution of 50 mg SEO/ mL DMF, (2) a spin rate of 1000 RPM using a 100 mg SEO/ mL DMF solution, and (3) a spin rate of 2000 RPM using a solution of 100 mg SEO/ mL DMF. As spin duration increased, films produced by each of the three methods decreased in thickness. However, above roughly 30 seconds, the film thickness appears to flatten out with increasing spin duration. It is possible that after 30 seconds of spinning, the films may already be completely dry. The results shown in Figures 8.1 and 8.2 should allow one to obtain SEO films having thicknesses between 150-1250 nm.

8.3 Corrections for X-ray overabsorption

When XAS is being measured in transmission mode, the absorption coefficient of a sample is can be determined through Beer's law:

$$I = I_0 e^{-\mu(E)\rho t} \quad (8.1)$$

The absorption coefficient is then given by:

$$\mu(E) = -\frac{1}{\rho t} \log\left(\frac{I}{I_0}\right) \quad (8.2)$$

However, when measuring the absorption coefficient in fluorescence mode, we are no longer measuring the absorption coefficient based on the attenuated intensity of the incoming X-ray signal. Instead, we are measuring the absorption coefficient using the intensity of fluorescent photons emitting from the sample. Here, the fluorescence intensity, I_f , is directly proportional to the absorption coefficient through:

$$\mu(E) \propto \frac{I_f}{I_0} \quad (8.3)$$

However, because of a phenomenon known as overabsorption (interchangeably referred to as self-absorption), this equation is not always true.

The contribution of fluorescence intensity (dI_f) from a slice of a sample between depths t and $t + dt$ is given by equation 8.4:

$$dI_f = K \cdot I_0 \cdot \mu_x(E) \rho_x \exp\left(-\left(\mu_{tot}(E) + \mu_{tot}(E_f)\right) \frac{\rho_{tot} t}{\sin\theta}\right) dt \quad (8.4)$$

Here, K is a constant that represents a variety of experimental parameters: the area of the fluorescence detector, the fluorescence yield of the given atom's core shell (i.e. how frequently a fluorescence photon would be created as opposed to an Auger electron if absorption were to occur) and the solid angle covered by the detector. The variable $\mu_x(E)$ represents the absorption coefficient for the atom we are probing with XAS, and is the absorption coefficient we aim to determine (where ρ_x is the density of the element within the sample). The exponential term accounts for the attenuation of incoming photons (of energy E) and outgoing fluorescence photons that have a known energy (E_f) that is characteristic of the X-ray emission lines (e.g. the $K\alpha$ line). The variables $\mu_{tot}(E)$ and $\mu_{tot}(E_f)$ represent the overall absorption coefficient of the material that lead to the attenuation of the incoming and outgoing signals, having a density of ρ_{tot} . The distance photons must travel to depth t , is given by $\frac{t}{\sin\theta}$, where θ is the angle that incoming photons take to enter the sample, and that exiting photons take to reach the fluorescence detector (in our experiment, these angles were equal). Integrating this equation, we arrive at equation 8.5:

$$I_f = K \cdot I_0 \cdot \frac{\mu_x(E) \rho_x}{\left(\mu_{tot}(E) + \mu_{tot}(E_f)\right) \frac{\rho_{tot}}{\sin\theta}} \left[1 - \exp\left(-\left(\mu_{tot}(E) + \mu_{tot}(E_f)\right) \frac{\rho_{tot} t}{\sin\theta}\right)\right] \quad (8.5)$$

We then note that:

$$\mu_{tot}(E) \rho_{tot} = \mu_x(E) \rho_x + \mu_{other}(E) \rho_{other} \quad (8.6)$$

$$\mu_{tot}(E_f) \rho_{tot} = \mu_x(E_f) \rho_x + \mu_{other}(E_f) \rho_{other} \quad (8.7)$$

Here, μ_x is the absorption coefficient of the atom being probed, and μ_{other} is the absorption coefficient of all other atoms in the sample (with a corresponding density of ρ_{other}). Equations 8.6 and 8.7 can then be substituted into equation 8.5. This substitution gives equation 8.8:

$$I_f = K \cdot I_0 \cdot \frac{\mu_x(E)\rho_x}{(\mu_x(E)\rho_x + \mu_{other}(E)\rho_{other} + \mu_x(E_f)\rho_x + \mu_{other}(E_f)\rho_{other})\frac{1}{\sin\theta}} \left[1 - \exp\left(-(\mu_x(E)\rho_x + \mu_{other}(E)\rho_{other} + \mu_x(E_f)\rho_x + \mu_{other}(E_f)\rho_{other})\frac{t}{\sin\theta}\right) \right] \quad (8.8)$$

Examining equation 8.8, we see that the absorption coefficient for the core-hole creation process (i.e. what we are attempting to measure) appears in the denominator. Thus, increases in the absorption coefficient (e.g. when we see a peak in a spectrum) will actually dampen the measured absorption. A decrease in the absorption coefficient will increase the measured absorption coefficient. Effectively, the appearance of the absorption coefficient in the denominator suppresses all absorption features. Another way of interpreting this is that the depth of penetration of X-rays into the sample changes as a function of incoming X-ray energy.

In the work shown in Chapter 2, the goal of using thin films samples (of ~150 nm in thickness) was to avoid thickness related issues of overabsorption. The use of thin films may not always be an option, and for that reason it is convenient to show how overabsorption can be corrected for.

In regards to the impact of sample thickness, equation 8.8 can be examined in three regimes: (1) when samples are extremely thin, (2) when samples are infinitely thick, and (3) when samples have a finite thickness.

When samples are extremely thin, we can use a Taylor expansion on the exponential term in equation 8.8 to arrive at:

$$I_f = K \cdot I_0 \cdot \mu_x(E)\rho_x \quad (8.9)$$

Thus, we recover our highly ideal scenario represented by equation 8.3, and no correction is needed.

When samples are infinitely thick, the exponential term goes to zero and equation 8.8 becomes:

$$I_f = K \cdot I_0 \cdot \frac{\mu_x(E)\rho_x}{(\mu_x(E)\rho_x + \mu_{other}(E)\rho_{other} + \mu_x(E_f)\rho_x + \mu_{other}(E_f)\rho_{other})\frac{1}{\sin\theta}} \quad (8.10)$$

To correct for overabsorption in the case of infinitely thick samples, we note that the values of $\mu_{other}(E)$ and $\mu_{tot}(E_f)$ can be calculated from well documented absorption coefficients for each atom (and knowing the composition of the sample being probed). The variables I_f and I_0 are the intensities we measure experimentally, and θ is the known incident/exiting angle of photons. The challenge, then, is to determine the constant K . To do this, we examine the obtained X-ray spectrum and note that for X-ray energies well above the absorption edge (i.e. outside the XANES region), the absorption coefficient $\mu_x(E)$ is on average equal to one at these energies. Thus, we can solve for K at high values of E , by setting $\mu_x(E)$ equal to 1 for a range of energies.

Once K is determined, equation 8.10 can be used to solve for the correct absorption coefficient $\mu_x(E)$, again using the measured values of I_f and I_0 and the known values of $\mu_{other}(E)$, $\mu_{tot}(E_f)$, ρ_x , ρ_{other} and θ .

Unfortunately, when samples have a finite thickness, equation 8.8 cannot be simplified. However, the process for determining the correct value of $\mu_x(E)$ is similar to the process used for the infinitely thick case. Again, we determine the value of K at high X-ray energies (where

we know $\mu_x(E)$ will on average be equal to 1), and then solve for the corrected values of $\mu_x(E)$ at all other energies.

To test this correction procedure, the sulfur K-edge spectra of lithium polysulfide species dissolved in SEO (60-63 kg/mol, PS to PEO) at a concentration of 0.149 g sulfur/ g SEO and having a stoichiometric $\text{Li}_2\text{S}_{x_{\text{av}}}$ ' x_{av} ' value of 8. These samples were spin coated to thin film thicknesses between 150-1000 nm (thicknesses were measured using ellipsometry). More details on how these samples were prepared can be found in Chapter 2.

The raw spectra obtained for the set of samples is shown in Figure 8.3. As shown, the main edge peak at 2472.6 eV becomes lower as the sample became thicker. Since the samples had the same composition, the spectra should be identical. The difference in main edge peak intensity between sample thicknesses is thus attributed to the effect of overabsorption. Figure 8.4 shows the corrected absorption coefficient values that were obtained using the correction procedure for samples of finite thickness. After correcting for overabsorption, the absorption coefficients are nearly equal, confirming the effectiveness of the correction procedure. This result is significant to those studying lithium polysulfide species, as the main edge to pre-edge peak area ratio can be used to determine the average polysulfide dianion chain length present in a sample. Figure 8.3 shows that overabsorption artificially lowered the main edge peak, which could inadvertently be interpreted as a drop in polysulfide dianion chain length.

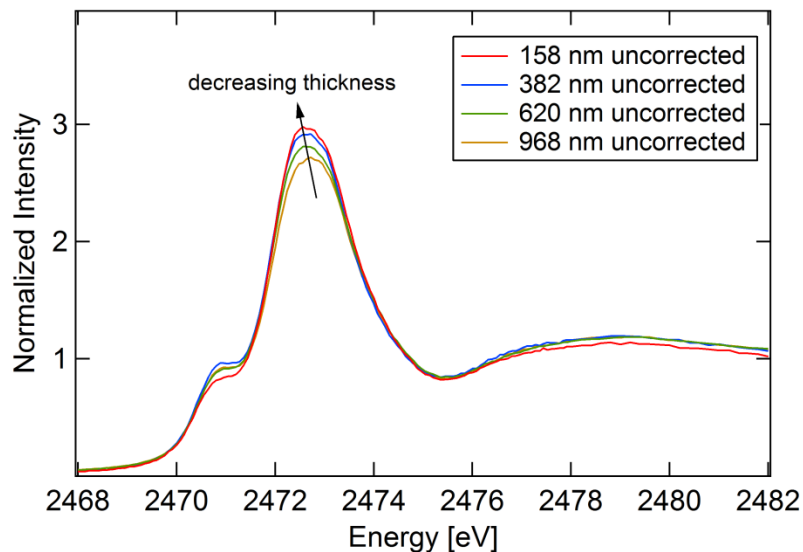


Figure 8.3 Raw Sulfur K-edge XAS spectra obtained for $\text{Li}_2\text{S}_{x_{\text{av}}}$, $x_{\text{av}} = 8$ in SEO at a concentration of 0.149 g sulfur/ g SEO. Thicknesses were measured using ellipsometry.

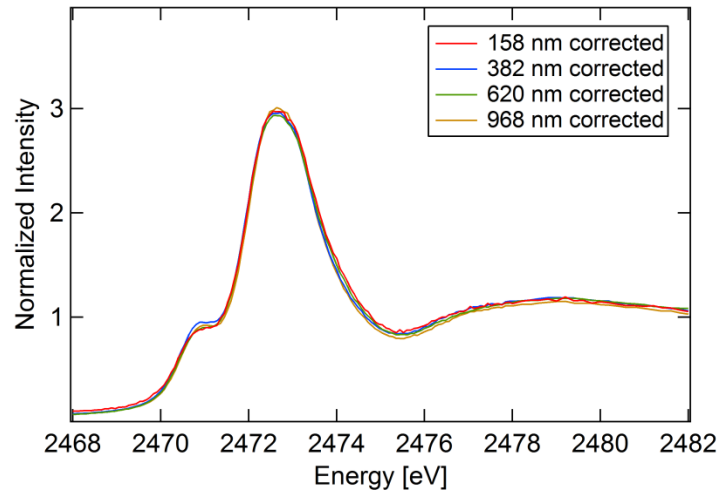


Figure 8.4 Corrected sulfur K-edge XAS spectra for the series of spectra shown in Figure 8.3. The finite thickness correction procedure was used to find the correct value of the absorption coefficient.